Aus dem
NMI Naturwissenschaftliches und Medizinisches
Institut an der Universität Tübingen

# Functional and immunomodulatory effects of non-invasive physical plasma treatment on patient-specific, tissue-resident peritoneal macrophages

**Inaugural-Dissertation**
**zur Erlangung des Doktorgrades**
**der Medizin**

**der Medizinischen Fakultät**
**der Eberhard Karls Universität**
**zu Tübingen**

**vorgelegt von**

**Schultze-Rhonhof, Laura Margarita Elena**

**2025**

| | |
|---|---|
| Dekan: | Professor Dr. B. Pichler |
| 1. Berichterstatter: | Professor Dr. M. Weiss |
| 2. Berichterstatter: | Professor Dr. W. K. Aicher |
| 3. Berichterstatter: | Professor Dr. M. Thill |

Tag der Disputation: 19.03.2025

Parts of this work were previously published in:

**Schultze-Rhonhof L**, Marzi J, Carvajal Berrio DA, et al. Human tissue-resident peritoneal macrophages reveal resistance towards oxidative cell stress induced by non-invasive physical plasma. *Frontiers in Immunology*. 2024;15:1357340. doi:10.3389/fimmu.2024.1357340

**Table of Contents**

## List of figures

## List of tables

## List of abbreviations

| | |
|---|---|
| **7-AAD** | 7-Aminoactinomycin D |
| **AFI** | average fluorescence intensity |
| **APC** | antigen-presenting cell |
| **BSA** | bovine serum albumin |
| **casp** | caspase |
| **CCL** | C-C motif chemokine ligand |
| **CCR2** | C-C chemokine receptor type 2 |
| **CD** | cluster of differentiation |
| **CRS** | cytoreductive surgery |
| **CXC** | C-X-C motif chemokine ligand |
| **DAMP** | damage-associated molecular pattern |
| **DBD** | dielectric barrier discharge |
| **DMEM** | Dulbecco's Modified Eagle's Medium |
| **DPBS** | Dulbecco's phosphate buffered saline |
| **DSB** | double-strand break |
| **ECM** | extracellular matrix |
| **EGFR** | epidermal growth factor receptor |
| **FACS** | fluorescence activated cell sorting |
| **FBS** | fetal bovine serum |
| **FC** | flow cytometry |
| **FMO** | fluorescence minus one |
| **FSC** | forward scatter |
| **GATA6** | GATA-binding protein 6 |
| **H2A.X** | H2A histone family member X |
| **$H_2O_2$** | hydrogen peroxide |
| **HIPEC** | hyperthermic intraperitoneal chemotherapy |
| **HLADR** | human leukocyte antigen – DR isotype |
| **HSC** | hematopoietic stem cells |
| **ICD** | immunogenic cell death |
| **IF** | immunofluorescence |
| **IFN-$\gamma$** | interferon gamma |
| **Ig** | immunoglobin |
| **IL** | interleukin |
| **IP-10** | interferon gamma-induced protein 10 or CXCL10 |
| **LPM** | large peritoneal macrophage |
| **LPS** | lipopolysaccharide |
| **M-CSF** | macrophage-colony stimulating factor |
| **M1** | pro-inflammatory macrophage |
| **M2** | anti-inflammatory macrophage |
| **MAPK** | mitogen-activated protein kinase |
| **MCP-1** | monocyte chemoattractant protein 1 |
| **MEM** | Minimal Essential Medium |
| **MFI** | mean fluorescence intensity |
| **MMP** | metalloproteinase |
| **$NaN_3$** | sodium azide |

| | |
|---|---|
| **NF-kB** | nuclear factor “kappa-light-chain-enhancer” of activated B cells |
| **NIPP** | non-invasive physical plasma |
| **NK** | natural killer cells |
| **$^{\bullet}$NO** | nitric oxide |
| **$NO_2^-$** | nitrites |
| **$NO_3^-$** | nitrates |
| **NOX2** | NADPH oxidase 2 |
| **$O_2^{\bullet-}$** | superoxide |
| **$^{\bullet}$OH** | hydroxyl |
| **P/S** | Penicillin/Streptomycin |
| **PAL** | plasma-activated liquids |
| **PAMP** | pathogen-associated molecular pattern |
| **PC** | principal component |
| **PCA** | principal component analysis |
| **PFA** | paraformaldehyde |
| **PIPAC** | pressurized intraperitoneal aerosol chemotherapy |
| **PMT** | photomultiplier tube |
| **PTEN** | phosphatase and tensin homolog |
| **PUFA** | polyunsaturated fatty acids |
| **ROI** | region of interest |
| **RONS** | reactive oxygen and nitrogen species |
| **rpS6** | S6 ribosomal protein |
| **SD** | standard deviation |
| **SPM** | small peritoneal macrophage |
| **Src** | proto-oncogene, non-receptor tyrosine kinase |
| **SSC** | side scatter |
| **TAM** | tumor-associated macrophages |
| **TCA** | true component analysis |
| **TG** | triglyceride |
| **TGF-ß** | transforming growth factor ß |
| **TLR** | Toll-like receptor |
| **TNF-α** | tumor necrosis factor ∝ |
| **VEGF** | vascular endothelial growth factors |
| **XO** | xanthine oxidase |

# 1 Introduction

## 1.1 Peritoneal cavity and role of peritoneal macrophages

### 1.1.1 Peritoneal cavity and peritoneum

The peritoneum is a continuous tissue membrane that lines the intraperitoneal abdominal organs (visceral layer) and the abdominal and pelvic walls (parietal layer) [1,2]. Thus, it covers an estimated surface area of 1.7 $m^2$ [1]. Like other serosal membranes such as the pleura and pericardium, the peritoneum comprises a monolayer of mesothelial cells, a basal lamina and underlying loose connective tissue (Figure 1) [3]. Cellular and noncellular components, including fibroblasts, adipocytes, blood and lymphatic vessels and extracellular matrix (ECM)-related molecules, form the connective tissue [3,4].

The peritoneal cavity, the space between the parietal and visceral layer, is filled with a small volume of peritoneal fluid (5 - 20 mL) [5]. This plasma transudate contains immunoglobin G (IgG), anti-microbial peptides, free-floating mesothelial cells, and immune cells, including macrophages, eosinophils and lymphocytes [2,4,5]. The peritoneal fluid and the non-adhesive surface of the peritoneum, a mesothelial cell-generated glycocalyx, allow mobility of the abdominal organs against each other [3,5].

The peritoneum facilitates immune modulation, fluid and cell transport while limiting adhesion formation and tumor dissemination [4]. Disruption of these mechanisms may contribute to an imbalance of peritoneal homeostasis, potentially resulting in pathologic conditions such as fibrotic adhesions, inflammatory peritonitis or tumor dissemination [5].

### 1.1.2 Peritoneal macrophages

Macrophages are highly heterogeneous and specialized myeloid cells that partake in immune responses (innate and adaptive), wound repair and tissue

homeostasis [6,7]. Due to their high plasticity, macrophages can adopt either a more pro- (M1) or anti-inflammatory (M2) phenotype [8,9]. In response to the release of pathogen-associated (PAMPs) or damage-associated molecular patterns (DAMPs), pattern recognition receptors like Toll-like receptors (TLR) are activated and pro-inflammatory signaling pathways are triggered [9]. Pro-inflammatory signaling pathways include p38, MAPK and NF-kB, responsible for releasing pro-inflammatory cytokines (e.g., interleukin-1 or IL-1, IL-6) and recruiting additional immune cells to the site of tissue injury or inflammation. These M1 or "classically" activated macrophages are cytotoxic and highly express CD86, a co-stimulatory marker essential for T cell activation [8,10]. Conversely, a non-inflammatory microenvironment accommodates the differentiation towards M2 or "alternatively" activated macrophages [9,11,12]. These anti-inflammatory macrophages highly express the scavenger receptor CD163 and show tumor-promoting properties via the release of growth factors and their involvement in angiogenesis and tissue remodeling. The M1/M2 macrophage polarization nomenclature, however, largely applies to *in vitro* monocyte-derived macrophages, which are classically activated with LPS (lipopolysaccharide) and IFN-$\gamma$ (interferon gamma) or alternatively activated with IL-4 [13]. *In vivo* macrophages may show co-expression of pro- and anti-inflammatory polarization and activation markers.

Research on tissue-resident macrophages has mainly focused on murine macrophages or *in vitro* monocyte-derived macrophages [14]. Limited research on human tissue-resident macrophages is available because of the need for surgical procedures, low cell counts and difficult *in vitro* cell culture conditions [7]. Recent findings and fate-mapping studies have revealed that tissue-resident macrophages are not, as previously assumed, solely derived from hematopoietic stem cells (HSC) [7,15]. Instead, most tissue-resident macrophages stem from embryonic precursors capable of self-renewal and proliferation. F4/80 is highly expressed by yolk sac progenitor-derived tissue-resident macrophages, whereas HSC-dependent macrophages show lower levels of F4/80 [15,16].

Within the peritoneal cavity, monocytes and macrophages constitute 50 to 90 % of leukocytes [2]. In a steady-state, the population of tissue-resident peritoneal macrophages mostly consists of large peritoneal macrophages (LPMs) capable of phagocytosis and tissue repair [7,17]. In contrast, only one-tenth are small blood monocyte-derived peritoneal macrophages (SPMs) (Figure 1). These SPMs are recruited more often following tissue injury or inflammation [17]. GATA-binding protein 6 (GATA6) is the transcription factor responsible for the differentiation of these long-lived murine LPMs, and GATA6-gene-specific expression regulates their survival, proliferation and metabolism [16]. Ruiz-Alcaraz et al. suggested that the $CD14^{++(high)}$, $CD16^{++(high)}$ subset constitutes a mature phenotype of tissue-resident human peritoneal macrophages found in a homeostatic environment [14].

Peritoneal macrophages have often been utilized to study the phagocytic or oxidative activity of tissue-resident macrophages [14,18]. Phagocytosis is the process by which pathogens, foreign materials and other cells larger than 0.5 µm in diameter can be ingested and eliminated by forming a specialized vacuole or "phagosome" [19]. As specialized phagocytes, macrophages can remove pathogens via phagocytic oxidative burst, which refers to the quick release of elevated levels of reactive oxygen species (ROS) [20]. Superoxide ($O_2^{\bullet -}$) and hydrogen peroxide ($H_2O_2$) are produced by NADPH oxidase 2 (NOX2) and xanthine oxidase (XO) [21]. These high intrinsic levels of ROS formed during oxidative burst could explain the higher resistance of macrophages toward oxidative stress [22].

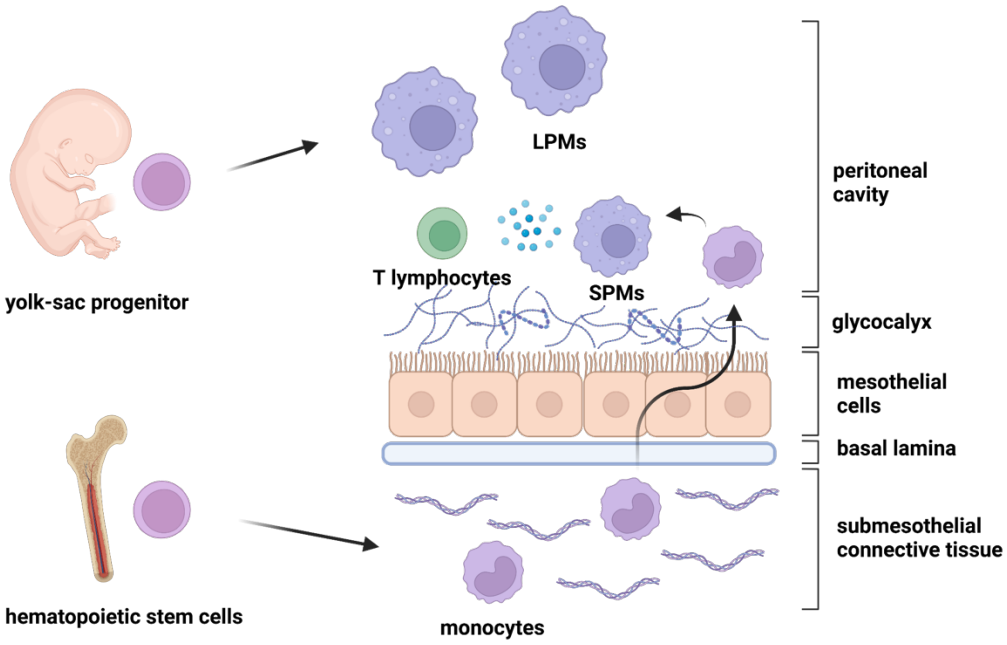


**Figure 1: Origin of tissue-resident peritoneal macrophages and their local proliferation within the peritoneal cavity.** Tissue-resident macrophages (large and small peritoneal macrophages, LPMs and SPMs) are derived from yolk-sac progenitors and hematopoietic stem cells (HSC) [7,15]. The peritoneum comprises a monolayer of mesothelial cells, basal lamina and underlying connective tissue [3]. Adapted from Dos Anjos Cassado et al., *Frontiers in Immunology*, 2015, under CC BY 4.0 [16]. Created with biorender.com.

## 1.2 Peritoneal surface malignancies and role of peritoneal macrophages

### 1.2.1 Peritoneal surface malignancies

Peritoneal surface malignancies stem from primary tumors of the peritoneum (e.g., peritoneal mesothelioma) or from peritoneal metastasis of tumors with intraperitoneal or extraperitoneal origin [1]. Development of peritoneal metastasis differs greatly depending on the origin of the primary tumor, of which ovarian and gastric cancer show the highest incidence of peritoneal involvement. Prior to the introduction of advanced surgical techniques and hyperthermic intraperitoneal chemotherapy (HIPEC) or pressurized intraperitoneal aerosol chemotherapy (PIPAC), minimal therapeutic options existed to achieve full cytoreduction and removal of microscopic residual tumor [23-25]. Cytoreductive surgery (CRS) and HIPEC is, however, related to a high incidence of postoperative complications [26]. Zhou et al. showed that 22 out of 86 patients (25.6%) suffered from high grade

postoperative complications after CRS and HIPEC, which negatively affected the patient survival outcome.

Tumor dissemination within the peritoneal cavity can occur via the hematogenous, lymphatic or transcoelomic route [27]. The latter requires the detachment of cells from the intraperitoneal primary tumor, survival of cancer cells within the peritoneal cavity and attachment to the mesothelial monolayer [28]. Damage to the mesothelial cell monolayer via the release of matrix metalloproteinases (MMPs) allows for invasion of the submesothelial space [28,29]. MMPs form a family of calcium- and zinc-dependent proteolytic enzymes that can cleave most ECM components and regulate other enzymes and cell receptors. *De novo* angiogenesis is necessary for tumor growth, mostly regulated by the release of vascular endothelial growth factor (VEGF) [28].

### 1.2.2 Role of tumor-associated macrophages

Macrophages, which infiltrate or settle in the microenvironment of solid tumors, are defined as tumor-associated macrophages (TAM) [30]. Their polarization is determined by the tumor microenvironment and the cytokines, chemokines and other signaling molecules released by cancer and stromal host cells [31]. High expression levels of IL-4, IL-13, C-C motif chemokine ligand 8 (CCL8) and C-X-C motif chemokine ligand 12 (CXC12) within the tumor microenvironment promote recruitment and polarization towards the predominantly M2-like phenotype of TAMs. The M2-like phenotype can be further subdivided into M2a and M2b macrophages with immunoregulatory properties, while M2c macrophages show immunosuppressive activity and are involved with tissue remodeling [32].

TAMs participate in nearly the entire process of tumor cell metastasis, including invasion, vascularization, intra- and extravasation and creating pre-metastatic niches [31]. TAMs, for example, release proteolytic enzymes, including MMPs and serine proteases, as well as soluble factors such as transforming growth factor ß (TGF-ß), IL-8 and IL-1ß, leading to loss of ECM as a barrier against tumor

invasion. *De* novo angiogenesis and remodeling of the existing vasculature through the release of VEGF and MMP-9 further promote tumor growth. Consistent with their pro-tumoral activity, high infiltration of TAMs is related to poor outcomes in most human cancers [33]. Altered epidermal growth receptor (EGFR) signaling reduced the number of M2-polarized TAMs and improved prognosis in murine cancer cell models [34]. In contrast, pro-inflammatory M1 macrophages have tumoricidal potential by increasing their pro-inflammatory cytokine secretion, antibody-dependent cellular toxicity and phagocytotic activity [33].

## 1.3 Peritoneal adhesions and tissue repair

### 1.3.1 Peritoneal adhesions

Peritoneal adhesions are fibrous bands that can form between the omentum, intraperitoneal viscera and abdominal wall [35,36]. These bands constitute either a thin layer of connective tissue, more organized bands with nerve fibers and blood vessels or direct contact of serosal surfaces. Peritoneal adhesions can be categorized as congenital or acquired, of which the latter can be of inflammatory (e.g., peritonitis) or postoperative origin. The incidence of peritoneal adhesions after surgery is estimated at 67 to 93 % [37,38].

Even though most patients with postoperative adhesions are asymptomatic, a clinically relevant number of patients develop a symptomatic condition or “adhesive disease” [39]. One-third of patients, who received open abdominal-pelvic surgery, required two hospital readmissions on average over ten years for adhesion-related complications [40]. Postoperative complications include small bowel obstruction, chronic abdominal-pelvic pain, secondary infertility and increased technical difficulty with subsequent surgery [41,42]. The cost for adhesion-related complications surpasses $2 billion annually in the United States [42,43].

Surgical lysis of adhesions, or adhesiolysis, is often required for patients with symptomatic bowel obstruction, infertility and ineffective pain relief [41,44].

Prevention of postoperative adhesions is necessary to reduce adhesion-related morbidity and improve patient outcomes after abdominal-pelvic surgery. Development of these anti-adhesive prophylactic agents, however, requires a better understanding of the pathophysiology of the inflammatory response to surgical trauma-induced peritoneal injury.

### 1.3.2 Peritoneal tissue repair

Peritoneal tissue repair differs from skin or other epithelial layer repair as it results from the simultaneous repopulation of mesothelial cells from undifferentiated precursor cells of the underlying mesenchyme and the implantation of free-floating mesothelial cells [45,46]. Since peritoneal tissue defects do not solely rely on the proliferation or migration of mesothelial cells from the edges, these defects can be closed more quickly, mostly independent of the initial size of the injury [45].

Physiological tissue repair and the development of peritoneal adhesions undergo three phases following tissue injury: (1) inflammation, (2) coagulation and proteolysis and (3) remodeling or formation [45]. Injured mesothelium releases cytokines and chemokines, including IL-1, IL-6 and tumor necrosis factor $\alpha$ (TNF-$\alpha$), allowing for higher vascular permeability and the recruitment of additional immune cells to the injury site. Vascular injury activates the coagulation cascade, resulting in thrombin generation and fibrin deposition [45,47]. These fibrin deposits form a temporary matrix on the tissue defect, attract peritoneal macrophages and are later repopulated with mesothelial cells. If the balance between coagulation and fibrinolysis is dysregulated after surgery and insufficient fibrinolysis occurs, collagen- and fibronectin-producing fibroblasts proliferate within the substrate matrix [48]. The ingrowth of capillaries and neuronal fibers leads to more organized adhesions [45,49]. If, however, inflammation subsides and fibrinolysis leads to the degradation of these fibrin deposits, normal peritoneal healing occurs, which is facilitated by the proteolytic environment of the peritoneal cavity under physiologic conditions [35,48].

### 1.3.3 Role of peritoneal macrophages in tissue repair

Intravital microscopy has shown that GATA6+ tissue-resident peritoneal macrophages attach to tissue defects within seconds of injury, entirely engulfing the wound within 15 minutes [50]. The formation of these aggregates in response to DAMPs leads to a reduced number of peritoneal macrophages in peritoneal lavages [17]. This “macrophage disappearance reaction” is associated with higher pro-inflammatory cytokine levels in the peritoneal fluid and the recruitment of monocytes and other immune cells to the peritoneal cavity. These SPMs can be directly involved in wound repair or act as an intermediate population to replace the depleted GATA6+ macrophages.

## 1.4 Non-invasive physical plasma

### 1.4.1 Definition and use of non-invasive physical plasma

Non-invasive physical plasma (NIPP) is a novel therapeutic tool with wound healing, anti-tumoral and anti-microbial properties [51]. NIPP is a highly reactive (partially) ionized gas at atmospheric pressure [52]. Consisting of a high number of reactive species, ions, electrons, electromagnetic field and weak ultraviolet radiation, NIPP exerts physical and chemical effects. While these physical effects (e.g., generation of an electromagnetic field, ultraviolet radiation) are minimal [53,54], the chemical effects through plasma-derived reactive oxygen and nitrogen species (RONS) can induce considerable molecular and morphological changes at a cellular level [52,53]. NIPP can, for example, induce cellular membrane changes, DNA double-strand breaks (DNA-DSBs), increase intracellular RONS levels and decrease the anti-oxidative potential of cells.

NIPP is produced using electric alternate or direct currents, microwaves or radiofrequencies [55]. Different methods and configurations exist to generate ionized gases: dielectric barrier discharge (DBD), atmospheric pressure plasma jets and plasma needles [56]. Frequently used feeding gases are atmospheric air, pure nitrogen or noble gases, including argon. In this study, an atmospheric

pressure plasma jet – kINPen® MED – with argon as the feeding gas was used. The kINPen® MED incorporates a pin-type powered electrode within a dielectric ceramic tube and an outer electrode [57]. The pen-like handpiece is connected to a power and gas supply unit with a flexible tube approximately 1 m long (Figure 2).

As the feeding gas is ionized to form plasma, the charged species in the plasma discharge react with atmospheric air and the target, either solids or liquids, transforming oxygen- and nitrogen-based species into reactive species [58]. Hydroxyl ($^{\bullet}OH$) and nitric oxide ($^{\bullet}NO$) are generally formed by plasma-air interactions, whereas plasma-liquid interactions generate long-lived nitrates ($NO_3^-$), nitrites ($NO_2^-$), and hydrogen peroxide ($H_2O_2$). The biologically active agents can be transferred from the gas to the liquid phase to generate plasma-activated liquids (PAL) [59]. These biologically active agents most likely possess the primary anti-tumoral activity since comparable effects *in vitro* and *in vivo* with PAL and direct treatment were observed [60]. Additionally, the cytotoxicity of these RONS is suppressed by adding specific scavengers (e.g., cysteine, catalase) or renewing the cell medium directly after PAL treatment. The indirect treatment offers advantages over direct treatment, as more tumor modalities can be targeted (e.g., injection of solid tumors or use as an abdominal lavage) [61]. PAL can be stored for up to seven days at -80 °C without losing effectiveness [53,62].

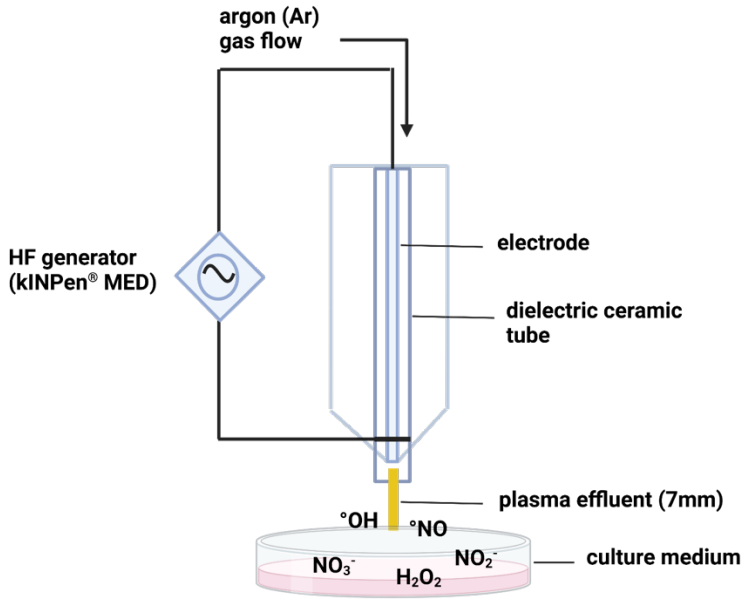


**Figure 2: Schematics of the atmospheric pressure plasma jet kINPen® MED.** The kINPen® MED incorporates a pin-type powered electrode within a dielectric ceramic tube and an outer electrode [57]. Adapted from Holl et al., *Biomedicines*, 2022, under CC BY 4.0 [63]. Created with biorender.com.

Studies have demonstrated the therapeutic effects of NIPP treatment, leading to its use in wound repair, cancer as well as infectious or inflammatory skin disease treatment [64,65]. The selective anti-tumoral activity of NIPP is promising, as studies showed *in vitro* anti-proliferative effects on ovarian, colorectal and cervix cancer cells [66-68]. *In vivo* effects have also been shown in clinical trials. Marzi et al. (2022), for example, demonstrated that NIPP could be an alternative to invasive loop electric excision, offering a tissue-preserving treatment modality for patients with confirmed cervical intraepithelial neoplasia [69]. In the 24-week follow-up, 19 out of 20 patients (n = 20) showed complete histological remission.

### 1.4.2 Anti-tumoral activity of non-invasive physical plasma

Cancer cells have shown a greater sensitivity towards plasma-derived RONS than benign cells, possibly due to their higher expression of aquaporins and lower distinct cholesterol fraction in the cellular membrane [70,71]. Studies have further suggested that NIPP can promote immunogenic cell death (ICD) by which dying cancer cells release DAMPs [72,73]. Especially considering that cancer cells can evade surveillance of the host immune system, ICD and NIPP treatment could

re-establish the immunogenicity of cancer cells by promoting adaptive immunity against cancer cells [53,74]. NIPP treatment can, for example, lead to higher activation of antigen-presenting cells (APCs) and shift the anti-inflammatory, tumor-promoting milieu towards a more pro-inflammatory tumor microenvironment [74,75].

### 1.4.3 Wound healing properties of non-invasive physical plasma

NIPP presents wound healing properties due to its bactericidal effects via the upregulation of anti-microbial peptides of the ß-defensin family and faster initiation of tissue repair via inflammatory stimuli [64,76]. NIPP-derived RONS may lead to an increased release of signaling molecules (e.g., IL-6, IL-8 and monocyte chemoattractant protein 1 or MCP-1) [77,78]. Regarding peritoneal tissue repair, NIPP showed dose-dependent reduced proliferation of pro-adhesive peritoneal fibroblasts, while peritoneal mesothelial cells maintained their wound closure potential [63]. While RONS may show beneficial wound healing effects, excessive production may slow wound repair by contributing to an imbalanced redox homeostasis [79].

## 1.5 Aim of thesis

The role of peritoneal macrophages in tumor dissemination and postoperative adhesions emphasizes the need for therapeutic alternatives targeted at peritoneal macrophages. As present prophylactic and therapeutic agents showed an unclear clinical benefit or are associated with side effects [80,81], NIPP treatment could offer a novel, non-invasive therapeutic approach.

This study aimed to isolate, culture and characterize human tissue-resident peritoneal macrophages from peritoneal lavages since most research focused on murine macrophages or *in vitro* differentiated human blood monocyte-derived macrophages [14]. Hence, investigations on specifically human tissue-resident macrophages are required in order to further translate these experimental preclinical findings to more human-like models. After establishing the cell culture model, this study investigated the PAL-derived molecular and cellular effects focusing on the following in human tissue-resident peritoneal macrophages:

- Does NIPP treatment induce DNA double-strand breaks and apoptosis?
- Does NIPP treatment induce anti-oxidative pathways?
- Does NIPP treatment induce a phenotype switch?
- Does NIPP treatment alter the release of cytokines and chemokines?
- Does NIPP treatment affect migratory activity?
- Does NIPP treatment show subcellular effects at a nuclei, lipid and protein level as measured by label-free, marker-independent Raman micro-spectroscopy?

# 2 Material and methods

## 2.1 Material

### 2.1.1 Laboratory equipment

**Table 1: Instruments**

| Instrument | Type | Manufacturer |
|---|---|---|
| Automated cell counter | NucleoCounter NC-200 | Chemometec, Denmark |
| Brightfield microscope | EVOS XL Core Cell Imaging System | ThermoFisher, USA |
| Cell cytometer | BD LSR Fortessa | BD Bioscience, Germany |
| Centrifuges | Centrifuge 5424 R, 5415 R, 5810 R, MiniSpin | Eppendorf, Germany |
| Centrifuge | Megafuge 8 small benchtop centrifuge | ThermoFisher, Germany |
| Fluorescence microscope | Cell Observer | Carl Zeiss AG, Germany |
| Incubator | $CO_2$ incubator CB 150 | Binder, Germany |
| Objective | 63 x Apochromat water immersion-objective | N.A. 1.4, Olympus, Japan |
| Pipetboy | Pipetboy acu 2 | Integra Biosciences, Germany |
| Pipettes | Eppendorf Research Plus 0.1-2.5 µL, 0.5-10 µL, 10-200 µL, 100-1000 µL | Eppendorf, Germany |
| Plasma jet | kINPen MED | neoplas tools, Germany |
| Thermomixer | ThermoMixer C | Eppendorf, Germany |
| Raman microscope | WITec alpha 300 R Raman System | WITec GmbH, Germany |
| Vortex | Vortex Genie 2 | Scientific Industries Inc., USA |
| Water bath | | GFL, Germany |

### 2.1.2 Consumables

**Table 2: Consumables**

| Material | Type | Manufacturer |
|---|---|---|
| Automatic cell counter cassette | NucleoCounter Via2-Casette | Chemometec, Denmark |

| | | |
|---|---|---|
| Cell culture inserts | ThinCert, 8 µm pore size | Greiner Bio-One, Germany |
| Cell culture well plates | 6, 24 and 48 wells | Corning, USA |
| Cell scraper | | Corning, USA |
| Cotton swabs | | Rossmann, Germany |
| Cryo tubes | 2 mL | Greiner Bio-One, Germany |
| Imaging dishes | µ-Dish 35 mm, high (glass bottom) | Ibidi, Germany |
| Plate sealers | | BioLegend, USA |
| Plastic pipettes | 10 µL, 100 µL, 200 µL, 1 mL | Greiner Bio-One, Germany |
| Plastic pipettes | 5 mL, 25 mL, 50 mL | Corning, USA |
| Polypropylene centrifuge tubes | 15 mL, 50 mL | Greiner Bio-One, Germany |
| Polypropylene microfuge tubes | 1.5 mL, 2 mL | Eppendorf, Germany |
| Polystyrene microfuge tubes | 5 mL | BD Bioscience, Germany |
| V-bottom plate | | BioLegend, USA |

2.1.3 Gas

**Table 3: Gas**

| Gas | Purity | Catalogue number | Manufacturer |
|---|---|---|---|
| Argon | ≥ 99,996 % | 10100321 | Linde, Germany |

2.1.4 Reagents

**Table 4: Reagents**

| Reagent | Catalogue number | Manufacturer |
|---|---|---|
| Accutase | 423201 | Biolegend, USA |
| Bovine serum albumin (BSA) | 8076 | Carl Roth, Germany |
| CS&T RUO beads | 15849991 | BD Bioscience, Germany |
| Dulbecco's phosphate buffered saline (DPBS) | 14190094 | Gibco, USA |
| EDTA | 8043.1 | Carl Roth, Germany |
| Fixation/Permeabilization solution kit | 554714 | BD Bioscience, Germany |
| Human male AB serum | 21001P | H2B, France |
| Methanol ≥99 % | 8388.1 | Carl Roth, Germany |

| | | |
|---|---|---|
| Sodium azide ($NaN_3$) | 4221.1 | Carl Roth, Germany |
| Staurosporin | S1421 | Selleck Chemicals, USA |
| Triton X-100 | 3051.4 | Carl Roth, Germany |
| UltraComp eBeads Plus compensation beads | 01-3333-41 | ThermoFisher, Germany |
| 4 % Paraformaldehyde (PFA) | 158127 | Sigma-Aldrich, USA |

2.1.5 Buffers and solutions

**Table 5: Buffers and solutions**

| **Buffers, solutions** | **Components** |
|---|---|
| Blocking buffer (IF) | 0.5 g BSA + 30 µL Triton + 10 mL DPBS |
| Antibody dilution buffer (IF) | 0.1 g BSA + 30 µL Triton + 10 mL DPBS |
| 1 x Perm/Wash | 1 mL 10 x Perm/Wash + 9 mL distilled water |
| FACS buffer | DPBS + 2 % FBS + 0.05 mM $NaN_3$ + 0.1 mM EDTA |

2.1.6 Cell culture media and supplements

**Table 6: Cell culture media and supplements**

| **Reagent** | **Catalogue number** | **Manufacturer** |
|---|---|---|
| Dulbecco's Modified Eagle's Medium (DMEM), high glucose, Glutamax™ supplement, pyruvate | 31966021 | Gibco, USA |
| Fetal bovine serum (FBS) | 10270-106 | Gibco, USA |
| Minimal Essential Medium (MEM) | 31095029 | Gibco, USA |
| L-Glutamine | 25030-024 | Gibco, USA |
| Penicillin/Streptomycin (P/S) | 15140-122 | Gibco, USA |
| Recombinant human macrophage-colony stimulating factor (M-CSF) | 300-25 | PeproTech, Germany |

2.1.7 Antibody targets, commercial kits and viability dyes

**Table 7: Antibody targets, commercial kits and viability dyes**

| Antibody target, viability dyes | Species | Catalogue number | Manufacturer |
|---|---|---|---|
| Anti-human CD14 PE (clone HCD14) | mouse IgG1 | 325605 | BioLegend, USA |
| Anti-human CD14 FITC (clone HCD14) | mouse IgG1 | 325603 | BioLegend, USA |
| Anti-human CD16 BV605™ (clone 3G8) | mouse IgG1 | 302039 | BioLegend, USA |
| Anti-human CD68 PE-eFluor 610 (clone Y1/82A) | mouse IgG2b | 61-0689-42 | ThermoFisher Scientific, USA |
| Anti-human CD68 (clone D4B9C) | rabbit IgG | 76437 | Cell Signaling Technology, Netherlands |
| Anti-human CD86 PE (clone IT2.2) | mouse IgG2b | 305405 | BioLegend, USA |
| Anti-human CD163 PE/Cy7 (clone GHI/61) | mouse IgG1 | 25-1639-42 | ThermoFisher Scientific, USA |
| Anti-human CD206 BV421™ (clone 15–2) | mouse IgG1 | 321125 | BioLegend, USA |
| Anti-human GATA6 PE (clone D61E4) | rabbit IgG | 26452 | Cell Signaling Technology, Netherlands |
| Anti-human HLADR FITC (clone Tü36) | mouse IgG2b | 361603 | BioLegend, USA |
| Anti-phospho-Histone-H2A.X FITC (Ser139, clone JBW301) | mouse IgG1 | 16-202A | Sigma-Aldrich, USA |
| Apotracker Green staining solution | | 427401 | BioLegend, USA |
| CellTracker Green CMFDA | | C2925 | ThermoFisher Scientific, USA |
| Cy3-AffiniPure | goat anti-rabbit (H+L) | 111-165-003 | Jackson ImmunoResearch, UK |
| Hoechst 34580 | | H21486 | ThermoFisher Scientific, USA |
| LEGENDplex HU Essential Immune Response Panel | | 740930 | BioLegend, USA |
| Zombie NIR | | 423105 | BioLegend, USA |

| | | | |
|---|---|---|---|
| 7-Aminoactinomycin D (7-AAD) viability staining solution | | 420403 | BioLegend, USA |

**Table 8: Antibody and viability dye "master mixes"**

| Antibody, viability dye | Use | Dilution ratio | "Master mix" |
|---|---|---|---|
| Apotracker | FC | 1:200 | 1 µL 80 µM Apotracker stock solution + 9 µL FACS buffer → 5 µL diluted reagent + 100 µL FACS buffer |
| CellTracker Green CMFDA | IF | 1:1000 | 1 µL 10 mM CellTracker stock solution + 999 µL serum-free DMEM Glutamax |
| CD14, CD68 | FC | 1:50 | **CD14**: 1 µL Ab + 5 µL human serum + 45 µL FACS buffer<br>**CD68**: 2 µL Ab + 10 µL human serum + 90 µL 1 x Perm/Wash |
| CD14, CD16, GATA6 | FC | 1:50<br><br>1:50 | **CD14, CD16**: 2 µL Ab + 4.8 µL human serum + 43.2 µL FACS buffer<br>**GATA6**: 2 µL Ab + 10 µL human serum + 90 µL 1 x Perm/Wash |
| CD68 | IF | 1:800 | 2.5 µL Ab + 2000 µL antibody dilution buffer |
| CD86, HLADR, CD163, CD206 | FC | 1:50 | 4 µL Ab + 4.2 µL human serum + 41.8 µL FACS buffer |
| Cy3-AffiniPure | IF | 1:500 | 6 µL Ab + 3000 µL antibody dilution buffer |
| H2A.X | FC | 1:250 | 0.4 µL Ab + 10 µL human serum + 90 µL 1 x Perm/Wash |
| Hoechst | IF | 1:1000 | 3 µL Ab + 3000 µL antibody dilution buffer |
| Zombie NIR | FC | 1:1000 | 0.5 µL Zombie NIR + 500 µL DPBS |

FC: flow cytometry, IF: immunofluorescence, Ab: Antibody

### 2.1.8 Software programs

**Table 9: Software programs**

| Software programs | Manufacturer |
|---|---|
| BD FACSDiva (8.0.3) | Becton Dickinson, USA |
| Control FIVE (5.0) | WITec GmbH, Germany |
| EndNote (20.2) | Clarivate Analytics, USA |
| FlowJo (10.8.2) | Becton Dickinson, USA |
| GraphPad Prism (9) | GraphPad Software Inc., USA |
| ImageJ | U.S. National Institutes of Health, USA |
| LEGENDplex data analysis | BioLegend, USA |

| | |
|---|---|
| MatLab (R2018a) | The MathWorks, Germany |
| Microsoft PowerPoint (16.43) | Microsoft, USA |
| Microsoft Word (16.43) | Microsoft, USA |
| NucleoView™ NC-200 Software | Chemometec, Denmark |
| Project FIVE (5.2) | WITec GmbH, Germany |
| TheUnscrambler (X10.5) | Camo Software AS, Norway |
| ZEN (blue edition) | Carl Zeiss, Germany |

## 2.2 Methods

### 2.2.1 Sample collection of human tissue-resident peritoneal macrophages

Samples were obtained following written informed consent from patients undergoing laparoscopic surgery at the University Women's Hospital in Tübingen. The ethics committee of the medical faculty at the Eberhard Karl's University Tübingen approved the use of human donor cells (495/2018BO2). Shortly after skin incisions were made for port placement in exploratory or therapeutic laparoscopic surgery, the peritoneal cavity was rinsed with 10 - 15 mL sterile, isotonic 0.9 % NaCl solution, which was then collected from the pouch of Douglas (rectouterine pouch) with a plastic syringe (Figure 3). Contamination with blood could not always be avoided. Samples were stored at 4 °C to minimize cell attachment to the plastic syringe prior to isolation.

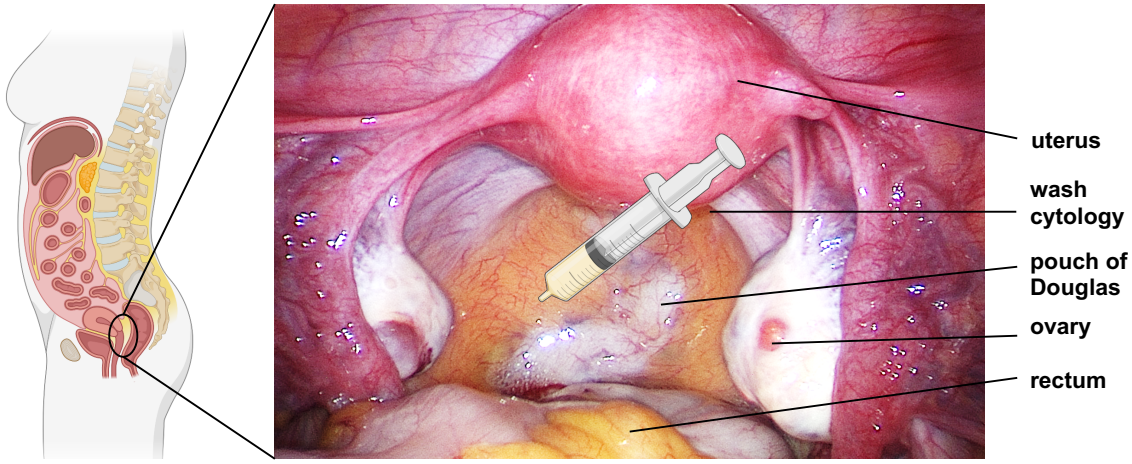


**Figure 3: Sample collection of wash cytology in the pouch of Douglas.** Laparoscopic image of the pouch of Douglas (rectouterine pouch) shown with permission of Prof. Martin Weiss. Adapted from Holl et al., *Biomedicines*, 2021, under CC BY 4.0 [82]. Created with biorender.com.

### 2.2.2 Isolation of human tissue-resident peritoneal macrophages

Human tissue-resident peritoneal macrophages were isolated from peritoneal lavages as previously described [83,84]. The isolation process is described in Figure 4. The sample was transferred from the plastic syringe into a 50 mL Falcon tube and centrifuged at 500 x g for 5 min at 4 °C. The supernatant was carefully removed and the cell pellet was washed with 10 mL cold $Ca^{2+}$/$Mg^{2+}$-free DPBS.

A second washing step followed and the cell pellet was resuspended in 2 mL cold DMEM Glutamax supplemented with 20 ng/mL macrophage-colony stimulating factor (M-CSF), 100 µg/mL streptomycin, 100 U/mL penicillin, 2 mM L-glutamine and 10 % heat-inactivated FBS. 20 µL of the cell suspension was diluted at a 1:4 dilution ratio for cell counting with an automated cell counting device. The cells were seeded at a seeding density of 2 - 4 x $10^5$ cells per well in a polystyrene 48-well plate and left to adhere at 37 °C and 5 % $CO_2$. After a 2h-incubation period, non-adherent cells were aspirated and removed. Plastic-adherent macrophages were washed three times with 200 µL warm DPBS. The protocol relies on the faster adherence of macrophages than other peritoneal cells [83]. Initial seeding density was chosen based on the subsequent experiments performed.

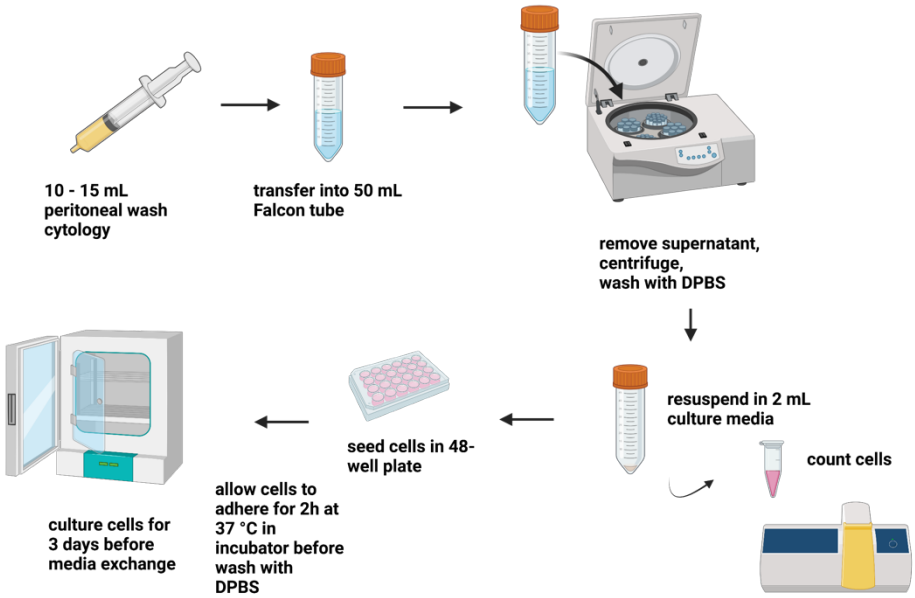


**Figure 4: Isolation of human tissue-resident peritoneal macrophages.** Isolation of cells after sample collection from the peritoneal cavity. Created with biorender.com.

### 2.2.3 Culture of human tissue-resident peritoneal macrophages

Human peritoneal macrophages were cultured in 200 µL DMEM Glutamax per well in a 48-well plate. The exchange of culture media was performed three days after isolation by washing cells once with warm DPBS and adding fresh culture media. The morphology of the macrophages was observed daily using a brightfield microscope.

### 2.2.4 Enzymatic dissociation and reseeding

Human peritoneal macrophages were harvested enzymatically with accutase. Macrophages were washed three times with either cold DPBS or FACS buffer (DPBS + 2 % FBS + 0.05 mM $NaN_3$ + 0.1 mM EDTA), depending on whether cells were reseeded or stained for flow cytometry. Adherent macrophages were detached with accutase for 10 min at 37 °C and 5 % $CO_2$. Culture media was added to inactivate accutase. The cell suspension was collected in 15 mL tubes and the remaining adherent cells were washed three times. The cell suspension was centrifuged at 300 x g for 5 min at 4 °C and resuspended in either culture media or FACS buffer. Prior to reseeding, cells were counted using an automated cell counter.

### 2.2.5 Immunostaining

Immunostaining of the intracellular protein CD68 and the nuclear-specific dye Hoechst was used to characterize human peritoneal macrophages morphologically. Primary human peritoneal fibroblasts were used as a negative control. Macrophages were reseeded in glass bottom imaging dishes at a seeding density of 3 x $10^5$ cells. Cells were cultured for 24 hours at 37 °C and 5 % $CO_2$. Cells were fixed with 400 µL 4 % PFA for 10 min at 37 °C. PFA was removed and cells were washed three times with 500 µL cold DPBS. All steps with PFA including washing steps were performed under a specialized fume hood. For permeabilization of cells, cells were incubated in 400 µL ice-cold methanol for 20 min at -20 °C. Cells were then rinsed with 1 mL cold DPBS for 5 min. Cells were blocked with a blocking buffer (0.5 g BSA + 30 µL Triton + 10 mL DPBS) for 60 min at room temperature in the dark. The blocking buffer was aspirated and 400 µL of the diluted primary antibody CD68 was added. The antibody was diluted at a 1:800 dilution ratio with an antibody dilution buffer (0.1 g BSA + 30 µL Triton + 10 mL DPBS). Cells were incubated overnight with the primary antibody, covered in aluminum foil and stored at 4 °C. Cells were rinsed three times with 1 mL cold DPBS. Cells were incubated in 400 µL of the diluted fluorochrome-conjugated secondary antibody Cy3 for 60 min at room

temperature in the dark. The secondary antibody Cy3 was diluted at a 1:500 dilution ratio with the aforementioned antibody dilution buffer. Cells were rinsed with 1 mL cold DPBS for 5 min. Hoechst, a counterstain for the nucleus, was diluted at a 1:1000 dilution ratio with the antibody dilution buffer. Cells were incubated in 400 µL of the diluted nuclear-specific dye for 20 min at room temperature, covered with aluminum foil and placed on a plate shaker. Cells were rinsed with 1 mL cold DPBS for 5 min and resuspended in 400 µL cold DPBS before image acquisition with a Cell Observer fluorescent microscope. Images were acquired at a 20 x and 63 x magnification.

### 2.2.6 Surface and intracellular marker staining using flow cytometry

Flow cytometric staining of human peritoneal macrophages was performed simultaneously for cell surface and intracellular proteins. Table 10 shows a detailed description of the conjugated antibodies. The staining of solely surface markers is described in 2.2.11, as it differs from the co-staining with intracellular markers. A fixation and permeabilization treatment is required for the staining of intracellular markers.

Human peritoneal macrophages were washed twice after harvesting with 1 mL cold DPBS and transferred into FACS tubes. These were centrifuged at 300 x g for 5 min at 4 °C. After the supernatant was discarded, cells were resuspended in 500 µL PBS containing 0.5 µL Zombie NIR, a fixable viability dye. Cells were incubated for 20 min at room temperature in the dark. Cells were then washed twice with FACS buffer. Cells were resuspended in 50 µL of surface marker antibodies diluted in FACS buffer, supplemented with 10 % sterile-filtered human male AB serum. After antibody addition, tubes were vortexed and cells were incubated for 30 min on ice in the dark. Cells were then washed with FACS buffer and resuspended in 100 µL Cytofix/Cytoperm. Cells were incubated in Cytofix/Cytoperm for 20 min on ice in the dark. After the 20 min-incubation period, cells were washed twice with 1 mL 1 x Perm/Wash. Cells were blocked by adding 100 µL blocking reagent (10 % sterile-filtered human male AB serum diluted in 1 x Perm/Wash) for 20 min on ice in the dark. Intracellular antibodies were added

directly, tubes were vortexed after antibody addition and cells were incubated for 30 min on ice in the dark. Cells were then washed once more with 1 mL 1 x Perm/Wash and resuspended in 100 µL FACS buffer before data acquisition with flow cytometry.

Single-color compensation controls and unstained controls of peritoneal macrophages were used for the compensation setup in the flow cytometer. Compensation controls were performed using compensation beads to adjust the photomultiplier tube (PMT) voltages. Unstained cells were used to further adjust the PMT voltages, forward (FSC) and side scatter (SSC) settings and determine the gating strategy. The gating strategy comprised the removal of cell debris in the forward and side scatter plot (FSC vs SSC), doublets in the pulse geometry plot (FSC-A vs FSC-H) and dead cells with the viability dye (FSC vs Zombie NIR). Unstained cells showed background fluorescence and cellular autofluorescence, allowing for better visualization of positive cell populations.

**Table 10: Conjugated antibodies used for staining in flow cytometry**

| Antibody | Fluorochrome | Target |
|---|---|---|
| CD14 | PE | cell surface |
| CD14 | FITC | cell surface |
| CD16 | BV605™ | cell surface |
| CD68 | PE-eFluor 610 | intracellular |
| CD86 | PE | cell surface |
| CD163 | PE/Cy7 | cell surface |
| CD206 | BV421™ | cell surface |
| GATA6 | PE | intracellular |
| HLADR | FITC | cell surface |

### 2.2.7 Generation of plasma-activated liquids and cell treatment

Plasma-activated liquids (PAL) were generated using the atmospheric pressure plasma jet kINPen® (neoplas tools). The plasma jet was operated with a power and gas supply unit. The noble gas argon was applied as a feed gas with a 4 L/min flow rate. The plasma jet, which comprised a central pin-type electrode, generated a visible 9 - 13 mm long plasma effluent, of which the temperature did not exceed 40 °C. A 2 - 3 kV voltage was applied at the central electrode with a sinusoidal frequency of approximately 1 MHz.

The treatment of the culture media MEM without pyruvate occurred manually. 2 mL MEM was added to a 6-well plate. The plasma jet was positioned approximately 7 mm above the center of the well. MEM was activated for 120 s with plasma. MEM was treated with pure argon gas for 120 s as a negative control. The PAL dilutions are shown in Table 11.

Before PAL treatment, cells were washed once with warm DPBS. The volume of plasma-activated and argon-treated MEM was adjusted depending on the size of the wells. In a 48-well plate, for example, 200 µL of plasma-activated or argon-treated MEM per well was added. Cells were treated with PAL for 4 h at 37 °C and 5 % $CO_2$ before further propagation in full DMEM Glutamax for the indicated time points. Except for an apoptosis and necrosis assay, all experiments were performed with an argon-treated control, 1:2-diluted and undiluted PAL. The initial apoptosis and necrosis assay was performed with an argon-treated control, 1:5-diluted, 1:2-diluted, 1:1-diluted and undiluted PAL.

**Table 11: PAL dilutions**

| **Dilution ratio** | **e.g. 200 µL** |
|---|---|
| 1:5 | 33 µL PAL + 167 µL MEM |
| 1:2 | 67 µL PAL + 133 µL MEM |
| 1:1 | 100 µL PAL + 100 µL MEM |
| undiluted | 200 µL PAL |

### 2.2.8 Apoptosis, necrosis: Apotracker and 7-AAD co-staining

Apoptosis and viability was measured in the flow cytometer by co-staining Apotracker, similar to Annexin V, with 7-AAD, a membrane impermeant dye in viable cells.

Human peritoneal macrophages were washed twice after harvesting with 1 mL cold FACS buffer and transferred into FACS tubes. Cells were centrifuged at 300 x g for 5 min at 4 °C and the supernatant was discarded. The 80 µM Apotracker stock solution was diluted at a 1:10 dilution ratio with FACS buffer and 5 µL of the diluted reagent was added to the cell suspension in 100 µL FACS buffer to yield a final concentration of 400 nM Apotracker staining solution. Tubes were vortexed gently and cells were incubated for 20 min at room temperature in the dark. Cells were then washed twice with FACS buffer and resuspended in 100 µL FACS buffer. 5 µL of 7-AAD viability dye was added. Cells were incubated for 10 min at room temperature in the dark before flow cytometric data acquisition. Apotracker was registered in the FITC channel.

For the gating strategy, viability was defined as the percentage of cells negative for Apotracker and 7-AAD, as these cells showed no phosphatidyl exposure or cell membrane permeability [85,86]. The co-staining allowed for the discrimination of early and late apoptotic as well as necrotic and live cells. The separation of these populations can be seen in the gating strategy as populations within the quadrants Q1 - Q4 in Figure 5. Q1 shows necrotic cells (Apo-, 7-AAD+), Q2 shows late apoptotic (Apo+, 7-AAD+), Q3 shows early apoptotic (Apo+, 7-AAD- ), and Q4 shows viable cells (Apo-, 7-AAD-). Macrophages were treated with 2 µM Staurosporine for a 2 h-incubation period and in a water bath at 80 °C for a 20 min-incubation period for positive controls of apoptosis and necrosis, respectively. These positive controls helped to determine the gating strategy and are shown in the Appendix (1).

a)

| | |
|---|---|
| **Q1**: Necrosis Apo-, 7-AAD+ | **Q2**: Late apoptosis Apo+, 7-AAD+ |
| **Q4**: Viable cells Apo-, 7-AAD- | **Q3**: Early apoptosis Apo+, 7-AAD- |

b)

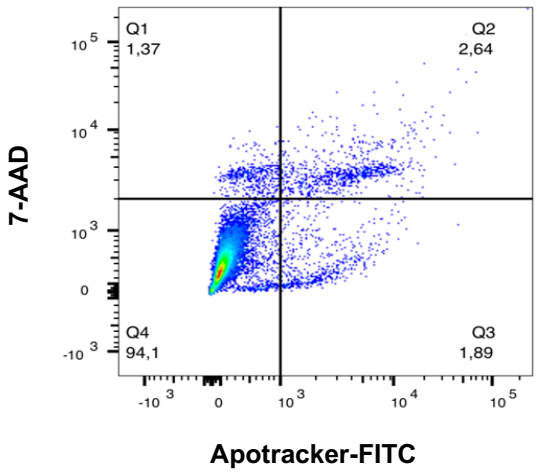


**Figure 5: Gating strategy of Apotracker and 7-AAD co-staining.** (a) Shown is the separation of early and late apoptotic as well as necrotic and viable cells as populations within the quadrants Q1 - Q4. Q1 shows necrotic cells (Apo-, 7-AAD+), Q2 shows late apoptotic (Apo+, 7-AAD+), Q3 shows early apoptotic (Apo+, 7-AAD-), and Q4 shows viable cells (Apo-, 7-AAD-). (b) Shown is an exemplary flow cytometry dot plot (Apo vs 7-AAD) of peritoneal macrophages treated with undiluted PAL. Parts of this figure were previously published in Schultze-Rhonhof et al., *Frontiers in Immunology*, 2024, under CC BY 4.0 [87].

### 2.2.9 DNA double-strand breaks: γH2A.x staining

DNA double-strand breaks (DSB) were measured by intracellular staining of histone H2A.X phosphorylation on Ser139 ($\gamma$H2A.X), a marker of DNA damage, in the flow cytometer [88]. The $\gamma$H2A.X fluorescence intensity was measured four and 24 hours after PAL treatment.

Human peritoneal macrophages were washed twice after harvesting with 1 mL cold FACS buffer and transferred into FACS tubes. Cells were resuspended in 150 µL Cytofix/Cytoperm and incubated for 20 min on ice in the dark. Cells were washed twice with 1 mL 1 x Perm/Wash. Cells were blocked by adding 100 µL blocking reagent (10 % sterile-filtered human male AB serum diluted in 1 x Perm/Wash) for 20 min at room temperature in the dark. 0.4 µL of anti-$\gamma$ H2A.X antibody was added directly, tubes were vortexed gently after antibody addition and cells were incubated for one hour at room temperature in the dark. Cells were washed once with 1 mL 1 x Perm/Wash and resuspended in 250 µL FACS buffer.

Macrophages were treated for 30 min at 25 J/m$^2$ UV light as a positive control for DSBs. Unstained cells and positive controls were used to adjust PMT voltages for data acquisition and to perform gating strategy. Gating was performed as previously described to quantify mean fluorescence intensities (MFIs) of positive cell populations.

### 2.2.10 Protein expression analysis by DigiWest multiplex protein profiling

Human peritoneal macrophages were harvested with accutase 24 hours after PAL treatment and cell pellets were frozen at -80 °C until DigiWest multiplex protein profiling was performed as previously described [89,90]. Antibody signals were measured using Luminex$^{TM}$ FlexMAP 3D$^{TM}$ Instrument System (Luminex Corporation, TX, USA). Protein bands were shown as peaks by plotting average fluorescence intensity (AFI) with the respective molecular weight of the antibody. Streptavidin conjugates were used as loading controls to normalize resulting antibody signals.

### 2.2.11 Surface marker expression

Surface marker expression was measured for the markers CD86, HLADR, CD206 and CD163 24 hours after PAL treatment in the flow cytometer. Human peritoneal macrophages were washed after harvesting with 1 mL cold FACS buffer and transferred into FACS tubes. Cells were centrifuged at 300 x g for 5 min at 4 °C and the supernatant was discarded. All antibodies were diluted at a dilution ratio of 1:50 with FACS buffer supplemented with 10 % sterile-filtered human male AB serum. 50 µL of surface marker antibodies diluted in FACS buffer was added and the tubes were gently vortexed once more after antibody addition. Cells were incubated for 30 min on ice in the dark, after which they were washed with 1 mL FACS buffer. Cells were then resuspended in 100 µL FACS buffer and 1 µL 7-AAD viability dye was added. Cells were incubated for 10 min on ice in the dark before flow cytometric data acquisition.

Similar to intracellular marker staining, single-color compensation controls and unstained controls of peritoneal macrophages were included to adjust PMT voltages. Fluorescence minus one (FMO) controls were further performed to show lack of significant spillover in other fluorescence channels. Gating was performed as previously described to quantify MFIs of positive cell populations. Gating strategy is partially shown in Figure 6. The entire gating strategy and FMO controls can be seen in the Appendix (2, 3).

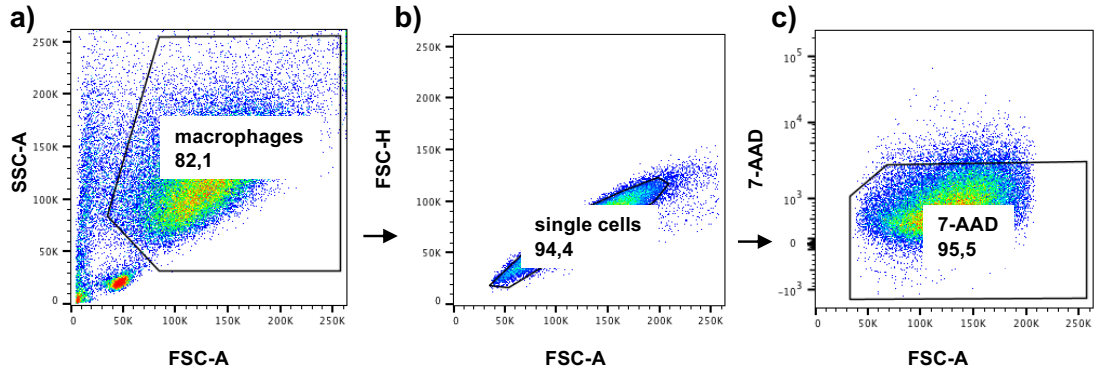


**Figure 6: Gating strategy of surface marker expression in flow cytometry.** (a) Shown is the removal of cell debris in the forward and side scatter plot (FSC-A vs SSC-A), (b) doublets in the pulse geometry plot (FSC-A vs FSC-H) and (c) dead cells with the viability dye (FSC-A vs 7-AAD). Previously published in Schultze-Rhonhof et al., *Frontiers in Immunology*, 2024, under CC BY 4.0 [87].

### 2.2.12 Cytokine and chemokine release

LEGENDplex HU Essential Immune Response Panel, a bead-based immunoassay, was used to quantify 13 different chemokines and cytokines simultaneously in the flow cytometer. The mean fluorescence intensities (MFIs) of IL-4, IL-2, CXCL10 (IP-10), IL- 1ß, TNF-∝, CCL2 (MCP-1), IL-17A, IL-6, IL-10, IFN-$\gamma$, IL-12p70, CXCL8 (IL-8) and TGF- ß1 in cell culture supernatants were measured. Supernatants were collected four and 24 hours after PAL treatment. These were centrifuged at 3000 x g for 3 min to remove cell debris and were frozen at -80 °C until analysis. The manufacturer's instructions were closely followed [91]. The standard was prepared by adding 75 µL of assay buffer to each of the six labelled polypropylene microcentrifuge tubes (C1 - C6). A 1:4 dilution was performed by transferring 25 µL from C7 (top standard) to C6. The diluted reagent was mixed well and further serial dilutions were performed. C0 contained

75 µL assay buffer. Wash buffer was prepared by diluting 25 mL of 20 x wash buffer with 475 mL distilled water.

The plate was loaded with 15 µL assay buffer and 15 µL standard or sample, respectively. Antibody-immobilized beads were vortexed and 15 µL of mixed beads were added to each well. The plate was sealed with a plate sealer and covered in aluminum foil. The plate was placed on a plate shaker at 800 rpm for 2 hours at room temperature and then stored at 4 °C overnight. The following day the plate was centrifuged at 500 x g for 5 min. Instantly after centrifugation the supernatant was discarded by quickly inverting and blotting the plate. Wells were then washed with 200 µL of 1 x wash buffer and incubated for 1 min in wash buffer. The plate was once more centrifuged at 500 x g for 5 min and an additional washing step as previously described was performed. 15 µL of detection antibodies were added to each well. The plate was once more sealed with a plate sealer, covered in aluminum foil and placed on a plate shaker at 800 rpm for 30 min at room temperature. After two washing steps, 150 µL of 1 x wash buffer was added to each well and the beads were resuspended by pipetting. Samples were then transferred into FACS tubes for flow cytometric data acquisition.

The flow cytometer settings were set as described in the manufacturer's instructions. FSC and SSC as well as PMT voltages in the APC-, FITC- and PE-channel were calibrated using predefined beads. No compensation was required. A standard or calibration curve was acquired for each of the analytes. Technical replicates (duplicates) were performed for each sample. A low flow rate and a stopping gate including 4000 events was set. LEGENDplex data analysis software was used to analyze flow cytometric data. MFIs were recorded and absolute concentrations of the analytes were determined from the acquired standard curves.

### 2.2.13 Migration analysis

A Transwell migration assay was performed 24 hours after PAL treatment to observe changes in the migratory activity of PAL-treated macrophages.

Peritoneal macrophages were reseeded at a seeding density of 8 x $10^4$ cells in 200 µL DMEM and loaded onto ThinCert cell culture inserts (upper chamber) with a 8 µm pore size. 600 µL DMEM Glutamax was added into the respective lower chamber of a 24-well plate. Cells were left to adhere for 2 hours at 37 °C and 5 % $CO_2$. Cell culture inserts were then carefully washed once with 200 µL warm DPBS and transferred to unused wells containing 600 µL MEM. 200 µL argon-treated or PAL-treated MEM was added to the cell culture inserts. Cells were incubated for 4 hours at 37 °C and 5 % $CO_2$. Cell culture inserts were then carefully washed once with DPBS, 200 µL serum-free DMEM Glutamax was added and the cell culture inserts were transferred to unused wells containing DMEM Glutamax supplemented with 20 % heat-inactivated FBS. 24 hours after PAL treatment, the wells were washed twice with DPBS. Migrated cells were stained with 600 µL CellTracker Green CMFDA diluted at 1:1000 dilution ratio with serum-free MEM, which was added to the respective wells. Cells were incubated for 30 min at 37 °C and 5 % $CO_2$. Cells were then fixed with 4 % PFA for 15 min at room temperature. Cells in the cell culture inserts were removed with a cotton swab. Cell culture inserts were transferred into unused wells containing 600 µL DPBS.

Tile scans of the migrated cells were acquired with a Cell Observer fluorescent microscope at a 5 x magnification. TIF images were imported from the ZEN blue image acquisition and analysis software to ImageJ for counting of the migrated cells to the lower chamber of the Transwell dish. Images were then converted into 16-bit greyscale images. For counting of the migrated cells, the threshold for pixel intensity and particle size was adjusted to exclude small noise pixels. The watershed tool allowed for separation of the merged cells.

### 2.2.14 Raman micro-spectroscopy

Raman micro-spectroscopy was performed for the molecular analysis at a lipid, nuclei and protein level of fixed cells. To show the effects of PAL treatment on human peritoneal macrophages, cells were reseeded at a seeding density of 3 x $10^5$ cells per glass bottom dish. After reseeding, cells were cultured for 24

hours at 37 °C and 5 % $CO_2$ and treated with PAL for four hours. 24 hours after PAL treatment, cells were fixed with 400 µL 4 % PFA for 10 min at 37 °C. Cells were covered with DPBS and stored at 4 °C in the dark until Raman analysis.

Raman imaging was performed with a customized inverted WITec Raman system using a 532 nm green laser and a CCD spectrograph with a 600 g/mm grating. Images were acquired with a 63 x apochromat water-immersion objective, an integration time of 0.1 s, a pixel resolution of 1 x 1 µm and a laser power of 50 mV. For each sample, 9 - 10 cells were measured as large area scans of different sizes due to the both elongated and round shape of the isolated human peritoneal macrophages.

Image analysis was performed using Project FIVE 5.2 software (WITEC GmbH) as previously described [63,69,92,93]. The spectral data was baseline corrected, cosmic rays were removed and the spectra was cropped from 300 to 3045 $cm^{-1}$. True component analysis (TCA), a non-negative matrix factorization-based tool, followed to identify subcellular structures, including nuclei, lipids and proteins, based on prominent spectral components. The subcellular structures were further visualized as false-color coded intensity distribution heat maps. Single spectra of the subcellular structures were extracted using masks applied to the intensity distribution heat maps.

Principal component analysis (PCA), a multivariate data analysis tool with a vector-based approach, simplified the dimensionality of the spectral data acquired to improve interpretability while reducing data loss [94]. PCA was performed using The Unscrambler x 10.5 software (Camo Software) and the NIPALS algorithm as previously described [63,69,92,93]. The fingerprint region, which ranges from 400 to 1800 $cm^{-1}$, was investigated for nuclei, proteins and lipids. A further PCA analysis for the high wavenumber region (2700 to 3100 $cm^{-1}$) was performed for proteins and lipids. PCA results are shown as score plots and loading plots. Loadings show how the original variables explain the principal components (PC) [95]. Each vector or PC shows decreasing amounts of variation in chronological order [93]. Therefore, PC-1 shows a higher amount of variation

compared to PC-2. PC (score) values are plotted against each other to show separation of data sets for the argon-treated control, 1:2-diluted and undiluted PAL. PCs were chosen based on the clustering behavior of the data sets in the score value dot plots and the biological relevance of the most prominent peaks in the respective loading plots [95].

### 2.2.15 Statistical analysis

All statistical analyses were unless otherwise stated performed using a paired student's t-test with GraphPad Prism 9.2.0 (GraphPad Software Inc., San Diego, CA, USA) after testing for normality with the Shapiro-Wilk test. *P*-values of $< 0.05$ were considered statistically significant. The data is shown as mean ± standard deviation of a minimum of three independent experiments.

# 3 Results

## 3.1 Characterization of human tissue-resident peritoneal macrophages

Human tissue-resident peritoneal macrophages isolated from peritoneal lavages were characterized with brightfield microscopy, immunostaining and flow cytometry.

### 3.1.1 Characterization using brightfield microscopy

Macrophages became increasingly adherent after isolation and increased in size. They adopted a round (Figure 7a) or elongated, fibroblast-like shape (Figure 7b) as seen in the brightfield microscope images. Pro-inflammatory, or “classically” activated, macrophages have a round form, whereas anti-inflammatory, or “alternatively” activated, macrophages develop a more elongated shape. The isolation of peritoneal macrophages yielded macrophages of different phenotypes and cell complexity.

### 3.1.2 Characterization using immunostaining

Cells were stained with CD68, a pan-macrophage marker, and Hoechst, a nuclear-specific dye, to further characterize the peritoneal macrophages. Images were acquired with a 63 x magnification. Round and elongated, fibroblast-like macrophages showed a high expression of the intracellular CD68 marker, as shown in Figures 7c and 7d. In Figure 7e, primary peritoneal fibroblasts were used as a negative control, as these showed no expression of the intracellular marker CD68.

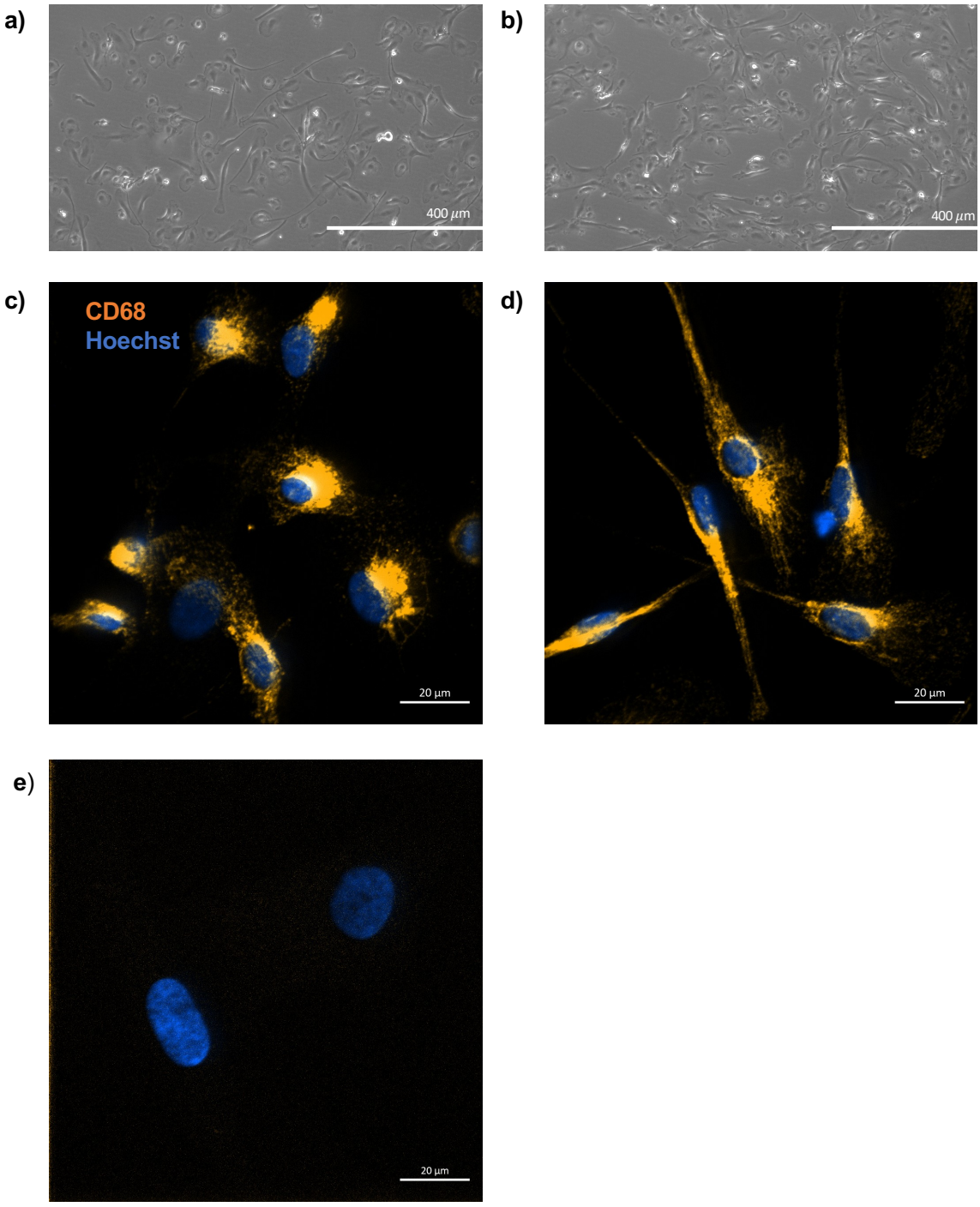


**Figure 7: Characterization of human tissue-resident peritoneal macrophages in brightfield and fluorescence microscopy.** Isolated primary macrophages from peritoneal lavages were cultured for at least five days. (a) and (b) Brightfield microscope images (10 x) were taken six days after isolation in 48-well culture plates. Macrophages showed round and elongated, fibroblast-like shapes. (c) and (d) Fluorescence microscope images (63 x) were taken five days after isolation in 35 mm high glass-bottom dishes. Macrophages were stained with CD68, an intracellular marker (orange), as well as Hoechst, a nuclear-specific dye (blue). (e) Primary peritoneal fibroblasts were used as a negative control. Scale bars represent 400 µm for brightfield microscope images and 20 µm for fluorescence microscope images. Parts of this figure were

### 3.1.3 Characterization using flow cytometry

Different surface and intracellular markers were used in flow cytometry to characterize the isolated human tissue-resident peritoneal macrophages. Surface markers included CD14 and CD16, whereas intracellular markers included CD68, as already utilized for immunostaining, and GATA6, a specific intracellular marker for tissue-resident peritoneal macrophages. Surface markers, including CD86, HLADR, CD206 and CD163, were further co-stained to characterize the isolated peritoneal macrophages based on a more pro- or anti-inflammatory phenotype.

Flow cytometry demonstrated that peritoneal macrophages represented the largest cell population of isolated cells following the plastic adherence-based isolation method from peritoneal lavages. In Figure 8a, more than 90 % of the cells were positive for CD14 (90.2 ± 0.2 %) and CD68 (93.7 ± 0.4 %) after excluding cell debris, doublets and dead cells. Dead cells were stained with 7-AAD, a membrane impermeant dye excluded from viable cells.

Figure 8b shows the flow cytometric surface marker expression of CD14 and CD16. Fewer macrophages were positive for the surface marker CD16 (61.2 ± 13.5 %) compared to CD14 (90.9 ± 1.1 %). GATA6, an intracellular peritoneal-specific macrophage marker, was expressed by 98.5 ± 0.4 % of the cells.

The percentage of cells positive for pro-inflammatory (CD86, HLADR) and anti-inflammatory (CD206, CD163) surface markers are shown in Figure 8c. Most macrophages showed a basal expression of pro- and anti-inflammatory surface markers. Peritoneal macrophages showed a higher basal expression of pro-inflammatory surface markers with 99.9 ± 0.1 % of cells expressing CD86 and 90.2 ± 5.1 % expressing HLADR. The basal expression of anti-inflammatory surface markers was lower with 58.1 ± 18.9 % of the cells expressing CD206 and 82.7 ± 11.1 % expressing CD163.

Tissue-resident peritoneal macrophages showed a high expression of CD14, CD16 and the peritoneal-specific marker GATA6. Co-expression of the pro- and anti-inflammatory surface markers reveals the heterogenous nature of tissue-resident peritoneal macrophages in a homeostatic environment.

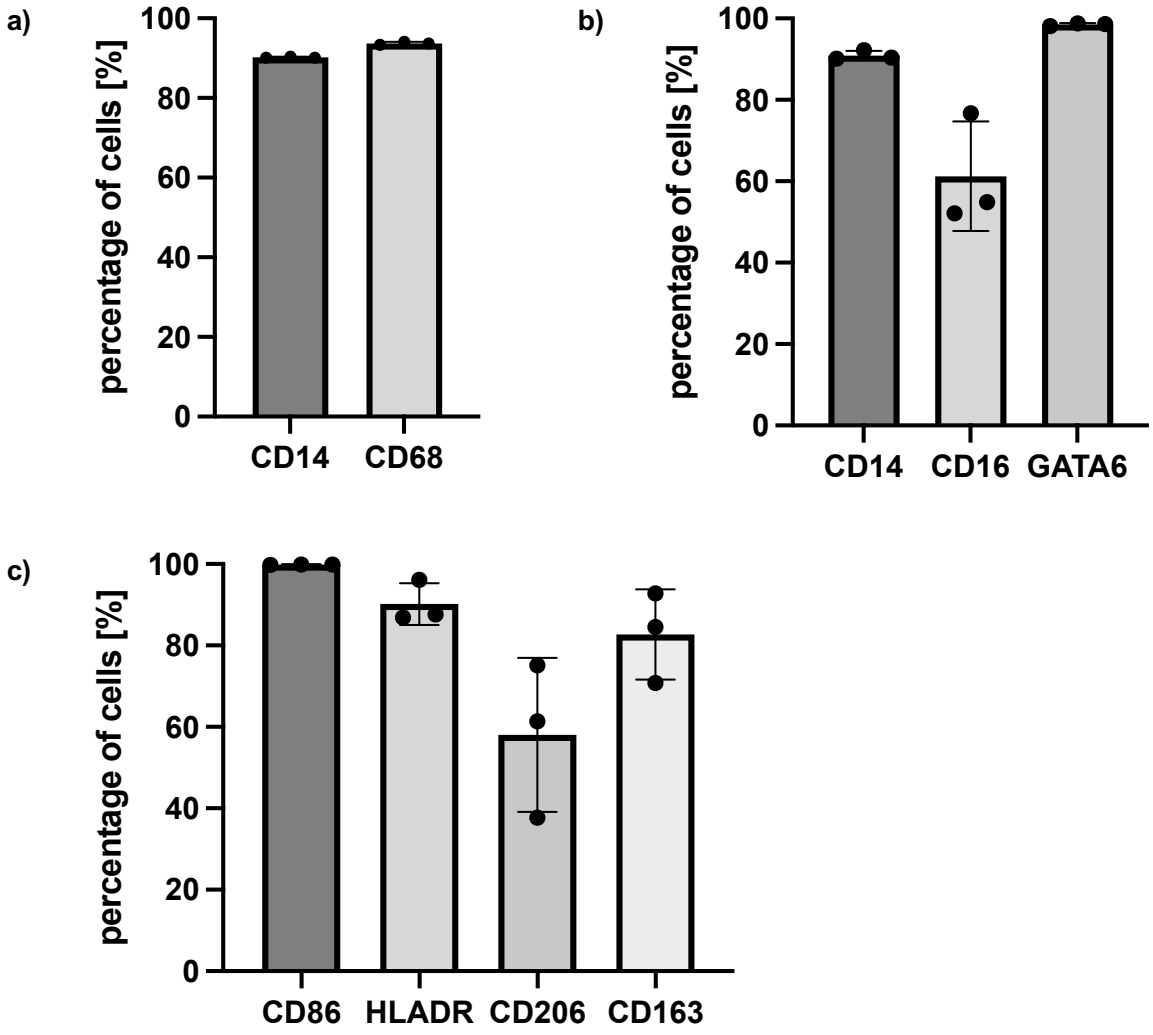


**Figure 8: Characterization of human tissue-resident peritoneal macrophages in flow cytometry.** Isolated primary macrophages from peritoneal lavages were cultured for at least five days. (a) Bar graph shows the percentage of cells positive for CD14 and CD68. (b) Bar graph shows the percentage of cells positive for the surface markers CD14 and CD16 and the intracellular peritoneal macrophage-specific marker GATA6. (c) Bar graph shows the percentage of cells positive for pro- (CD86, HLADR) and anti-inflammatory surface markers (CD206, CD163). Shown are mean ± SD, n = 3. Previously published in Schultze-Rhonhof et al., *Frontiers in Immunology*, 2024, under CC BY 4.0 [87].

## 3.2 Characterization of PAL-treated human tissue-resident peritoneal macrophages

A combined apoptosis and necrosis assay was used in preliminary experiments to test the dilution ratios 1:5-, 1:2- and 1:1-diluted as well as undiluted PAL on peritoneal macrophages. Previous experiments performed with the same parameters (2 mL culture media, 4 L/min gas flow, 4 h-incubation period) and equipment determined 1:2-diluted PAL as a therapeutic window for peritoneal cells if used as an anti-adhesion prophylaxis, as it showed a significant reduction in fibroblast confluence while preserving the mesothelial cell monolayer [63]. A confluence-based assay was used to determine the therapeutic window of PAL-treated fibroblasts and mesothelial cells. Such a confluence-based assay could not be reproduced for peritoneal macrophages. The dose-dependent reduction in viability and the effect of the different dilution rations (1:5-, 1:2-, 1:1- and undiluted PAL) on the apoptotic and necrotic behavior of PAL-treated macrophages are shown in the Appendix (4).

Considering the prior established therapeutic window for an anti-adhesion prophylaxis, the 1:2-diluted and undiluted PAL were selected to be further investigated for human tissue-resident peritoneal macrophages. The number of dilutions feasible for peritoneal macrophages was limited due to the relatively low number of cells isolated from the peritoneal lavages and difficult *in vitro* culture conditions.

### 3.2.1 Analysis of viability, apoptosis and necrosis of PAL-treated macrophages

The effect of PAL treatment was investigated on the viability and induction of early and late apoptosis as well as necrosis using the previously mentioned flow cytometry co-staining of Apotracker and 7-AAD. Gating allowed for the separation of cell populations as viable, early and late apoptotic as well as necrotic cells. Unstained and positive controls were used to determine the gating strategy. Figures 9c, 9d and 9e show the gating strategy and the flow cytometry dot plots of one donor for the argon-treated control, 1:2-diluted and undiluted PAL.

Quadrant 1 (Q1) shows necrotic cells (Apotracker-, 7-AAD+), Q2 late apoptotic cells (Apotracker+, 7-AAD+), Q3 early apoptotic cells (Apotracker+, 7-AAD-) and Q4 viable cells (Apotracker-, 7-AAD-). In total, four donors were measured (n = 4).

In Figure 9a, three of the four donors showed a viability over 90 % for the argon-treated control, one donor showed a viability of 86.8 %. However, all four donors demonstrated a comparable effect regarding viability, apoptosis and necrosis of PAL-treated macrophages. 24 hours after PAL treatment, the peritoneal macrophages sustained a high viability with 94.1 ± 4.9 % viable cells for the argon-treated control, 92.9 ± 7.3 % for the 1:2-diluted and 91.2 ± 7.8 % for the undiluted PAL.

Figure 9b shows the percentage of apoptotic and necrotic cells 24 hours after PAL treatment. A marginal, non-significant early and late apoptosis was induced for undiluted PAL. Paired t-tests were used for the analysis (* $p < 0.05$) after testing for normality with the Shapiro-Wilk test. As for the argon-treated control 0.9 ± 0.3 % were early apoptotic, while 1.4 ± 0.8 % and 1.2 ± 0.5 % were early apoptotic for the 1:2-diluted and undiluted PAL, respectively. Compared to the argon-treated control, of which 3.3 ± 3.4 % cells were positive for late apoptosis, the 1:2-diluted and undiluted PAL resulted in 4.0 ± 4.9 % and 5.3 ± 5.9 % late apoptotic cells, respectively. Regarding necrosis, 1.7 ± 1.6 % cells were necrotic for the argon-treated control, while 1.7 ± 1.7 % and 2.3 ± 2.1 % cells were necrotic for the 1:2-diluted and undiluted PAL, respectively. The results showed that there was no considerable increase in early and late apoptosis as well as necrosis. Accordingly, the peritoneal macrophages sustained a high viability following PAL treatment.

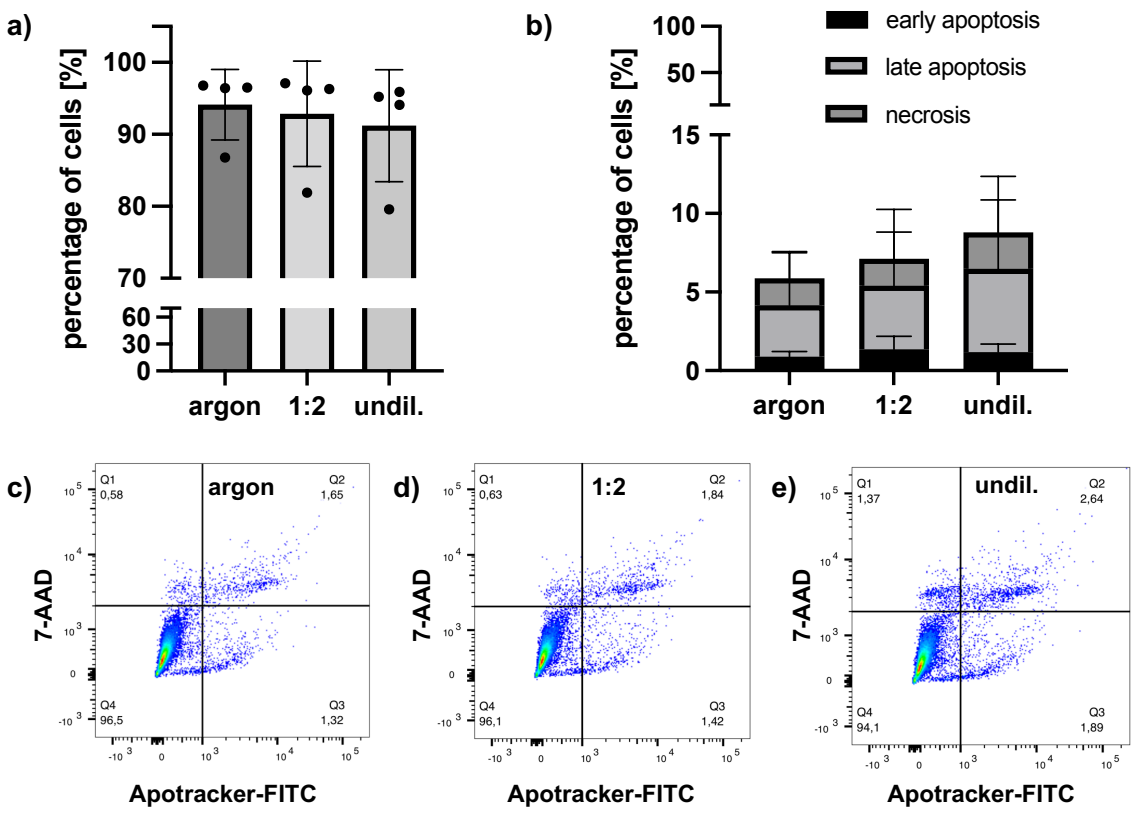


**Figure 9: Analysis of viability, apoptosis and necrosis of PAL-treated peritoneal macrophages.** Peritoneal macrophages were treated for four hours with 1:2-diluted and undiluted PAL on day four after isolation. 24 hours after PAL treatment peritoneal macrophages were stained with Apotracker-FITC and 7-AAD staining solution for flow cytometry. (a) Bar graph shows the high viability of the 1:2-diluted and undiluted PAL-treated macrophages. (b) Bar graph shows the percentage of PAL-treated macrophages early apoptotic (black), late apoptotic (light grey) and necrotic (dark grey). No significant increase in early, late apoptosis and necrosis was seen following PAL treatment. (c), (d) and (e) Flow cytometry dot plots of one donor (donor 4) are shown for the argon-treated control (c), 1:2-diluted (d) and undiluted PAL (e). Shown are mean ± SD, n = 4. Previously published in Schultze-Rhonhof et al., *Frontiers in Immunology*, 2024, under CC BY 4.0 [87].

### 3.2.2 Analysis of DNA double-strand breaks of PAL-treated macrophages

The effect of PAL treatment was further investigated on the induction of DNA-DSBs with the intracellular staining of histone H2A.X phosphorylation on Ser139 ($\gamma$H2A.X), an indicator of DNA damage. The $\gamma$H2A.X fluorescence intensity was measured using the flow cytometer four and 24 hours after PAL treatment. The mean fluorescence intensities (MFIs) of the PAL-treated macrophages are shown in Figure 10. Paired t-tests were used for the analysis (* $p < 0.05$) after testing for normality with the Shapiro-Wilk test. There was no significant increase in the

induction of DNA double-strand breaks for the 1:2-diluted and undiluted PAL compared to the argon-treated control for both time points (four and 24 hours).

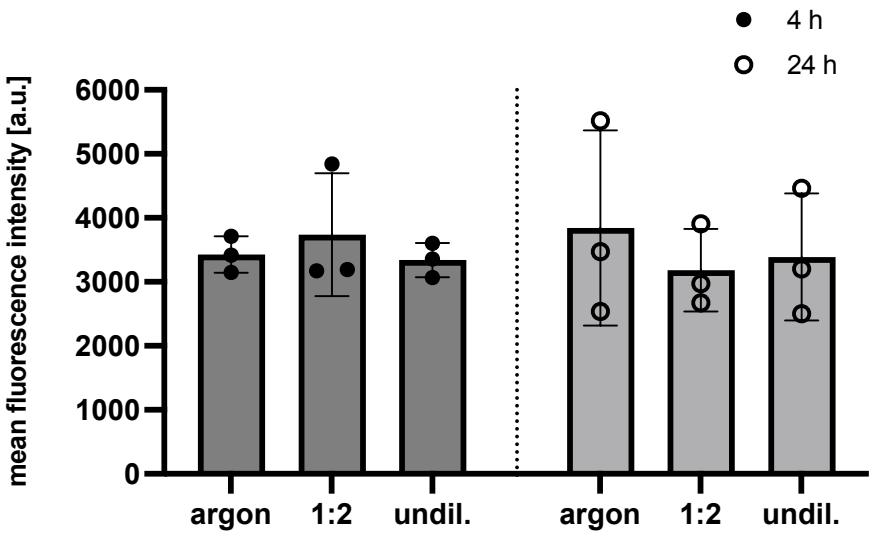


**Figure 10: Analysis of DNA double-strand breaks (DNA-DSBs) in PAL-treated macrophages.** Peritoneal macrophages were treated for four hours with 1:2-diluted and undiluted PAL on day four after isolation. No significant increase in DSBs were seen four and 24 hours after PAL treatment for the 1:2-diluted and undiluted PAL. Shown are the mean ± SD, n = 3.

### 3.2.3 Protein profiling of PAL-treated macrophages

DigiWest protein profiling, a high-throughput bead-based Western blot, was performed for further in-depth molecular characterization of PAL-derived effects on human tissue-resident peritoneal macrophages. Survival, proliferation and apoptosis markers as well as a redox-related enzyme were measured 24 hours after PAL treatment for the argon-treated control, 1:2-diluted and undiluted PAL. Cells were harvested 24 hours after PAL treatment and cell pellets were frozen at -80 °C until analysis. The average fluorescence intensities (AFIs) measured for each sample were normalized to their respective loading control (streptavidin). The AFIs and streptavidin controls are shown in the Appendix (5). Paired t-tests were used for the analysis (* $p < 0.05$) after testing for normality with the Shapiro-Wilk test.

Cellular factors related to immune response control, proliferation and pro-survival pathways, including proto-oncogene tyrosine-protein kinase (Src), S6 ribosomal

protein (rpS6) and phosphatase and tensin homolog (PTEN) showed an increased expression (Figures 11a, 11b and 11c). For PTEN and S6 ribosomal protein the upregulation was significant (PTEN: $p = 0.0252$; rpS6: $p = 0.0207$). Src showed a non-signficant increase (Src: $p = 0.0707$) for undiluted PAL compared to the argon-treated control.

The expression of effector cysteine-dependent aspartate-specific proteases (caspases, casp), casp3 and casp9, was not significantly increased in PAL-treated macrophages as shown by DigiWest protein expression profiles (casp3: $p = 0.4704$; casp9: $p = 0.4405$) (Figures 11d and 11e). Further signaling pathways related to apoptosis including p38 mitogen-activated protein kinases (MAPK) and NF-kappa B (NF-kB) were not significantly increased (p38-MAPK: $p = 0.4038$; NF-kB: $p = 0.2035$) (Figures 11f and 11g).

Superoxide dismutase, a redox-related enzyme, was moderately upregulated for undiluted PAL compared to the argon-treated control ($p = 0.1037$) (Figure 11h).

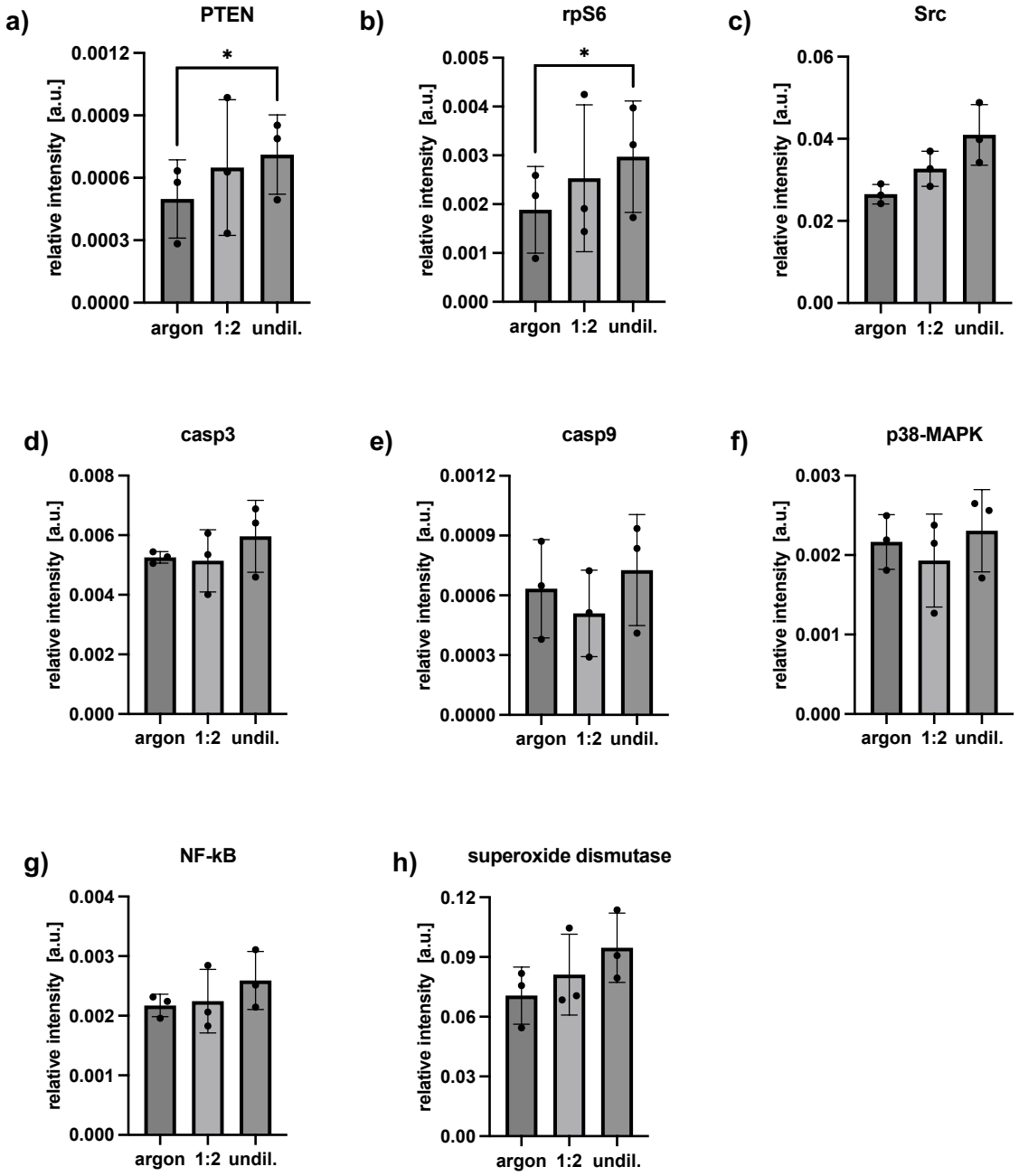


**Figure 11: Protein profiling of PAL-treated macrophages.** Peritoneal macrophages were treated for four hours with 1:2-diluted and undiluted PAL on day four after isolation. A high-throughput Western blot was performed with samples frozen 24 hours after PAL treatment. Shown are the relative intensities of the analytes normalized to their respective streptavidin loading control. (a), (b) and (c) show cellular factors related to proliferation, immune response and survival: PTEN (a), rpS6 (b) Src (c). (d), (e) and (f) show cellular factors related to apoptosis: casp3 (d), casp 9 (e), p38-MAPK (f) and NF-kB (g). (h) shows the redox-related enzyme superoxide dismutase. Shown are mean ± SD, n = 3, * $p < 0.05$. Adapted from Schultze-Rhonhof et al., *Frontiers in Immunology*, 2024, under CC BY 4.0 [87].

### 3.2.4 Analysis of surface marker expression of PAL-treated macrophages

Surface marker expression was analyzed to see whether PAL treatment can induce changes in polarization toward a pro- or anti-inflammatory phenotype in human tissue-resident peritoneal macrophages. CD86 and HLADR are pro-inflammatory markers (M1), whereas CD163 and CD206 represent anti-inflammatory markers (M2). Using the flow cytometer, the mean fluorescence intensity (MFI) was measured to quantify surface marker expression. As shown in Figure 12, there was no change in surface marker expression for CD86 and CD206 for 1:2-diluted and undiluted PAL compared to the argon-treated control. However, there was a moderate, non-significant downregulation of HLADR ($p = 0.0889$) and CD163 ($p = 0.1556$) expression for the undiluted PAL compared to the argon-treated control. A paired t-test was used for the analysis ($* p < 0.05$) after testing for normality with the Shapiro-Wilk test.

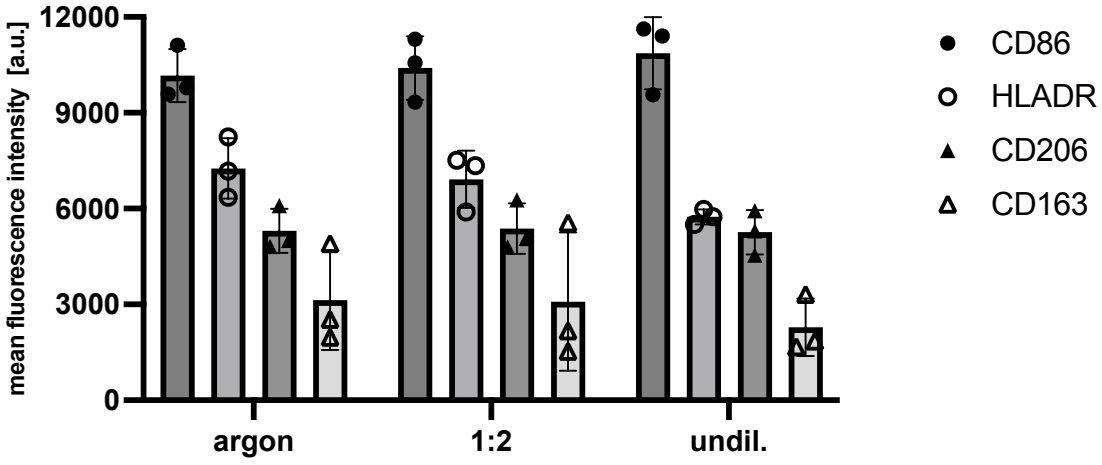


**Figure 12: Analysis of surface marker expression in PAL-treated macrophages.** Peritoneal macrophages were treated for four hours with 1:2-diluted and undiluted PAL on day four after isolation. Surface marker expression was measured 24 hours after PAL treatment. The mean fluorescence intensities (MFIs) of the different surface markers are shown. Surface marker expression of HLADR, a pro-inflammatory, and CD163, an anti-inflammatory surface marker, was moderately reduced for the undiluted PAL. Shown are mean ± SD, n = 3. Previously published in Schultze-Rhonhof et al., *Frontiers in Immunology*, 2024, under CC BY 4.0 [87].

### 3.2.5 Analysis of cytokine and chemokine release of PAL-treated macrophages

Release of cytokines and chemokines was studied to further investigate changes in the polarization profile of PAL-treated macrophages, as these intercellular

messengers are greatly involved in multiple signaling pathways, including the differentiation and polarization process of macrophages. 13 different cytokines and chemokines were measured in the culture supernatants collected four and 24 hours after PAL treatment. After four hours, the mean fluorescence intensities (MFIs) of the analytes were partially too low to be detected or further processed as concentrations. The macrophages had not been stimulated previously with, for example, LPS and IFN-$\gamma$ or IL-4 and IL-10 to boost cytokine release. However, after 24 hours seven of the 13 analytes were detectable. These included IL-2, IP-10, IL-6, IL-17, IL-10, IL-8 and MCP-1.

The standard curves were generated based on a seven-fold dilution. For the standard curves of all analytes, the curve fittings had an $R^2 > 0.99$, except for IL-17, where the $R^2 > 0.98$, which allowed for high accuracy in calculating the absolute cytokine concentrations. However, for MCP-1, the MFIs measured were higher than the standard curve range, so that the absolute concentrations could not be calculated. The average MFIs and absolute concentrations of the analytes are shown in Table 12. Figure 13 shows the averaged MFIs (duplicates) measured 24 hours after PAL treatment.

The pro-inflammatory cytokines including IL-6, IL-17 and IP-10 showed a moderate increase, especially for the undiluted PAL compared to the argon-treated control. However, changes in the cytokine/chemokine release of PAL-treated macrophages were not significant due to the high donor-dependent variance (IL-6: $p = 0.2837$; IL-17: $p = 0.4288$; IP-10: $p = 0.1426$ for undiluted PAL). The other pro-inflammatory cytokines, IL-2, IL-8 and MCP-1, showed no PAL-derived changes. The anti-inflammatory cytokine, IL-10, demonstrated a small decrease, which was higher for undiluted ($p = 0.1757$) compared to the 1:2-diluted PAL ($p = 0.2762$). IP-10, IL-8 and MCP-1 were the cytokines or chemokines with the highest average MFIs and accordingly absolute concentrations (Table 12).

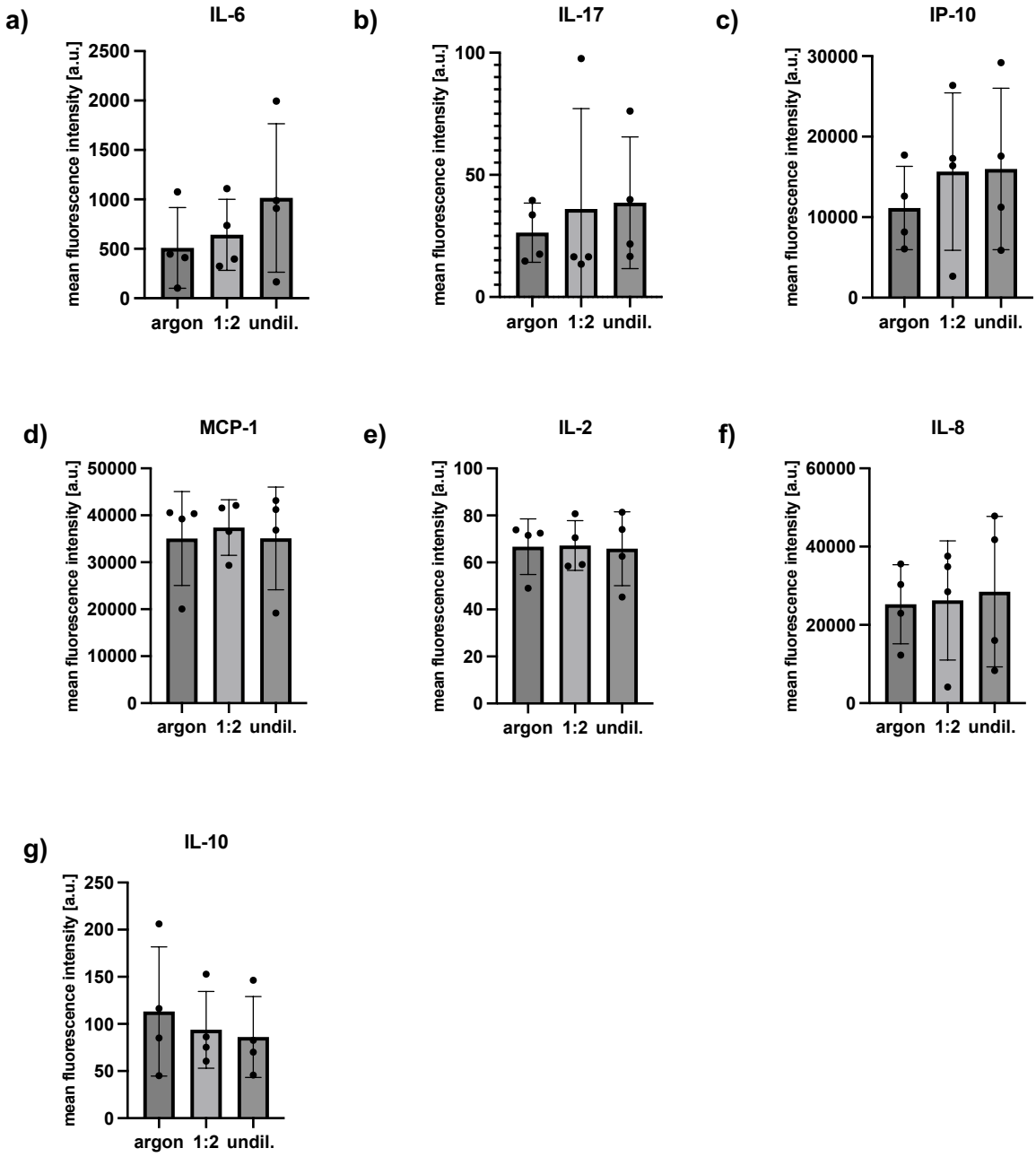


**Figure 13: Analysis of cytokine and chemokine release of PAL-treated macrophages.** Peritoneal macrophages were treated for four hours with 1:2-diluted and undiluted PAL on day four after isolation. The mean fluorescence intensities (MFIs) of the cytokine/chemokine levels were measured as duplicates in cell culture supernatants 24 hours after PAL treatment. (a), (b) and (c) A moderate increase in pro-inflammatory cytokines and chemokines, IL-6, IL-17 and IP-10, can be seen. (d), (e) and (f) Other pro-inflammatory cytokines, including MCP-1, IL-2 and IL-8, showed no changes. (g) The anti-inflammatory cytokine, IL-10, showed a moderately decreased expression. Shown are mean ± SD, n = 4. Previously published in Schultze-Rhonhof et al., *Frontiers in Immunology*, 2024, under CC BY 4.0 [87].

**Table 12: Average MFIs and absolute concentrations of cytokines and chemokines released 24 hours after PAL treatment. The following table was previously published in Schultze-Rhonhof et al., *Frontiers in Immunology*, 2024, under CC BY 4.0 [87].**

| | | average MFI [a.u.] | | | | average absolute concentration [pg / mL] | | | |
|---|---|---|---|---|---|---|---|---|---|
| **donor (n = 4)** | | 1 | 2 | 3 | 4 | 1 | 2 | 3 | 4 |
| **IL-6** | argon | 446 | 102 | 412 | 1075 | 122 | 24.7 | 112 | 281 |
| | 1:2 | 1110 | 324 | 397 | 736 | 289 | 88.6 | 108 | 197 |
| | undil. | 989 | 165 | 1995 | 909 | 260 | 43.5 | 501 | 240 |
| **IL-17** | argon | 40 | 15 | 34 | 18 | 6.67 | 1.96 | 5.63 | 2.55 |
| | 1:2 | 16 | 16 | 98 | 13 | 2.33 | 2.33 | 15.2 | 1.69 |
| | undil. | 22 | 40 | 76 | 17 | 3.41 | 6.73 | 12.3 | 2.37 |
| **IP-10** | argon | 12625 | 8152 | 17705 | 6054 | 565 | 364 | 858 | 277 |
| | 1:2 | 17276 | 16376 | 26368 | 2659 | 830 | 773 | 1618 | 148 |
| | undil. | 17597 | 11249 | 29187 | 5892 | 850 | 499 | 1980 | 271 |
| **IL-2** | argon | 72 | 49 | 74 | 72 | 5.63 | 2.73 | 5.85 | 5.74 |
| | 1:2 | 81 | 58 | 71 | 59 | 6.73 | 3.99 | 5.48 | 4.08 |
| | undil. | 74 | 45 | 81 | 63 | 5.94 | 2.22 | 6.81 | 4.52 |
| **IL-8** | argon | 30348 | 12278 | 35577 | 22954 | 1847 | 372 | 2899 | 1017 |
| | 1:2 | 34854 | 28463 | 37569 | 4120 | 2631 | 1594 | 3254 | 102 |
| | undil. | 47838 | 16048 | 41765 | 8341 | 7633 | 548 | 4549 | 223 |
| **IL-10** | argon | 116 | 45 | 85 | 206 | 9.39 | 2.65 | 6.50 | 17.2 |
| | 1:2 | 86 | 61 | 75 | 153 | 6.64 | 4.16 | 5.58 | 12.6 |
| | undil. | 70 | 46 | 83 | 146 | 5.08 | 2.70 | 6.28 | 12.1 |
| **MCP-1** | argon | 40561 | 20068 | 39247 | 40337 | >10000 | 1670 | >10000 | >10000 |
| | 1:2 | 41575 | 29348 | 42102 | 36578 | >10000 | 3809 | >10000 | 7917 |
| | undil. | 41213 | 19177 | 43148 | 36858 | >10000 | 1523 | >10000 | 8186 |

### 3.2.6 Migration analysis of PAL-treated macrophages

To investigate functional changes, the migratory activity of PAL-treated macrophages was measured using Transwell dishes. Migrated cells were stained with Cell Tracker Green.

Fluorescence microscope images were acquired at a 5 x magnification as shown in Figures 14a, 14b and 14c. Migrated cells showed clustering at the border of the Transwell dish. Instead of extracting a region of interest (ROI) at the center of the Transwell dish, all migrated cells including those at the border were counted to allow for quantification of absolute cell numbers. Reduced migratory activity of PAL-treated macrophages was already visible in the fluorescence microscope images based on their cell distribution. The absolute cell numbers of migrated cells were counted using an ImageJ macro. Figure 14d shows a moderate, non-significant decrease in migrated cells to the lower chamber of the Transwell dish for the undiluted PAL compared to the argon-treated control ($p = 0.0609$). A significant effect was seen for the 1:2-diluted PAL compared to the argon-treated control ($p = 0.0327$).

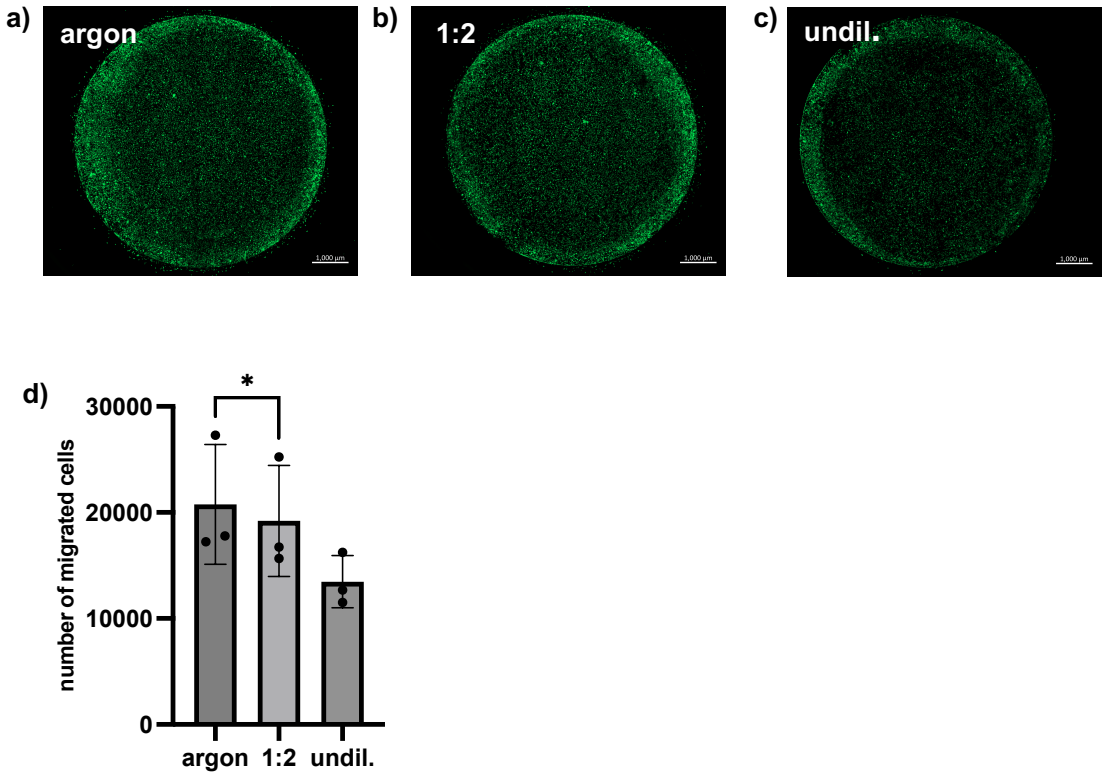


**Figure 14: Migration analysis of PAL-treated macrophages.** Peritoneal macrophages were cultured in Transwell dishes and treated with 1:2-diluted and undiluted PAL for four hours. Migratory activity was measured 24 hours after PAL treatment using Cell Tracker Green staining. Fluorescence microscope images of the argon-treated control (a), 1:2-diluted (b) and undiluted PAL (c) are shown. Images were taken using the tile function at a 5 x magnification. (d) Bar graph shows the absolute cell numbers of migrated cells to the lower chamber of the Transwell dish for the argon-treated control, 1:2-diluted and undiluted PAL. Shown are mean ± SD, n = 3, * $p < 0.05$.

### 3.2.7 Raman micro-spectroscopic analysis of PAL-treated macrophages

Peritoneal macrophages were analyzed with label-free Raman micro-spectroscopy in order to identify morphological and molecular changes at a nuclei, lipid and protein level 24 hours after PAL treatment. In total, 9-10 single cells were analyzed for each argon-treated control, 1:2-diluted and undiluted PAL of the individual donors (n = 3). True component analysis (TCA) allowed for characterization of cell components, which produced false-color coded heat maps. Representative Raman images can be seen in Figure 15a. Nuclei are colored in blue, lipids in red and proteins in green. No morphological differences at a nuclei and protein level were observed for the untreated and treated macrophages. At a lipid level discrete changes, such as slight clumping for the

macrophages treated with undiluted PAL, were visible compared to the argon-treated control.

Cell components in the TCA were identified based on specific peaks. The spectra of nuclei were determined based on distinct peaks at, for example, 785 $cm^{-1}$, 1220 to 1284 $cm^{-1}$, 1458 $cm^{-1}$ and 1655 to 1680 $cm^{-1}$. These refer to O-P-O backbone, thymine and adenine, nucleic acid modes as well as ring breathing modes of DNA and RNA bases [96-98] . The spectra of lipids could be identified based on peaks at 1078 $cm^{-1}$, 1270 $cm^{-1}$, 1460 $cm^{-1}$, 1754 $cm^{-1}$ and 3015 $cm^{-1}$, which are associated with C-C or C-O stretch, C=C groups in unsaturated fatty acids, $CH_2/CH_3$ deformation, C=O band and $\nu$=CH of lipids [99-103]. The most distinctive peaks of Raman spectra of lipids correspond to the hydrocarbon chain, which can be seen in the following regions: 1400 to 1500 $cm^{-1}$, 1250 to 1300 $cm^{-1}$ and 1050 to 1200 $cm^{-1}$ [104]. Further, the C-H stretching, as seen in bands with a high wavenumber (2800 to 3100 $cm^{-1}$), is indicative of lipid spectra [104]. The spectral components describing proteins show prominent peaks at 1008 $cm^{-1}$, 1308 $cm^{-1}$, 1453 $cm^{-1}$ and 1667 $cm^{-1}$, which refer to phenylalanine, C-N asymmetric stretching in aromatic amines, protein and C=C stretching bands [98,105-107]. A more detailed molecular assignment of the peaks for nuclei, lipids and proteins, which are seen in Figure 15b, can be found in Tables 13, 14 and 15. Figure 15b shows the average spectra of cellular components.

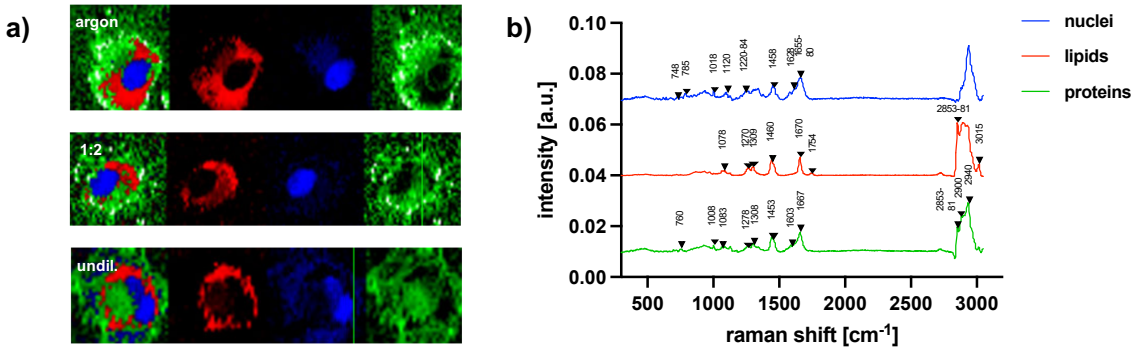


**Figure 15: Raman micro-spectroscopic analysis of PAL-treated macrophages.** (a) Representative Raman images of the TCA (True Component Analysis) are shown for the argon-treated control, 1:2-diluted and undiluted PAL. (b) A characteristic spectrum of each of the analyzed cell components was used to identify nuclei, lipids and proteins in the TCA. The fingerprint spectrum refers to the region of 600 to 1800 $cm^{-1}$. A silent region is seen from 1800 to 2700 $cm^{-1}$. From 2700 to 3100 $cm^{-1}$ further characteristic peaks can be seen, especially for lipids and proteins. Shown are the nuclei in blue, lipids in red and proteins in green. Parts of this figure were previously published in Schultze-Rhonhof et al., *Frontiers in Immunology*, 2024, under CC BY 4.0 [87].

**Table 13: Peak assignment for nuclei.**

| Peaks ($cm^{-1}$) | Assignment | Reference |
|---|---|---|
| 748 | DNA | 108 |
| 785 | uracil, thymine, cytosine, O-P-O backbone | 96 |
| 1018 | C-O stretch (ribose) | 109 |
| 1120 | C-O (ribose) | 107 |
| 1220-84 | thymine, adenine | 97 |
| 1458 | nucleic acid modes | 98 |
| 1628 | guanine carbonyl group | 110 |
| 1655-80 | thymine, guanine, cytosine (ring breathing modes) | 96 |

**Table 14: Peak assignment for lipids.**

| Peaks ($cm^{-1}$) | Assignment | Reference |
|---|---|---|
| 1078 | $\nu$(C-C) or $\nu$(C-O), phospholipids, C-C or C-O stretch (lipids) | 99,111 |
| 1270 | phospholipids, C=C groups (unsaturated fatty acids) | 100,112 |
| 1309 | $CH_3/CH_2$ twisting or bending mode (lipids) | 101 |
| 1460 | $CH_2/CH_3$ deformation (lipids, collagen) | 101 |
| 1670 | $\nu$(C=C) (*trans,* lipids, fatty acids) | 113 |
| 1754 | C=O (lipids) | 102 |
| 2853-81 | $CH_2$ symmetric stretch (lipids) & $CH_2$, asymmetric stretch (lipids, proteins) | 114 |
| 3015 | $\nu$=CH (lipids) | 103 |

**Table 15: Peak assignment for proteins.**

| Peaks ($cm^{-1}$) | Assignment | Reference |
|---|---|---|

| | | |
|---|---|---|
| 760 | tryptophan, $\delta$(ring)<br>ring breathing of tryptophan (proteins) | 97,113 |
| 1008 | phenylalanine | 105 |
| 1083 | C-N stretching mode (proteins > lipids) | 111 |
| 1278 | proteins, collagen I | 108 |
| 1308 | C-N asymmetric stretching in aromatic amines | 105 |
| 1453 | protein bands | 106,107 |
| 1603 | C=C of phenylalanine & tyrosine | 111,115 |
| 1667 | protein bands, C=C stretching | 98,106,107 |
| 2853-81 | $CH_2$ symmetric stretch (lipids), asymmetric stretch (lipids, proteins) | 114 |
| 2900 | CH stretch (lipids, proteins) | 114 |
| 2940 | C-H vibrations (lipids, proteins) | 116 |

PCA analysis, a multivariate data analysis tool, facilitated the discovery of minor spectral differences. Single spectra were extracted for each of the three cell components from the acquired single-cell large area Raman scans. These were used to perform PCA analyses at a nuclei, lipid and protein level.

The effect of PAL treatment on the molecular composition of nucleic acids was analyzed first. A PCA analysis of the extracted single spectra of nuclei was performed for the fingerprint region. No clear clustering of the argon-treated control, 1:2-diluted and undiluted PAL data sets was seen in the score values dot plot (PC-2 versus PC-3) in Figure 16a. A Mann-Whitney U test further showed no significant spectral differences in the score values of PC-2 in Figure 16b of the argon-treated control compared to 1:2-diluted and undiluted PAL. Even though no significant differences were seen in the score values for the nucleic acids, the loadings plot for PC-2 in Figure 16c showed peaks at 718 $cm^{-1}$, 788 $cm^{-1}$, 1096 $cm^{-1}$ and 1655 to 1680 $cm^{-1}$. These peaks can be assigned to nucleotides, phosphodiester bands, phosphodioxy groups and ring breathing modes of tyrosine, guanine and cytosine [96,97,100,115]. A more detailed molecular assignment of nuclei-specific peaks in the loadings plot for PC-2 can be found in Table 16.

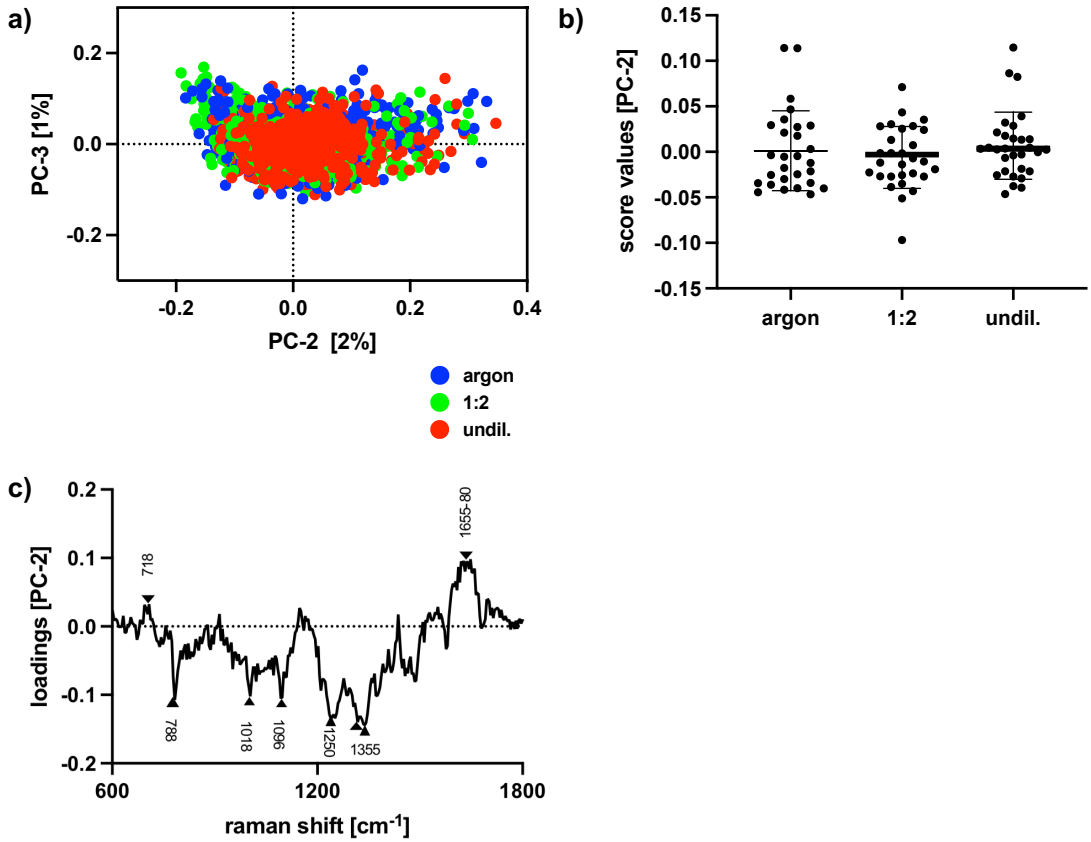


**Figure 16: Molecular analysis using Raman micro-spectroscopy at a nuclei level of PAL-treated macrophages.** Peritoneal macrophages were treated with 1:2-diluted and undiluted PAL for four hours. A molecular analysis at a nuclei level was performed on cells fixed 24 hours after PAL treatment using Raman micro-spectroscopy Results of the multidimensional data analysis are shown above. (a) Score values dot plot (PC-2 versus PC-3) of the extracted single spectra of nuclei showed no clear separation of the argon-treated control (blue), 1:2-diluted (green) and undiluted PAL (red). (b) Score values for PC-2 further showed no significant spectral differences for the argon-treated control, 1:2-diluted and undiluted PAL. (c) Loadings plot for PC-2 showed nuclei-specific peaks. A more detailed molecular assignment can be found in Table 16. Shown are individual values and mean ± SD for the 28-30 single cells from three donors. Adapted from Schultze-Rhonhof et al., *Frontiers in Immunology*, 2024, under CC BY 4.0 [87].

**Table 16: Peak assignment for nuclei in fingerprint region of PAL-treated macrophages.**

| Peaks ($cm^{-1}$) | Assignment | Reference |
|---|---|---|
| 718 | C-N (membrane phospholipid head) nucleotide peak | 115 |
| 788 | $C'_5$-O-P-O-$C'_3$ phosphodiester bands (DNA), O-P-O stretching (DNA) | 97 |
| 1018 | C-O stretch (ribose) | 109 |
| 1096 | phosphodioxy groups ($PO_2^-$) | 100 |
| 1250 | guanine, cytosine ($NH_2$) | 110 |
| 1325-30 | $CH_3CH_2$ wagging mode in guanine, adenine | 117 |
| 1355 | guanine ($N_7$, B,Z-marker) | 110 |
| 1655-80 | tyrosine, guanine, cytosine (ring breathing modes) | 96 |

After having analyzed the nucleic acids, the lipidome profile of PAL-treated macrophages was characterized in-depth. Two PCA analyses of the extracted single spectra were performed. First, one PCA analysis was performed for the regions 600 to 1800 $cm^{-1}$ and 2700 to 3100 $cm^{-1}$, excluding the silent region (1800 to 2700 $cm^{-1}$). However, the high wavenumber region (2700 to 3100 $cm^{-1}$) concealed spectral differences in the fingerprint region. Therefore, two separate PCA analyses were performed to allow for better separation of the spectral differences in the two regions.

Figure 17a shows the score values dot plot of the fingerprint region for PC-1 and PC-2. A clear separation was seen for the undiluted PAL compared to the argon-treated control data sets, while 1:2-diluted showed a greater overlap with the argon-treated control. The separation of the argon-treated control and undiluted PAL data sets was confirmed in a Mann-Whitney U test of the PC-1 score values in Figure 17b ($p < 0.0001$). An unpaired t-test of the PC-1 score values of the argon-treated control and 1:2-diluted PAL showed no significant spectral differences ($p = 0.9965$). Raman peaks that contributed to the separation in the fingerprint region, as seen in the loadings plot of PC-1 in Figure 17c, were the following: 1073 $cm^{-1}$, 1270 $cm^{-1}$, 1440 $cm^{-1}$ and 1655 $cm^{-1}$ for undiluted PAL and 1638 $cm^{-1}$ and 1697 $cm^{-1}$ for the argon-treated control.

In the score values dot plot for PC-1 and PC-2 of the high wavenumber region (Figure 18a), a distinct separation was seen for undiluted PAL compared to the argon-treated control with greater clustering of undiluted PAL along the x-axis. Again, a greater overlap was seen for 1:2-diluted PAL and the argon-treated control. The separation seen for undiluted PAL and the argon-treated control was further confirmed in a Mann-Whitney U test, which indicated significant differences in the molecular composition of lipids for undiluted PAL compared to the argon-treated control ($p < 0.0001$, Figure 18b). No significant spectral differences were seen in the Mann-Whitney U test of 1:2-diluted PAL and the argon-treated control ($p = 0.9273$). Raman peaks that contributed to the spectral differences, as seen in the loadings plot of PC-1 in Figure 18c, were: 2844 $cm^{-1}$

and 3010 $cm^{-1}$ for undiluted PAL and 2940 $cm^{-1}$ for the argon-treated control. The peaks at 1270 $cm^{-1}$, 1440 $cm^{-1}$, 1655 $cm^{-1}$ and 3010 $cm^{-1}$, which can be assigned to PAL-treated macrophages, refer to the C=C double bond of unsaturated fatty acids [100,102,112,114]. A more detailed molecular assignment of the peaks in the loadings plot for the fingerprint and high wavenumber region of PC-1 can be found in Tables 17 and 18.

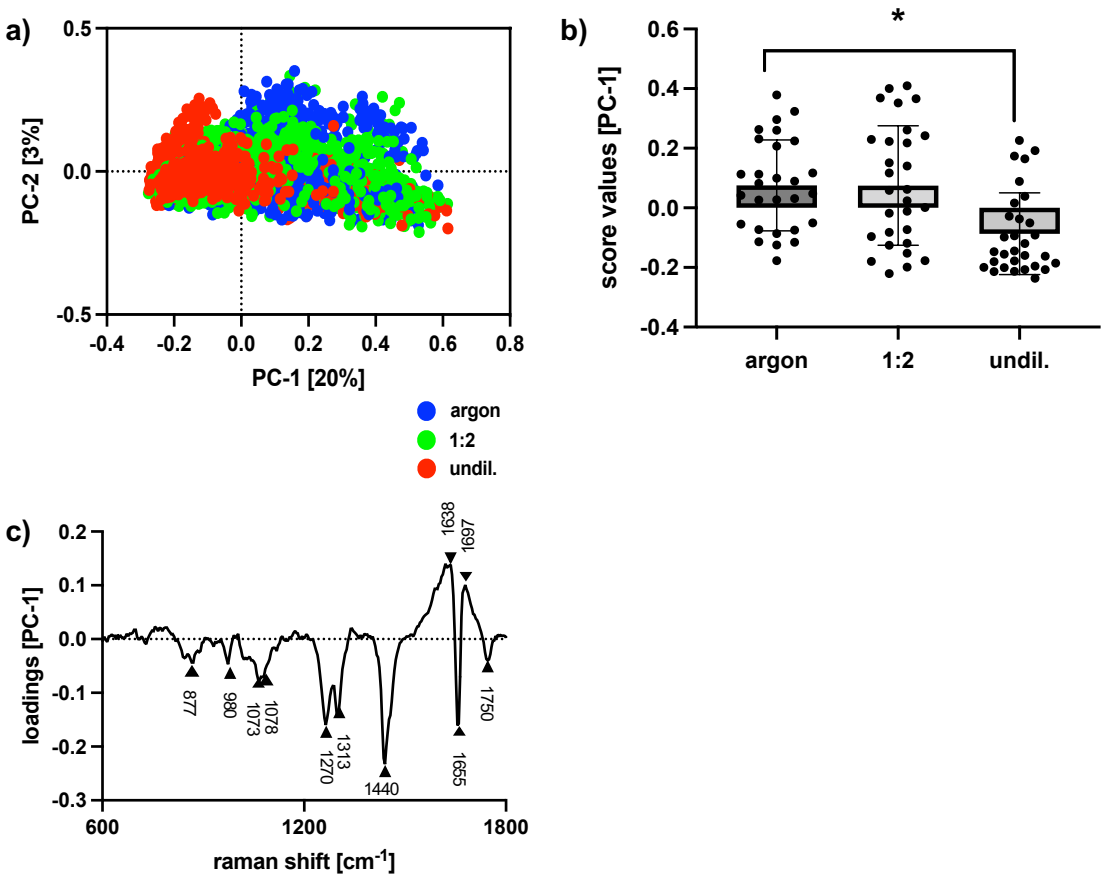


**Figure 17: Molecular analysis using Raman micro-spectroscopy at a lipid level of the fingerprint region of PAL-treated macrophages.** Peritoneal macrophages were treated with 1:2-diluted and undiluted PAL for four hours. A molecular analysis at a lipid level was performed on cells fixed 24 hours after PAL treatment using Raman micro-spectroscopy. Results of the multidimensional data analysis for the fingerprint region are shown above. (a) Score values dot plot (PC-1 versus PC-2) of the extracted single spectra of lipids showed a clear separation for the argon-treated control (blue) and undiluted PAL (red). A greater overlap was seen for the argon-treated control (blue) and 1:2-diluted (green) (b) Score values for PC-1 further showed significant spectral differences for the argon-treated control and undiluted PAL. (c) Loadings plot for PC-1 showed lipid-specific peaks. A more detailed molecular assignment can be found in Table 17. Shown are individual values and mean ± SD for the 28-30 single cells from three donors. Significant differences (*$p < 0.05$) were determined using an unpaired t-test or Mann-Whitney U test. Adapted from Schultze-Rhonhof et al., *Frontiers in Immunology*, 2024, under CC BY 4.0 [87].

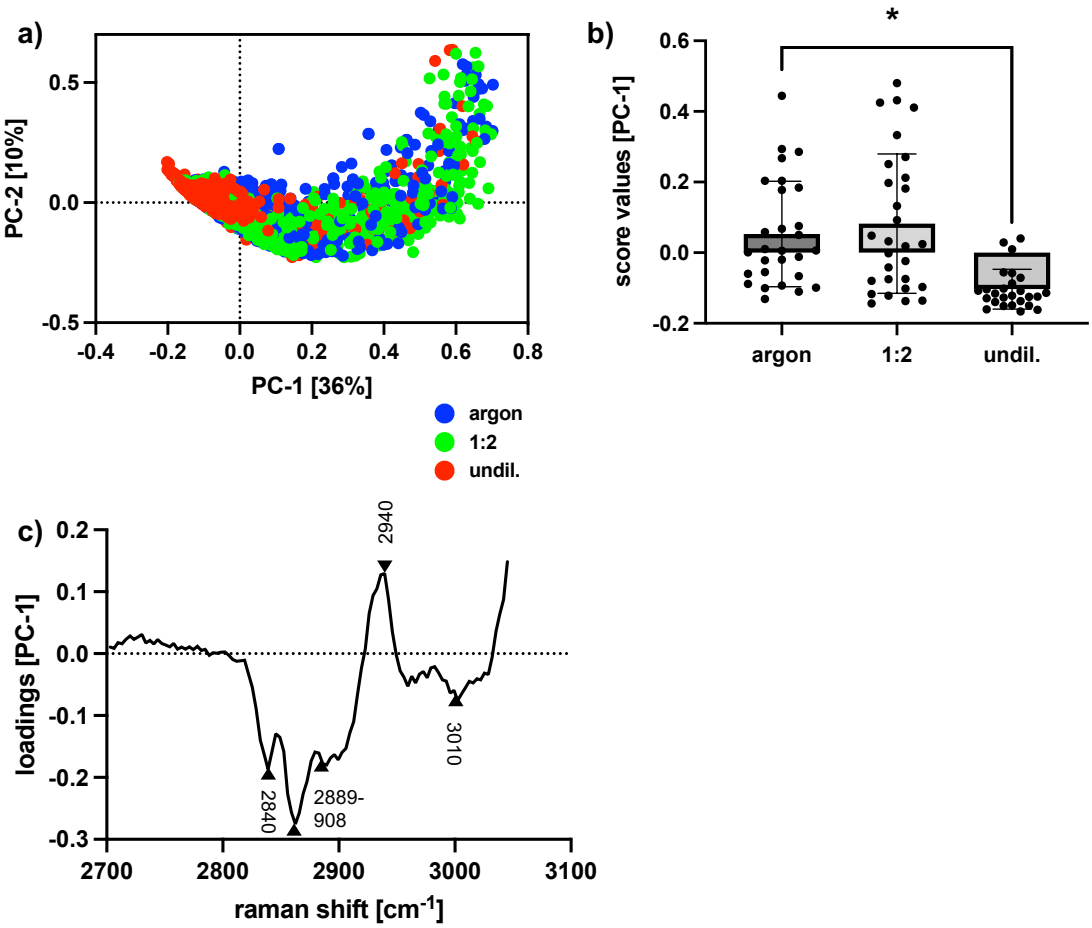


**Figure 18: Molecular analysis using Raman micro-spectroscopy at a lipid level of the high wavenumber region of PAL-treated macrophages.** Peritoneal macrophages were treated with 1:2-diluted and undiluted PAL for four hours. A molecular analysis at a lipid level was performed 24 hours after PAL treatment using Raman micro-spectroscopy. Results of the multidimensional data analysis for the high wavenumber region are shown above. (a) Score values dot plot (PC-1 versus PC-2) of the extracted single spectra of lipids showed a clear separation of the argon-treated control (blue) and undiluted PAL (red). A greater overlap was seen for the argon-treated control (blue) and 1:2-diluted (green). (b) Score values for PC-1 further showed significant spectral differences for the argon-treated control and undiluted PAL. (c) Loadings plot for PC-1 showed lipid-specific peaks. A more detailed molecular assignment can be found in Table 18. Shown are individual values and mean ± SD for the 28-30 single cells from three donors. Significant differences (*p < 0.05) were determined using Mann-Whitney U tests. Adapted from Schultze-Rhonhof et al., *Frontiers in Immunology*, 2024, under CC BY 4.0 [87].

**Table 17: Peak assignment for lipids in fingerprint region of PAL-treated macrophages.**

| Peaks ($cm^{-1}$) | Assignment | Reference |
|---|---|---|
| 877 | C-C-$N^+$ symmetric stretching (lipids) | 97 |
| 980 | =CH bending (lipids) | 97 |
| 1073 | triglycerides (fatty acids) | 118 |
| 1078 | C-C or C-O stretching mode (phospholipids) | 99 |
| 1270 | C=C groups (unsaturated fatty acids) | 100 |
| 1313 | $CH_3CH_2$ twisting mode (lipids, collagen) | 111,115 |
| 1440 | $\delta(CH_2)$ (lipids), $CH_2$ bending (lipids) | 102,114 |

| | | |
|---|---|---|
| 1638 | intermolecular bending mode of water | [111] |
| 1655 | C=C (lipids; not amide I) | [112] |
| 1697 | amide I | [102] |
| 1750 | C=O (lipids), n(C=C) (lipids, fatty acids) | [112,113] |

**Table 18: Peak assignment for lipids in high wavenumber region of PAL-treated macrophages.**

| Peaks ($cm^{-1}$) | Assignment | Reference |
|---|---|---|
| 2844 | $\nu_s$(=CH2) | [104] |
| 2853 - 81 | $CH_2$ symmetric stretch (lipids), $CH_2$ asymmetric stretch (lipids, proteins) | [114] |
| 2889-908 | $CH_2$ asymmetric stretch (lipids) | [114] |
| 2940 | C-H vibrations (lipids, proteins), $\nu_{as}CH_2$, (lipids, fatty acids) | [113,116] |
| 3010 | unsaturated =CH stretch | [100] |

Besides analyzing the nucleic acids and lipidome profile, the molecular composition of proteins of PAL-treated macrophages was further characterized. Two separate PCA analyses of the extracted single spectra were performed. As seen at a lipid level, proteins also showed bands with higher intensities in the region of 2700 to 3100 $cm^{-1}$.

In the score values dot plot of the fingerprint region for PC-2 and PC-3 (Figure 19a), the separation of the argon-treated control, 1:2-diluted and undiluted PAL data sets was not as evident as compared to the clustering seen at a lipid level. An unpaired t-test of score values of PC-2 indicated significant spectral differences for the argon-treated control and undiluted PAL in the fingerprint region ($p = 0.0024$). A Mann-Whitney U test further showed significant spectral differences for the argon-treated control and 1:2-diluted PAL ($p = 0.0263$). The Mann-Whitney U test was chosen because the Shapiro-Wilk test indicated that the data for 1:2-diluted PAL was not normally distributed. Raman peaks at 980 $cm^{-1}$, 1083 $cm^{-1}$, 1637 $cm^{-1}$ and 1685 $cm^{-1}$, as seen in the loadings plot of PC-2 in Figure 19c, explain the spectral differences of the argon-treated control and PAL-treated macrophages in the fingerprint region. Regarding peaks at 1200 to 1300 $cm^{-1}$, 1637 $cm^{-1}$ and 1685 $cm^{-1}$ PAL-treated macrophages showed vibrational changes in amide I and III bands of secondary protein structures [97,113,119].

In the score values dot plot of the high wavenumber region for PC-2 and PC-3 (Figure 20a), the limited separation seen of the argon-treated control, 1:2-diluted and undiluted PAL data sets was comparable to the fingerprint region. A Mann-Whitney U test of the score values of PC-2 for the high wavenumber region showed significant spectral differences in the argon-treated control and undiluted PAL-treated macrophages ($p = 0.0004$, Figure 20b). No significant spectral differences were seen for the argon-treated control compared to 1:2-diluted PAL ($p = 0.0505$). Raman peaks at 2850 $cm^{-1}$, 2913 to 2938 $cm^{-1}$, 2935 $cm^{-1}$ and 2980 $cm^{-1}$ give information regarding the spectral differences in the argon-treated control and PAL-treated macrophages (Figure 20c). For example, peaks at 2850 $cm^{-1}$, 2883 $cm^{-1}$ and 2935 $cm^{-1}$ indicated spectral differences in $CH_2$ symmetric stretch, $CH_2$ asymmetric stretch and $CH_3$ symmetric band in chain end [100,113,114]. A more detailed molecular assignment of the protein-specific peaks in the fingerprint and high wavenumber region can be found in Tables 19 and 20.

The lower explained variance at a protein level in the fingerprint and high wavenumber region compared to lipids correlates with the smaller separation seen in the score plots. As seen at a lipid level, the explained variance was higher in the high wavenumber compared to the fingerprint region.

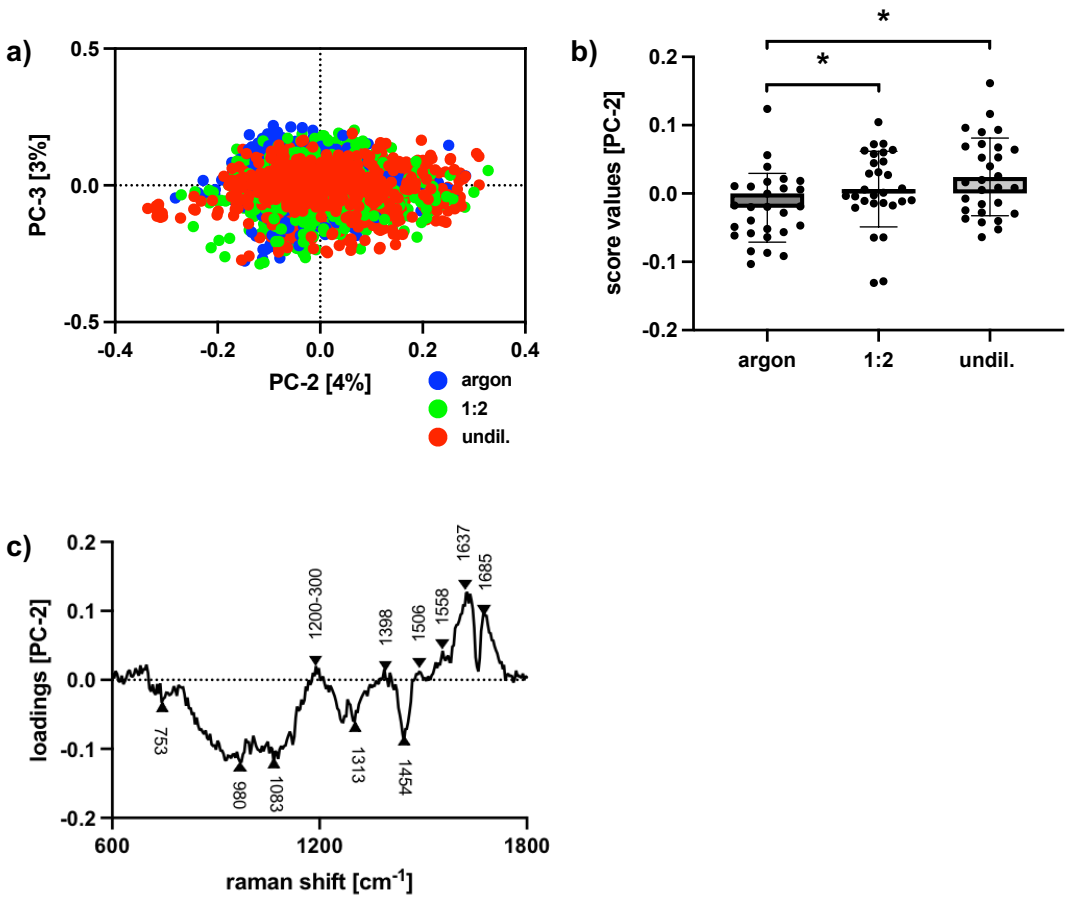


**Figure 19: Molecular analysis using Raman micro-spectroscopy at a protein level of the fingerprint region of PAL-treated macrophages.** Peritoneal macrophages were treated with 1:2-diluted and undiluted PAL for four hours. A molecular analysis at a protein level was performed 24 hours after PAL treatment using Raman micro-spectroscopy. Results of the multidimensional data analysis for the fingerprint region are shown above. (a) Score values dot plot (PC-2 versus PC-3) of the extracted single spectra of proteins showed no clear separation of the argon-treated control (blue), 1:2-diluted (green) undiluted PAL (red). (b) Score values for PC-2 showed significant spectral differences for the argon-treated control and undiluted PAL. (c) Loadings plot for PC-2 showed protein-specific peaks. A more detailed molecular assignment can be found in Table 19. Shown are individual values and mean ± SD for the 28-30 single cells from three donors. Significant differences (*$p < 0.05$) were determined using an unpaired t-test and Mann-Whitney U test.

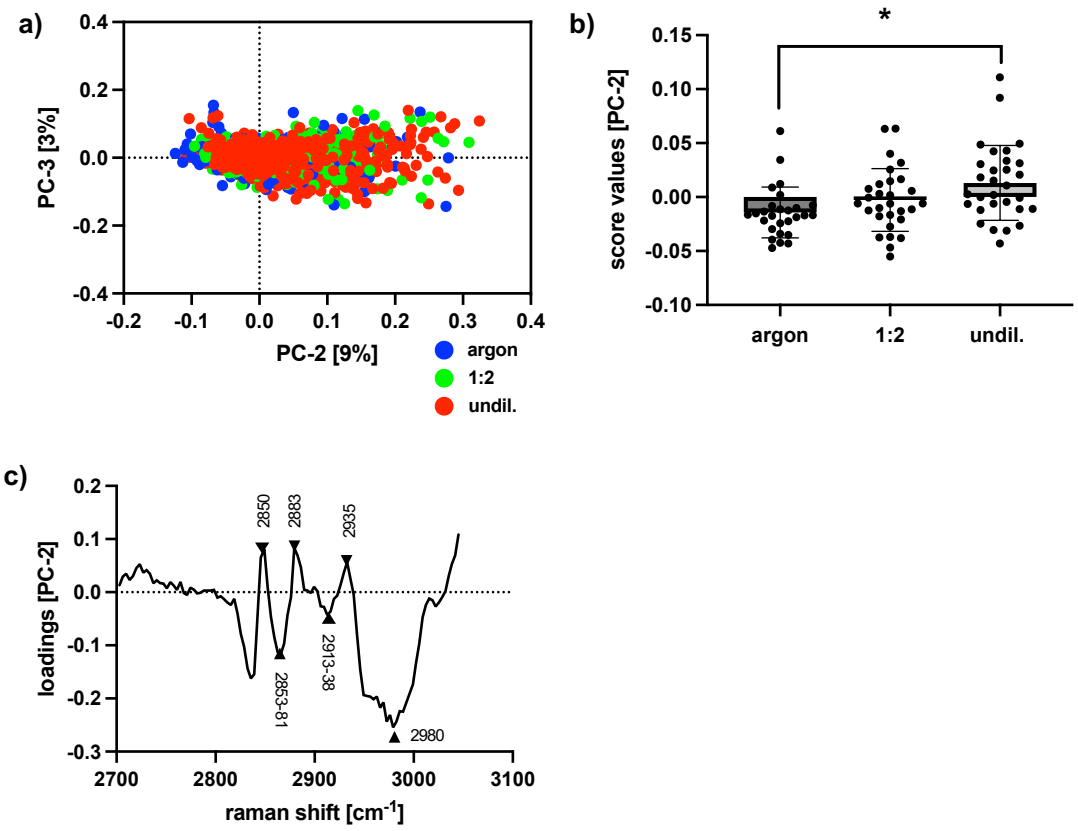


**Figure 20: Molecular analysis using Raman micro-spectroscopy at a protein level of the high wavenumber region of PAL-treated macrophages.** Peritoneal macrophages were treated with 1:2-diluted and undiluted PAL for four hours. A molecular analysis at a protein level was performed 24 hours after PAL treatment using Raman micro-spectroscopy. Results of the multidimensional data analysis for the region of high intensity bands are shown above. (a) Score values dot plot (PC-2 versus PC-3) of the extracted single spectra of proteins showed no clear separation of the argon-treated control (blue), 1:2-diluted (green) undiluted PAL (red). (b) Score values for PC-2 showed significant spectral differences for the argon-treated control and undiluted PAL. (c) Loadings plot for PC-2 showed protein-specific peaks. A more detailed molecular assignment can be found in Table 20. Shown are individual values and mean ± SD for the 28-30 single cells from three donors. Significant differences (*$p < 0.05$) were determined using Mann-Whitney U tests.

**Table 19: Peak assignment for proteins in fingerprint region of PAL-treated macrophages.**

| Peaks ($cm^{-1}$) | Assignment | Reference |
|---|---|---|
| 753 | symmetric breathing (tryptophan) | 99 |
| 980 | C-C stretching ß-sheet (proteins) | 97 |
| 1083 | C-N stretching mode (proteins > lipids) | 111 |
| 1200-300 | amide III (proteins) | 97 |
| 1278 | proteins, including collagen I | 108 |
| 1313 | $CH_3CH_2$ twisting mode (collagen, lipids) | 111,115 |
| 1398 | C=O symmetric stretch, $CH_2$ deformation | 101,119 |
| 1454 | $CH_2$ stretching/$CH_3$ asymmetric deformation overlapping asymmetric $CH_3$ bending & $CH_2$ scissoring (elastin, collagen & phospholipids) | 119,120 |

| | | |
|---|---|---|
| 1506 | N=H bending | [105] |
| 1558 | $\nu$(CN), $\delta$(NH) amide II (proteins) | [121] |
| 1637 | amide I band | [119] |
| 1685 | amide I (non-hydrogen bonded) | [113] |

**Table 20: Peak assignment for proteins in high wavenumber region of PAL-treated macrophages.**

| Peaks ($cm^{-1}$) | Assignment | Reference |
|---|---|---|
| 2850 | $CH_2$ symmetric stretch | [113] |
| 2853-81 | $CH_2$ symmetric stretch (lipids) & $CH_2$ asymmetric stretch (lipids, proteins) | [114] |
| 2883 | $CH_2$ asymmetric stretch (lipids, proteins) | [114] |
| 2913-38 | CH stretch (lipids, proteins) | [114] |
| 2935 | chain end $CH_3$ symmetric band | [100] |
| 2980 | $\nu_{as}(CH^{\alpha,\alpha'})$ | [122] |

Raman micro-spectroscopy allowed for the characterization of plasma-treated macrophages at a nuclei, lipid and protein level. Significant spectral differences were seen at a lipid and protein level for undiluted and partially for 1:2-diluted PAL. No significant effects were seen at the nuclei level, correlating with previous experiments, as no significant DNA double-strand breaks, apoptosis or necrosis was induced after PAL treatment for the 1:2-diluted and undiluted PAL.

# 4 Discussion

Tissue-resident macrophages contribute to the defense against bacterial infection, tumor dissemination and tissue injury within the peritoneal cavity [123]. In the presence of peritoneal cancer, the differentiation and polarization profile of infiltrating monocytes and macrophages is altered towards the predominantly M2-like, tumor-promoting phenotype of TAMs via cytokines and chemokines released from cancer and stromal host cells [31,32]. Activating macrophages and blocking their phenotype switch may thus present a potential target for an immunotherapeutic approach with PAL to reduce tumor growth and dissemination [74,124]. After peritoneal injury, LPMs attach to tissue defects within seconds [50], initiating an inflammatory response via their GATA6-driven transcriptional program [123]. The use of PAL as an anti-adhesion prophylaxis has been described in a study by our laboratory group, which examined the effects of PAL on the cell type-specific response of human peritoneal fibroblasts and mesothelial cells [63].

This thesis will discuss the use of PAL as an anti-tumoral agent and anti-adhesion prophylaxis at a macrophage level. PAL potentially represents a novel, effective preventive treatment option that is easily applicable and has demonstrated low side effects in other clinical applications [69,125].

## 4.1 PAL treatment as an anti-tumoral immunotherapeutic approach

Even though considerable progress in multimodal treatment (e.g., CRS, HIPEC or PIPAC) has been made, peritoneal recurrence rates remain high, with a median survival rate of three to six months following the recurrence of gastric cancer [1,126]. The long-term survival benefit is also uncertain since HIPEC is related to severe postoperative complications (e.g., adhesive ileus, systemic sepsis, digestive fistula) [126]. PAL may thus represent an adjuvant treatment option for peritoneal metastasis, allowing for lower adverse effects, tissue preservation and minimal cytotoxicity towards benign cells [69,74]. PAL was further

described as non-mutagenic and did not significantly alter the blood plasma anti-oxidant level [127].

Long-term tumor control requires specific and systemic recognition and removal of cancer cells [74,128]. Initiation of ICD may contribute to prolonged and protective anti-tumoral immunity. Cancer cells experiencing ICD exhibit proteins on their cellular membrane and release biomolecular messengers, or DAMPs [129]. Common DAMPs associated with ICD are surface-exposed calreticulin as well as adenosine triphosphate and high-mobility group box 1, which are released into the extracellular environment as a chemoattractant or activating factor for APCs. The cancer-immunity cycle starts with APCs recognizing these biomolecular messengers and activating T cells in the draining lymph nodes [74,129]. However, the upregulation of “don’t eat me” signals or an immunosuppressive tumor microenvironment can lead to low T cell activation [74].

PAL treatment may modulate the immunogenicity or visibility of cancer cells and the anti-tumoral activity of immune cells [73,74]. Changes in differentiation and polarization, receptor expression, metabolism and modified cytokine or chemokine secretion profiles of immune cells may enhance pro-inflammatory immune responses targeting cancer cells [74]. Bekeschus et al. showed that *in vitro* NIPP treatment of CT26 colorectal cancer cells was associated with higher immunogenic cell surface molecules (e.g., calreticulin) [130]. Van Loenhout et al. demonstrated that the secretion of less immunosuppressive cytokines by stromal host cells following NIPP treatment led to a higher infiltration of the tumor microenvironment with pro-inflammatory immune cells [129]. These M1-like macrophages are capable of phagocytosis and lysis of cancer cells, cancer-related antigen presentation and release of pro-inflammatory cytokines (e.g., IL-6) to recruit and activate cells, such as CD8+ T and natural killer cells, required for tumor control [12]. If more macrophages, however, are skewed towards an M2-like phenotype within the tumor milieu, the lower M1/M2 ratio is associated with higher chemoresistance [131]. M2-like macrophages can release growth factors and downregulate apoptosis signaling pathways in cancer cells.

## 4.2 PAL treatment as an anti-adhesion prophylaxis for postoperative adhesions

Prevention and treatment of postoperative adhesions are the focus of intensive research. Current adhesion prevention strategies focus on optimizing surgical techniques and using anti-adhesive agents (e.g., pharmacological agents or physical barriers) [132]. Improvement of surgical techniques includes reducing surgical trauma and ischemia as well as limiting exposure of the peritoneal cavity to foreign materials (e.g., sutures or powdered gloves). Targets of these anti-adhesive agents include minimizing local inflammation and inhibiting fibrin deposition [81]. Physical barriers primarily serve as a temporary matrix, capable of separating wound surfaces during the early phase of tissue repair. SEPRAFILM (Baxter, USA), INTERCEED (Ethicon, USA) and ADEPT (Baxter, USA) have FDA approval to inhibit postoperative adhesion formation. ADEPT, a 4 % icodextrin solution, prevents injured peritoneal surfaces from adhering to surrounding tissue by producing a fluid reservoir for approximately four days within the peritoneal cavity [133]. However, physical barriers and 4 % icodextrin solution showed a higher risk of anastomosis insufficiency after bowel resection, sepsis and labial swelling [80]. Especially the insufficient evidence for these anti-adhesive agents' efficacy in clinical trials may explain the lack of widespread clinical use [81,134].

So far, the anti-adhesive effect of PAL treatment has only been investigated in a limited number of studies [63,135]. Holl et al. (2022) studied PAL-derived effects on human peritoneal mesothelial cells and fibroblasts [63]. Like fully differentiated macrophages, mesothelial cells demonstrated higher robustness against PAL-derived oxidative stress and maintained an intact cell monolayer. Conversely, fibroblasts were inhibited from over-proliferation, entered G2/M cell cycle arrest and showed a higher expression of apoptosis markers (e.g., Annexin V, casp3 and casp7).

Peritoneal wound healing, as previously described (1.3.2), requires cellular infiltration and the release of mediators by injured mesothelial cells and macrophages, which initiate the inflammatory response essential for tissue repair [45,46]. Tissue-resident macrophages represent the largest cell population within the peritoneal fluid [2]. Expansion of these macrophages has demonstrated a protective role [136]. However, a lack of peritoneal macrophages has also been shown to limit the development of adhesions [137]. Using a mouse model, Ito et al. described that tissue-resident F4/80$^{high}$ CD206$^{-}$ macrophages could form "cell barriers" to limit the exposure of injured sites by enclosing the fibrin-rich clots and preventing these damaged sites from attaching to neighboring surfaces [138]. The recruitment of macrophages to these injured tissue sites is, as previously mentioned, known as the "macrophage disappearance reaction" [17]. However, these macrophage-containing cell barriers are often insufficient to prevent complete adhesion formation, and therefore Ito et al. further proposed to boost macrophage response [138].

In addition to the role of tissue-resident macrophages in peritoneal tissue injury, Sahputra et al. showed that monocyte-derived inflammatory macrophages can potentially attenuate the formation of peritoneal adhesions by modulating inflammation, fibrin deposition and fibrinolysis [139]. Enhanced proteolytic activity of monocyte-derived macrophages can lead to the clearance of immature adhesions within 7 to 14 days after surgery. Accordingly, monocyte-derived macrophages could also remove fibrin-rich clots formed due to intraperitoneal bacterial infection [140]. These infiltrating monocytes can differentiate into tissue-resident macrophages via an intermediate population [139]. Blocking these infiltrating monocytes with antibody-mediated C-C chemokine receptor type 2 (CCR2) depletion or using monocyte-depleted murine models resulted in higher postoperative adhesion occurrence. The aforementioned studies demonstrate that infiltrating monocyte-derived and tissue-resident macrophages may regulate postoperative adhesion formation through clearance of immature adhesions or cell barrier formation [138,139]. In this study, our observations are, however, limited to tissue-resident macrophages, as the postoperative infiltrating monocytes could

not be isolated due to the removal of peritoneal lavages at an early stage of surgery in order to minimize blood contamination and intraoperative dilution of peritoneal fluid.

### 4.3 PAL-derived effects on human tissue-resident peritoneal macrophages

In this study, the commercially available plasma device kINPen® was used. Due to the potential intraoperative use of the NIPP technology (e.g., minimally invasive or open abdominal-pelvic surgery), the indirect (PAL) over the direct treatment form of NIPP treatment was selected. The plasma application parameters, including distance, volume, treatment time and culture media, were carefully chosen, as the concentration and type of RONS generated vary greatly depending on these parameters [141]. Lower concentrations of RONS are necessary for physiological processes (e.g., proliferation and differentiation), whereas higher levels can result in pathophysiological responses (e.g., apoptosis and necrosis) [74]. Hence, lower levels of PAL-derived RONS may stimulate wound repair and higher concentrations may elicit cell death for cancer treatment. 1:2-diluted and undiluted PAL were investigated to show a dose-dependent effect of PAL compared to the argon-treated control. Culture media was used as a carrier instead of a ringer-lactate solution to provide optimal culture conditions for the isolated peritoneal macrophages. The culture medium MEM was selected since the specific formulation excludes pyruvate. Tornin et al. showed that the absence of pyruvate leads to a considerable increase (10 - 100 x) in PAL-derived hydrogen peroxide ($H_2O_2$) without modifying the concentration of nitrites ($NO_2^-$), thereby intensifying the cytotoxic, anti-tumoral activity of PAL [142].

Given the role macrophages play in peritoneal tumor dissemination and tissue repair, the cell-specific response of these macrophages to PAL was investigated in terms of morphological, molecular and functional changes. Most of the peritoneal macrophages isolated in this study showed a high expression of the intracellular transcription factor GATA6, which suggests that these are highly matured tissue-resident LPMs [14,16]. The high surface marker expression of CD14

and CD16 within the largest subset of isolated peritoneal macrophages further allowed for discrimination from newly migrated blood monocytes [14]. The increased influx of blood monocytes generally follows within 24 hours after surgery [143]. The primary isolated GATA6+ macrophages from peritoneal lavages further revealed co-expression of M1 and M2 surface markers, allowing these macrophages to function as sentinel and effector cells, maintain tissue homeostasis and orchestrate wound repair [8,144]. Common surface markers identifying M1 macrophages include a high expression of the co-stimulatory molecules CD86 and HLADR, responsible for antigen presentation and T cell activation [8,12]. Higher mannose receptor CD206 and scavenger receptor CD163 expression suggests a more anti-inflammatory or M2-like phenotype associated with phagocytosis and endocytosis of haptoglobin-hemoglobin complexes [8,11,12]. TAMs have been described to highly express CD163 [145]. The density of these CD163+ TAMs corresponds to the progression of gastric cancer and peritoneal metastasis. Flow cytometric characterization of peritoneal macrophages isolated from female patients showed that 99.9 ± 0.1 % of cells expressed CD86 and 90.2 ± 5.1 % expressed HLADR, both pro-inflammatory surface markers. The basal expression of anti-inflammatory was lower than pro-inflammatory surface markers. 58.1 ± 18.9 % of cells were positive for CD206 and 82.7 ± 11.1 % for CD163. HLADR and CD163 showed a reduced flow cytometric expression in PAL-treated macrophages, while the expression of CD86 and CD206 remained largely unchanged. Perhaps no distinct phenotype switch towards a pro- or anti-inflammatory phenotype was observed since the isolated peritoneal macrophages were fully differentiated [146].

Lower surface marker expression may also be due to damage to the cellular membrane via lipid peroxidation. For example, superoxide ($O_2^{\bullet -}$) can react with nitric oxide (NO) to initiate lipid peroxidation, leading to higher membrane permeability, altered membrane fluidity and functional changes in membrane proteins [147]. Accordingly, the reduced migratory activity of PAL-treated macrophages may be due to cellular membrane changes or an altered activation state rather than due to apoptosis or necrosis. Reduced migratory activity is

characteristic of classically activated M1 macrophages [148]. Vogel et al. suggested that the activation status of macrophages may affect their ability to reorganize their cytoskeleton. M2 macrophages form filopodia and migrate more toward a chemoattractant, whereas M1 macrophages adopt a spherical morphology.

Even though PAL-derived oxidative stress may affect cellular membrane integrity and induce cell death in cancer cells [149], most PAL-treated macrophages showed high viability and minimal, non-significant apoptosis in the co-staining with Apotracker and 7-AAD. Like Annexin V, Apotracker detects externalized negatively charged phospholipids during apoptosis [85]. 7-AAD is relatively membrane-impermeant in viable cells [86], indicating that a limited number of PAL-treated macrophages experienced increased membrane permeability. Minimal, non-significant early and late apoptosis was induced for undiluted PAL, correlating with observations that fully differentiated macrophages are more resistant to RONS-derived oxidative stress and cellular death than monocytes or other leukocytes [146,150]. The robustness of peritoneal macrophages towards PAL-derived oxidative stress could be due to the moderate upregulation of the redox-related enzyme superoxide dismutase in DigiWest protein profiling. The primary ROS species produced *in vivo* from molecular oxygen include hydrogen peroxide ($H_2O_2$), superoxide ($O_2^{\bullet -}$) and hydroxyl radicals ($^{\bullet}OH$) [151]. These can lead to oxidative stress-induced damage to cellular structures, such as lipids, proteins and nuclei. Superoxide dismutase catalyzes the conversion of $O_2^{\bullet -}$ to $H_2O_2$, which can be reduced to $H_2O$ [152]. Hwang et al. demonstrated that increased superoxide dismutase expression in epithelial cells inhibited excessive inflammatory response and apoptosis by blocking p38-MAPK/NF-kB signaling in epithelial cells [152].

Further apoptosis markers and pathways in protein profiling, such as casp3 or casp9, also showed no significant upregulation in PAL-treated macrophages. Effector caspases initiate the degradation phase of apoptosis, a form of cell-programmed death, including DNA fragmentation, shrinkage of cells and blebbing of the cellular membrane [153]. Instead, cellular markers relevant for proliferation

and immune response, including Src and PTEN, showed a significantly increased expression [154,155]. PTEN, a lipid phosphatase that acts as a PI3K antagonist, leads to an enhanced inflammatory response via the release of pro-inflammatory cytokines (e.g., IL-6) [155]. Src kinase is also related to immune response control, partaking in the functional activation of macrophages and the macrophage-derived inflammatory response [154]. The low apoptosis and high viability following PAL treatment is consistent with the absence of DNA-DSBs in PAL-treated macrophages. It has been suggested that RONS can induce severe DNA damage and consequently apoptosis in cancer cells, as these show a higher expression of aquaporins than healthy cells [70,71]. These aquaporins accelerate the transport of RONS, leading to higher intracellular concentrations within cancer cells. Since Marzi et al. (2022) showed that DNA-DSBs can be observed more quickly than apoptosis and are often transient in PAL-treated cells [69], we quantified these four and 24 hours after PAL treatment via the phosphorylation of the histone H2A.X at Ser139. Raman micro-spectroscopy at a nuclei level further confirmed the absence of DNA-DSBs or induction of apoptotic or necrotic signaling pathways. Brauchle et al. identified spectral shifts for cell death stages in apoptotic and necrotic cells via Raman micro-spectroscopy [156]. However, no molecular changes were seen for the 1:2-diluted or undiluted PAL compared to the argon-treated control. The absence of significant spectral shifts at a nuclei level for PAL-treated macrophages correlates with the results seen in the Apotracker and 7-AAD co-staining, DigiWest protein profiling and H2A.X-staining.

Raman micro-spectroscopy and multivariate data analysis allowed for the biochemical characterization of PAL-treated macrophages' subcellular structures, including lipids, proteins and nuclei. The ability of Raman imaging to identify PAL-derived changes has been previously demonstrated in bacterial spores by Wang et al. and cervical tissue by Wenzel et al. [157,158]. Proteins and lipids have been described as the cellular structures, which are the most reactive to indicate macrophage activation in Raman micro-spectroscopy [159]. Statistical analysis of PC score values confirmed significant separation in the proteome and lipidome profile of argon-treated and PAL-treated macrophages. Vibrational

changes in the amide I and III bands (1200 to 300 $cm^{-1}$, 1637 $cm^{-1}$ and 1685 $cm^{-1}$), which determine the secondary structures of proteins, contributed to the spectral differences [97,113,119].

Further in-depth analysis of the composition of lipids showed that Raman peaks at, for example, 1270 $cm^{-1}$, 1440 $cm^{-1}$, 1655 $cm^{-1}$, 2855 $cm^{-1}$ and 3010 $cm^{-1}$, contributed to the separation seen in the score plots for the argon-treated control and PAL-treated macrophages. These peaks can be assigned to PAL-treated macrophages and refer to the C=C double bond of unsaturated fatty acids [100,102,112,114]. PAL treatment, therefore, may significantly alter the degree of saturation in the fatty acid composition of macrophages. Montenegro-Burke et al. showed that macrophage phenotypes differ in fatty acid composition using fluid chromatography and mass spectroscopy [160]. Higher intensities of triglycerides (TGs), diacylglycerols and cholesterol esters, which are stored as lipid droplets, are distinctive of the lipidome profile of M1 macrophages [161]. Regarding triglycerides, M1 macrophages have higher proportions of unsaturated triglycerides (i.e. double bonds in the fatty acyl chains), especially polyunsaturated fatty acids (PUFA)- containing triglycerides. Triglyceride and cholesterol ester-containing lipid droplets are required for inflammatory functions and may serve as substrate pools for pro-inflammatory cytokines (e.g., IL-1ß and IL-6) [161,162]. The lipidome profile, particularly the fatty acid turnover, is related to metabolic shifts in macrophage polarization [95,163].

Consistent with the changes seen in Raman micro-spectroscopy regarding lipid composition, we were able to demonstrate that PAL-treated macrophages showed a moderate increase in pro-inflammatory cytokines and chemokines, including IP-10, IL-6 and IL-7, and a non-significant decrease in the anti-inflammatory cytokine IL-10. IP-10, for example, demonstrated immunomodulatory activity by recruiting APCs or activated T cells in melanoma and glioma murine tumor models [164]. However, IP-10 or CXCL10 may also be involved in tumor progression if the corresponding receptor CXCR3 is upregulated in cancer cells. Our observations of PAL-derived changes in cytokine

release correlate with the findings of Cheng et al., as they demonstrated higher IL-2 and IL-6 and lower IL-10 release 30 s after macrophage treatment with NIPP [165]. Arndt et al. further showed that NIPP treatment significantly increased pro-inflammatory cytokine release (e.g., IL-6, IL-8, MCP-1) by fibroblasts [166]. They proposed that the higher levels of these aforementioned signaling molecules may lead to a faster and improved immune response in the inflammatory phase of wound repair.

Improved immune response in the inflammatory phase may lead to a higher percentage of monocyte-derived inflammatory macrophages recruited to the peritoneal cavity. These SPMs may attenuate the formation of postoperative adhesions by modulating fibrin deposition and fibrinolysis [139]. In contrast, tissue-resident peritoneal macrophages can help to remove cell debris and form a cell barrier [138]. McFarland-Mancini et al. demonstrated the importance of IL-6 signaling for wound healing [167]. Wound healing was slower in IL-6-deficient mice due to compromised macrophage infiltration, more cellular debris or fibrin deposition and delayed re-epithelialization. Tager et al. revealed that IP-10, which was moderately increased in PAL-treated peritoneal macrophages, can limit the occurrence of pulmonary fibrosis [168]. Increased pulmonary fibrosis was observed in IP-10-deficient mice after bleomycin application, as IP-10 may prevent fibroblast accumulation by reducing their migratory activity. While the changes in cytokine release of PAL-treated peritoneal macrophages were predominantly associated with a pro-inflammatory shift, the cytokine secretion profiles were very donor-dependent and dynamic. Quantitative variability of these cytokine secretion profiles has also been described in other studies and can, for example, be observed based on sampling time point [74].

Tissue-resident peritoneal macrophages are highly resistant to plasma-derived oxidative stress by upregulating anti-oxidative mechanisms. NIPP can, however, trigger a moderate pro-inflammatory response in macrophages by altering their lipid and protein composition, as shown with label-free Raman micro-

spectroscopy. A NIPP-modulated cellular response may thus further facilitate the already shown anti-tumoral and wound healing properties at a macrophage level.

## 5 Summary

This thesis investigates PAL-derived effects on tissue-resident human peritoneal macrophages, as this cell population may present a potential target to limit tumor dissemination and postoperative adhesions within the peritoneal cavity.

Since most studies have investigated human blood-derived monocytes and murine macrophages [14], we wanted to investigate PAL-derived molecular, functional and immunomodulatory effects on tissue-resident human peritoneal macrophages. In this study, the isolated macrophages were characterized with immunostaining and flow cytometry. Even though PAL only had limited effects on human peritoneal macrophages regarding apoptosis, viability and DNA double-strand breaks (DNA-DSBs), the exposure to reactive oxygen and nitrogen species (RONS) actively triggered a cellular response. PAL treatment induced moderate upregulation of the redox-related enzyme superoxide dismutase and significant upregulation of cellular factors (PTEN, Src and rpS6) related to immune control, proliferation and survival, as seen in DigiWest protein profiling. Label-free and marker-independent Raman micro-spectroscopy further confirmed significant spectral changes in the proteome and lipidome profile of PAL-treated macrophages. An altered lipid composition regarding polyunsaturated fatty acid (PUFA)-containing triglycerides was observed based on spectral shifts and contributed to the moderate release of pro-inflammatory cytokines (e.g., IP-10, IL-6 and IL-17).

The high intrinsic anti-oxidant potential of fully differentiated macrophages to upregulate pro-survival signaling pathways against oxidative stress explains the limited effect of PAL treatment on macrophages. Their cellular response and skew towards a pro-inflammatory phenotype with anti-tumoral activity after PAL treatment should be further investigated in co-culture models with cancer cells or *in vivo.*

## Zusammenfassung

Ziel dieser Arbeit war es, die Wirkungen einer PAL-Behandlung auf die im Gewebe ansässigen peritonealen Makrophagen zu untersuchen. Schließlich stellt diese Zellpopulation ein potenzielles Ziel dar, um eine Tumorausbreitung und postoperative Adhäsionen innerhalb der Bauchhöhle zu reduzieren.

Da die meisten Studien aus menschlichem Blut stammende Monozyten und murine Makrophagen untersucht haben [14], wollten wir die molekulare, funktionelle und immunmodulatorische Wirkung einer PAL-Behandlung auf humane, ausdifferenzierte peritoneale Makrophagen untersuchen. In dieser Studie wurden die isolierten Makrophagen mittels Immunfärbung und Durchflusszytometrie charakterisiert. Obwohl PAL nur eine begrenzte Wirkung auf ausdifferenzierte peritoneale Makrophagen hinsichtlich Apoptose, Lebensfähigkeit und DNA-Doppelstrangbrüche zeigte, löste die Exposition eine aktive zelluläre Reaktion aus. Im DigiWest-Assay war erkennbar, dass eine PAL-Behandlung zu einer moderaten Hochregulierung des Redoxenzyms Superoxiddismutase sowie zellulärer Faktoren (PTEN, Src und rpS6), die mit der Immunkontrolle, Proliferation und dem Überleben peritonealer Makrophagen im Zusammenhang stehen, führte. Die Raman Mikrospektroskopie bestätigte weiterhin signifikante Veränderungen im Proteom und Lipidom der mit PAL behandelten Makrophagen. Eine veränderte Lipidzusammensetzung (u.a. der Triglyzeride, die mehrfach ungesättigte Fettsäuren enthalten) konnten auf Basis von Spektralverschiebungen beobachtet werden und trug zur moderaten Freisetzung proinflammatorischer Zytokine (z. B. IP-10, IL-6 und IL-17) bei.

Das hohe intrinsische antioxidative Potenzial der ausdifferenzierten Makrophagen bei oxidativem Stress erklärt die begrenzte Wirkung einer PAL-Behandlung auf Makrophagen. Die zelluläre Reaktion der Makrophagen und deren Tendenz zum proinflammatorischen Phänotyp mit antitumoraler Wirkung nach einer PAL-Behandlung sollte in Ko-Kulturmodellen mit Krebszellen oder *in vivo* weiter untersucht werden.

# 6 Appendices

**Appendix 1:** Apotracker and 7-AAD co-staining controls. (a) Flow cytometry dot plot shows unstained control. (b) and (c) Flow cytometry dot plot and histogram show Apotracker-FITC control. (d) and (e) Flow cytometry dot plot and histogram show 7-AAD control.

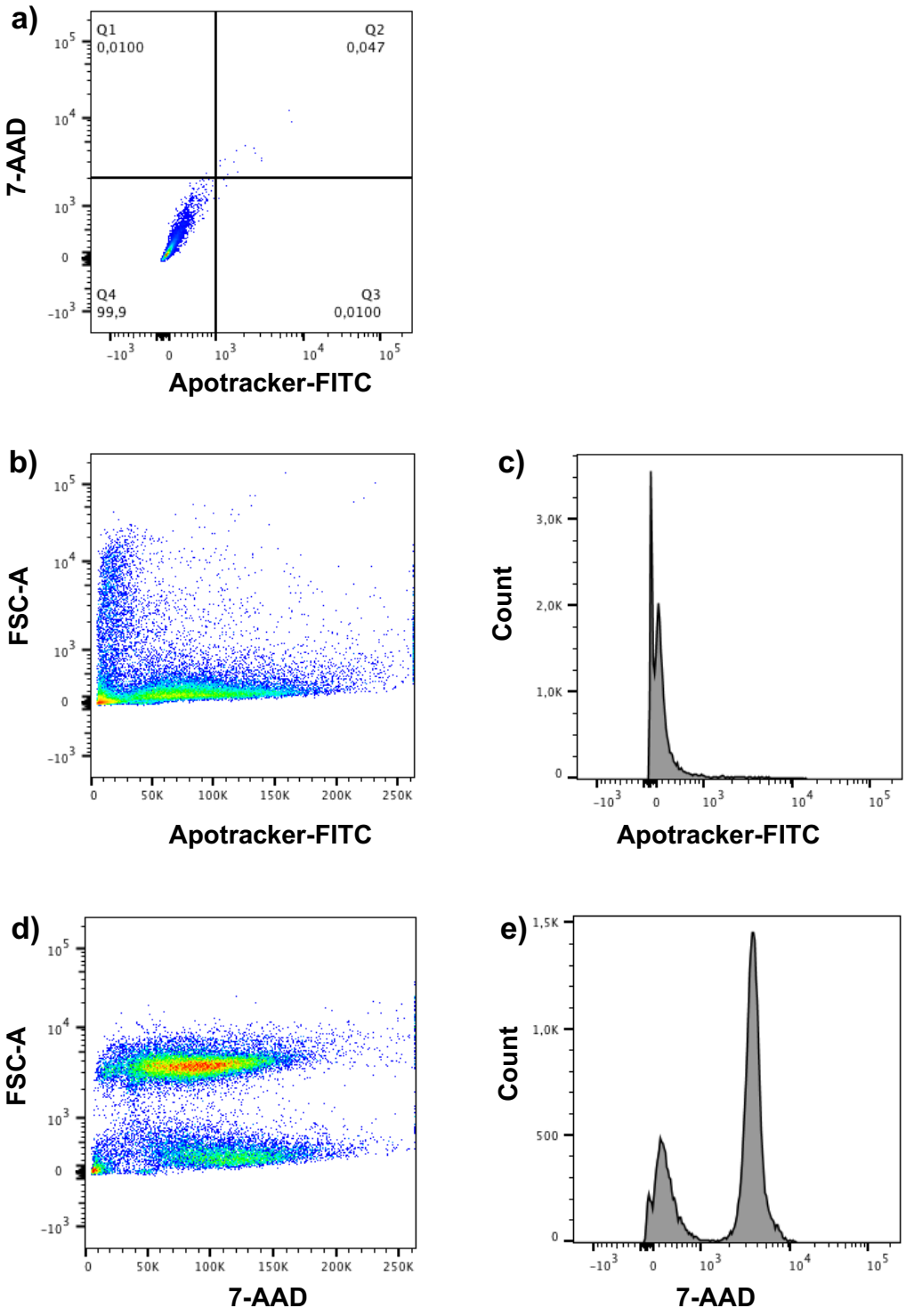

**Appendix 2:** Gating strategy for flow cytometric surface marker expression. Gating comprises the exclusion of cell debris (a), cell doublets (b) and dead cells (c). Unstained control helped to identify negative cell populations. These were used to set the gates for CD86-PE (d), HLADR-FITC (e), CD163-PE-Cy7 (f) and CD206-BV421 (g). Previously published in Schultze-Rhonhof et al., *Frontiers in Immunology*, 2024, under CC BY 4.0 [87].

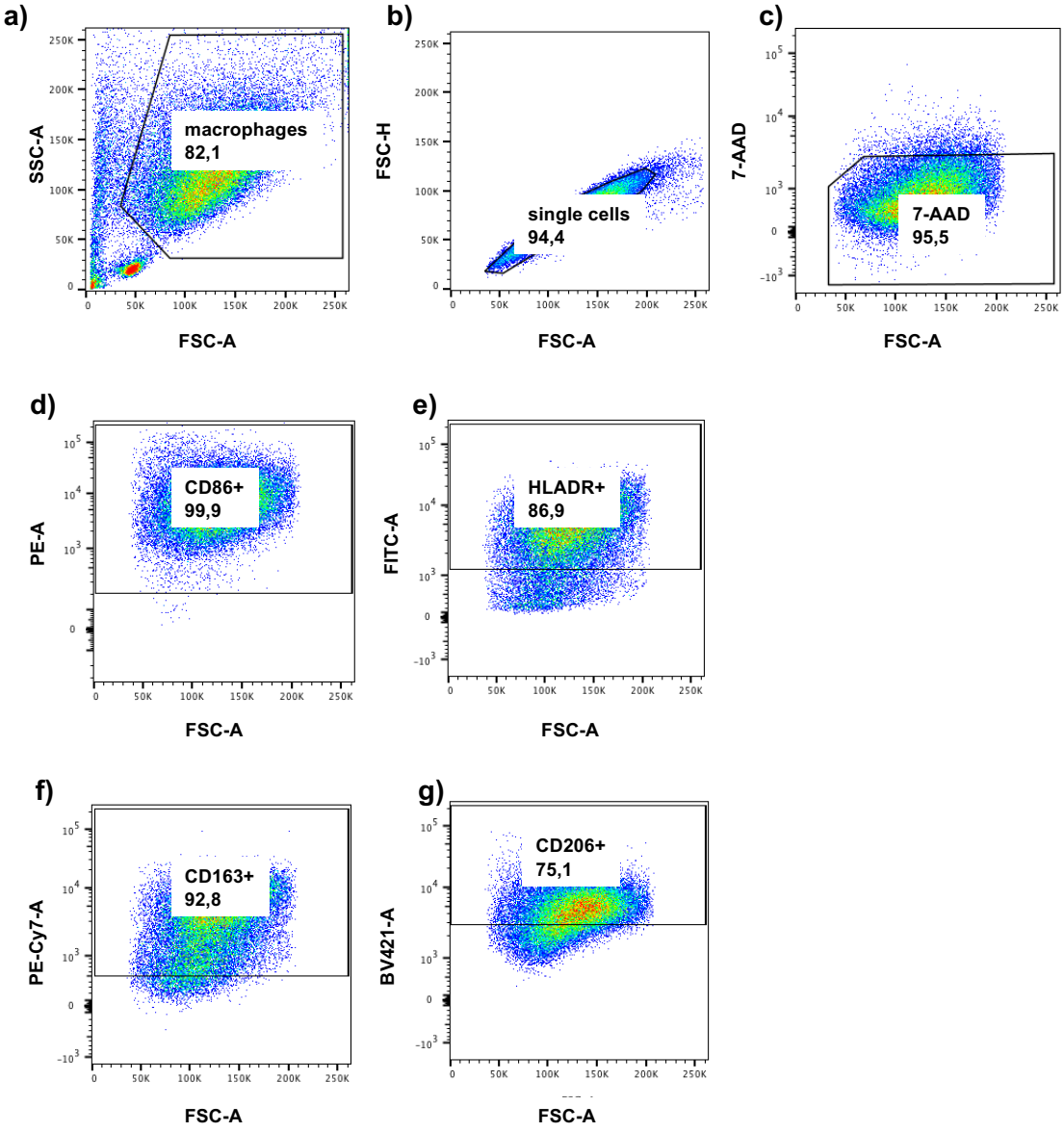

**Appendix 3:** FMO controls for flow cytometric surface marker expression. FMO controls were performed to show lack of significant spillover in other fluorescence channels.

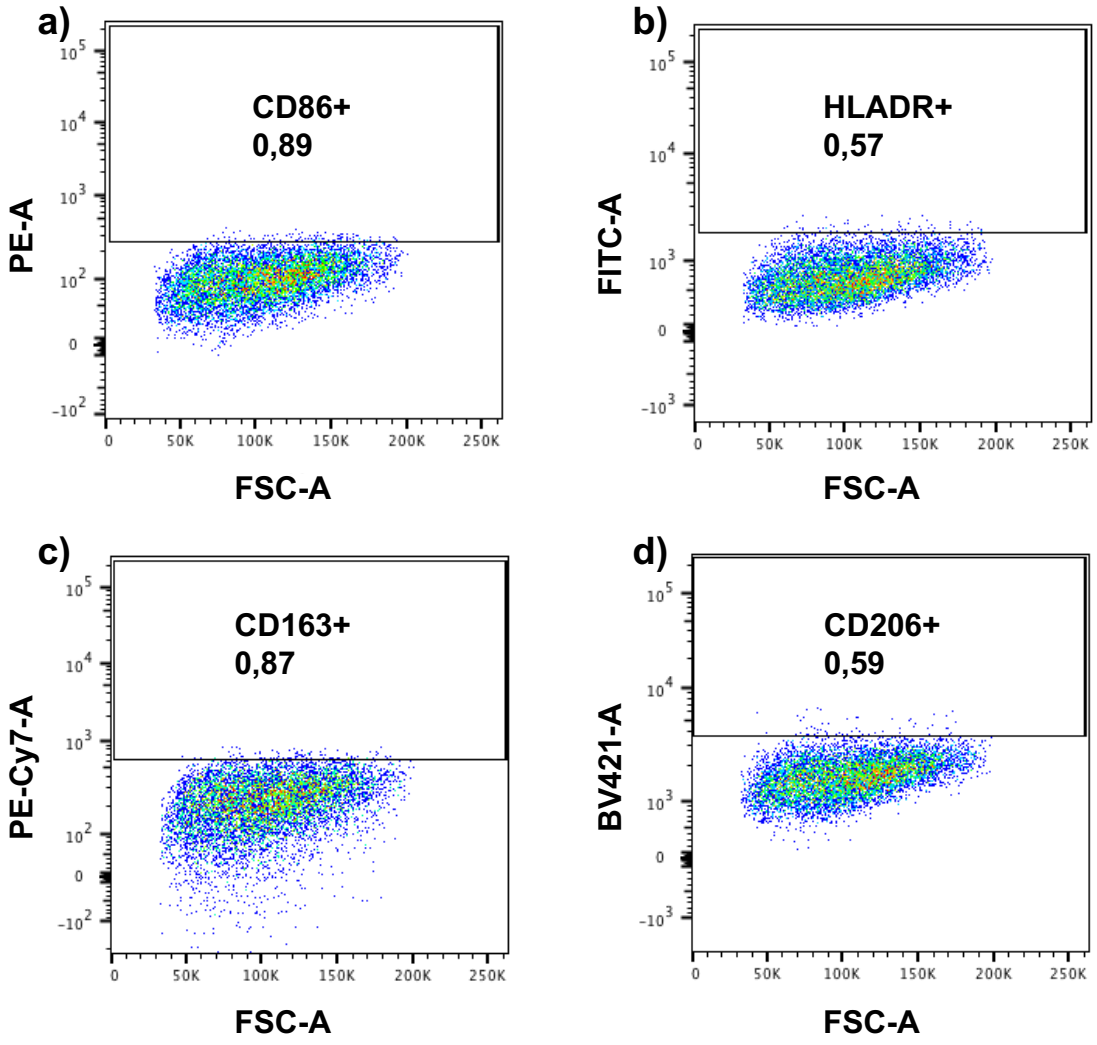

**Appendix 4:** Analysis of viability, apoptosis and necrosis of PAL-treated macrophages in preliminary experiments. Peritoneal macrophages were treated for four hours with 1:5-, 1:2-, 1:1-diluted and undiluted PAL on day two after isolation. 24 hours after PAL treatment peritoneal macrophages were stained with Apotracker-FITC and 7-AAD staining solution. (a) Bar graph shows the percentage of viable cells of the 1:5-,1:2-, 1:1-diluted and undiluted PAL following PAL treatment. (b) Bar graph shows the percentage of cells early apoptotic (black), late apoptotic (light grey) and necrotic (dark grey) following PAL treatment. No significant increase in early and late apoptosis as well as necrosis was seen following PAL treatment compared to the argon-treated control. Shown are the mean ± SD, n = 4.

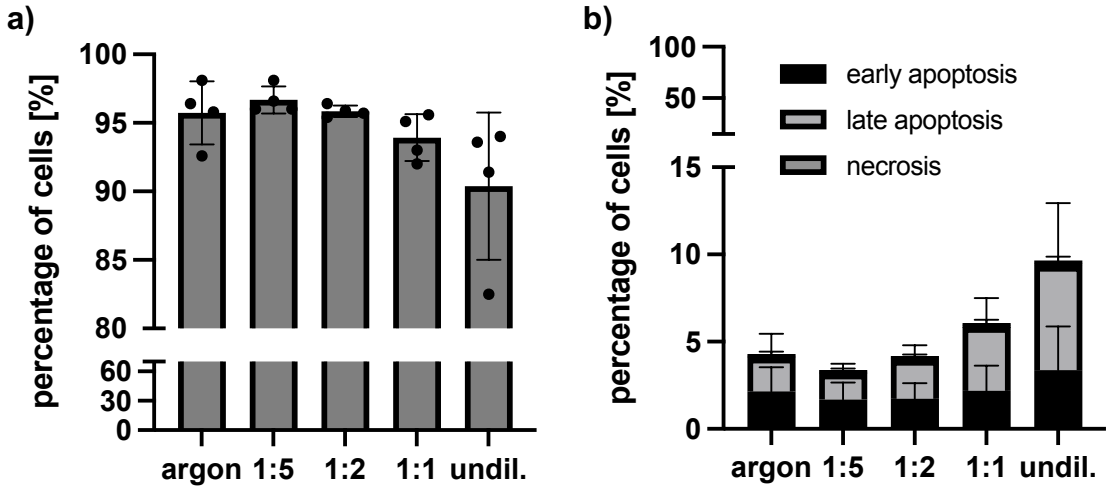

**Appendix 5:** Average fluorescence intensities of analytes and pathways measured in protein profiling using DigiWest technology.

| | | average fluorescence intensity [AFI] | | |
|---|---|---|---|---|
| **donor (n = 3)** | | 1 | 2 | 3 |
| **PTEN** | argon | 218 | 136 | 164 |
| | 1:2 | 312 | 207 | 256 |
| | undil. | 334 | 281 | 227 |
| **rpS6** | argon | 306 | 1045 | 735 |
| | 1:2 | 715 | 1183 | 1103 |
| | undil. | 732 | 1828 | 1058 |
| **Src** | argon | 9043 | 13921 | 6880 |
| | 1:2 | 18337 | 20280 | 7387 |
| | undil. | 20698 | 22614 | 9116 |
| **casp3** | argon | 1816 | 2612 | 1434 |
| | 1:2 | 2656 | 2485 | 1574 |
| | undil. | 2717 | 2612 | 1832 |
| **casp9** | argon | 300 | 182 | 184 |
| | 1:2 | 255 | 180 | 188 |
| | undil. | 354 | 233 | 249 |
| **p38-MAPK** | argon | 859 | 868 | 622 |
| | 1:2 | 1179 | 787 | 558 |
| | undil. | 1122 | 972 | 682 |
| **NF-kB** | argon | 797 | 940 | 636 |
| | 1:2 | 1023 | 1134 | 739 |
| | undil. | 1066 | 1219 | 828 |
| *streptavidin (loading ctrl)* | argon | 344236 | 479884 | 283736 |
| | 1:2 | 496244 | 619837 | 259730 |
| | undil. | 423749 | 567875 | 266247 |
| **superoxide dismutase** | argon | 17249 | 24438 | 9271 |
| | 1:2 | 34473 | 27284 | 10645 |
| | undil. | 31910 | 32783 | 12742 |
| *streptavidin* | argon | 228102 | 298807 | 170348 |
| | 1:2 | 329648 | 386819 | 155596 |
| | undil. | 280735 | 361157 | 160327 |

## 7 References


1. Cortés-Guiral D, Hübner M, Alyami M, et al. Primary and metastatic peritoneal surface malignancies. *Nature Reviews Disease Primers*. 2021;7(1):91. doi:10.1038/s41572-021-00326-6
2. Capobianco A, Cottone L, Monno A, Manfredi AA, Rovere-Querini P. The peritoneum: healing, immunity, and diseases. *J Pathol*. 2017;243(2):137-47. doi:10.1002/path.4942
3. Kawanishi K. Diverse properties of the mesothelial cells in health and disease. *Pleura and Peritoneum*. 2016;1(2):79-89. doi:10.1515/pp-2016-0009
4. Isaza-Restrepo A, Martin-Saavedra J, Velez-Leal J, Vargas-Barato F, Riveros-Dueñas R. The Peritoneum: Beyond the Tissue – A Review. Review. *Frontiers in Physiology*. 2018;9:738. doi:10.3389/fphys.2018.00738
5. Van Baal JO, Van de Vijver KK, Nieuwland R, et al. The histophysiology and pathophysiology of the peritoneum. *Tissue Cell*. 2017;49(1):95-105. doi:10.1016/j.tice.2016.11.004
6. Franken L, Schiwon M, Kurts C. Macrophages: sentinels and regulators of the immune system. *Cellular Microbiology*. 2016;18(4):475-87. doi:10.1111/cmi.12580
7. García-Peñarrubia P, Ruiz-Alcaraz A, Ruiz-Ballester M, Ramírez-Pávez TN, Martínez-Esparza M. Recent insights into the characteristics and role of peritoneal macrophages from ascites of cirrhotic patients. *World J Gastroenterol*. 2021;27(41):7014-24. doi:10.3748/wjg.v27.i41.7014
8. Mosser DM, Edwards JP. Exploring the full spectrum of macrophage activation. *Nature Reviews Immunology*. 2008;8(12):958-69. doi:10.1038/nri2448
9. Ricketts TD, Prieto-Dominguez N, Gowda PS, Ubil E. Mechanisms of Macrophage Plasticity in the Tumor Environment: Manipulating Activation State to Improve Outcomes. *Frontiers in Immunology*. 2021;12:642285. doi:10.3389/fimmu.2021.642285
10. Pan Y, Yu Y, Wang X, Zhang T. Tumor-Associated Macrophages in Tumor Immunity. Review. *Frontiers in Immunology*. 2020;11:775758. doi:10.3389/fimmu.2020.583084
11. Kinoshita J, Fushida S, Yamaguchi T, et al. Prognostic value of tumor-infiltrating CD163+macrophage in patients with metastatic gastric cancer undergoing multidisciplinary treatment. *BMC Cancer*. 2022;22(1):608. doi:10.1186/s12885-022-09713-y
12. Liu J, Geng X, Hou J, Wu G. New insights into M1/M2 macrophages: key modulators in cancer progression. *Cancer Cell International*. 2021;21(1):389. doi:10.1186/s12935-021-02089-2
13. Orecchioni M, Ghosheh Y, Pramod AB, Ley K. Macrophage Polarization: Different Gene Signatures in M1(LPS+) vs. Classically and M2(LPS–) vs. Alternatively Activated Macrophages. *Frontiers in Immunology*. 2019;10:1084. doi:10.3389/fimmu.2019.01084

14. Ruiz-Alcaraz AJ, Carmona-Martínez V, Tristán-Manzano M, et al. Characterization of human peritoneal monocyte/macrophage subsets in homeostasis: Phenotype, GATA6, phagocytic/oxidative activities and cytokines expression. *Scientific Reports*. 2018;8(1):12794. doi:10.1038/s41598-018-30787-x
15. Jayakumar P, Laganson A, Deng M. GATA6(+) Peritoneal Resident Macrophage: The Immune Custodian in the Peritoneal Cavity. *Front Pharmacol*. 2022;13:866993. doi:10.3389/fphar.2022.866993
16. Dos Anjos Cassado A, D'Império Lima MR, Ramalho Bortoluci K. Revisiting mouse peritoneal macrophages: heterogeneity, development, and function. *Frontiers in Immunology*. 2015;6:225. doi:10.3389/fimmu.2015.00225
17. Zwicky SN, Stroka D, Zindel J. Sterile Injury Repair and Adhesion Formation at Serosal Surfaces. Review. *Frontiers in Immunology*. 2021;12:684967. doi:10.3389/fimmu.2021.684967
18. Pavlou S, Wang L, Xu H, Chen M. Higher phagocytic activity of thioglycollate-elicited peritoneal macrophages is related to metabolic status of the cells. *Journal of Inflammation*. 2017;14(1):4. doi:10.1186/s12950-017-0151-x
19. Uribe-Querol E, Rosales C. Phagocytosis: Our Current Understanding of a Universal Biological Process. Review. *Frontiers in Immunology*. 2020;11:1066. doi:10.3389/fimmu.2020.01066
20. Cavinato L, Genise E, Luly FR, Di Domenico EG, Del Porto P, Ascenzioni F. Escaping the Phagocytic Oxidative Burst: The Role of SODB in the Survival of Pseudomonas aeruginosa Within Macrophages. Original Research. *Frontiers in Microbiology*. 2020;11:326. doi:10.3389/fmicb.2020.00326
21. Canton M, Sánchez-Rodríguez R, Spera I, et al. Reactive Oxygen Species in Macrophages: Sources and Targets. Review. *Frontiers in Immunology*. 2021;12:734229. doi:10.3389/fimmu.2021.734229
22. Virág L, Jaén RI, Regdon Z, Boscá L, Prieto P. Self-defense of macrophages against oxidative injury: Fighting for their own survival. *Redox Biol*. 2019;26:101261. doi:10.1016/j.redox.2019.101261
23. Ren K, Xie X, Min T, et al. Development of the Peritoneal Metastasis: A Review of Back-Grounds, Mechanisms, Treatments and Prospects. *Journal of Clinical Medicine*. 2022;12(1):103. doi:10.3390/jcm12010103
24. Glehen O, Gilly FN, Boutitie F, et al. Toward curative treatment of peritoneal carcinomatosis from nonovarian origin by cytoreductive surgery combined with perioperative intraperitoneal chemotherapy. *Cancer*. 2010;116(24):5608-18. doi:10.1002/cncr.25356
25. Glehen O, Kwiatkowski F, Sugarbaker PH, et al. Cytoreductive Surgery Combined With Perioperative Intraperitoneal Chemotherapy for the Management of Peritoneal Carcinomatosis From Colorectal Cancer: A Multi-Institutional Study. *Journal of Clinical Oncology*. 2004;22(16):3284-92. doi:10.1200/JCO.2004.10.012
26. Zhou S, Feng Q, Zhang J, et al. High-grade postoperative complications affect survival outcomes of patients with colorectal Cancer peritoneal metastases treated with Cytoreductive surgery and Hyperthermic

Intraperitoneal chemotherapy. *BMC Cancer*. 2021;21(1):41. doi:10.1186/s12885-020-07756-7
27. Zulfiqar M, Koen J, Nougaret S, et al. Krukenberg Tumors: Update on Imaging and Clinical Features. *AJR Am J Roentgenol*. 2020;215(4):1020-29. doi:10.2214/ajr.19.22184
28. Kanda M, Kodera Y. Molecular mechanisms of peritoneal dissemination in gastric cancer. *World J Gastroenterol*. 2016;22(30):6829-40. doi:10.3748/wjg.v22.i30.6829
29. Kamat AA, Fletcher M, Gruman LM, et al. The clinical relevance of stromal matrix metalloproteinase expression in ovarian cancer. *Clinical Cancer Research*. 2006;12(6):1707-14. doi:10.1158/1078-0432.ccr-05-2338
30. Genin M, Clement F, Fattaccioli A, Raes M, Michiels C. M1 and M2 macrophages derived from THP-1 cells differentially modulate the response of cancer cells to etoposide. *BMC Cancer*. 2015;15:577. doi:10.1186/s12885-015-1546-9
31. Lin Y, Xu J, Lan H. Tumor-associated macrophages in tumor metastasis: biological roles and clinical therapeutic applications. *Journal of Hematology & Oncology*. 2019;12(1):76. doi:10.1186/s13045-019-0760-3
32. Mantovani A, Sica A, Sozzani S, Allavena P, Vecchi A, Locati M. The chemokine system in diverse forms of macrophage activation and polarization. *Trends in Immunology*. 2004;25(12):677-86. doi:10.1016/j.it.2004.09.015
33. Mantovani A, Allavena P, Marchesi F, Garlanda C. Macrophages as tools and targets in cancer therapy. *Nature Reviews Drug Discovery*. 2022;21(11):799-820. doi:10.1038/s41573-022-00520-5
34. Zhang W, Chen L, Ma K, et al. Polarization of macrophages in the tumor microenvironment is influenced by EGFR signaling within colon cancer cells. *Oncotarget*. 2016;7(46):75366-78. doi:10.18632/oncotarget.12207
35. Arung W, Meurisse M, Detry O. Pathophysiology and prevention of postoperative peritoneal adhesions. *World J Gastroenterol*. 2011;17(41):4545-53. doi:10.3748/wjg.v17.i41.4545
36. Coccolini F, Ansaloni L, Manfredi R, et al. Peritoneal adhesion index (PAI): proposal of a score for the “ignored iceberg” of medicine and surgery. *World Journal of Emergency Surgery*. 2013;8(1):6. doi:10.1186/1749-7922-8-6
37. Weibel MA, Majno G. Peritoneal adhesions and their relation to abdominal surgery. A postmortem study. *The American Journal of Surgery*. 1973;126(3):345-53. doi:10.1016/s0002-9610(73)80123-0
38. Yang B, Gong C, Qian Z, et al. Prevention of post-surgical abdominal adhesions by a novel biodegradable thermosensitive PECE hydrogel. *BMC Biotechnology*. 2010;10(1):65. doi:10.1186/1472-6750-10-65
39. Tabibian N, Swehli E, Boyd A, Umbreen A, Tabibian JH. Abdominal adhesions: A practical review of an often overlooked entity. *Annals of Medicine and Surgery*. 2017;15:9-13. doi:10.1016/j.amsu.2017.01.021
40. Ellis H, Moran BJ, Thompson JN, et al. Adhesion-related hospital readmissions after abdominal and pelvic surgery: a retrospective cohort

study. *Lancet*. 1999;353(9163):1476-80. doi:10.1016/s0140-6736(98)09337-4
41. Diamond MP, Freeman ML. Clinical implications of postsurgical adhesions. *Human Reproduction Update*. 2001;7(6):567-76. doi:10.1093/humupd/7.6.567
42. Ten Broek RPG, Stommel MWJ, Strik C, van Laarhoven C, Keus F, van Goor H. Benefits and harms of adhesion barriers for abdominal surgery: a systematic review and meta-analysis. *Lancet*. 2014;383(9911):48-59. doi:10.1016/s0140-6736(13)61687-6
43. Sikirica V, Bapat B, Candrilli SD, Davis KL, Wilson M, Johns A. The inpatient burden of abdominal and gynecological adhesiolysis in the US. *BMC Surgery*. 2011;11:13. doi:10.1186/1471-2482-11-13
44. Vrijland WW, Jeekel J, van Geldorp HJ, Swank DJ, Bonjer HJ. Abdominal adhesions: intestinal obstruction, pain, and infertility. *Surgical Endoscopy And Other Interventional Techniques*. 2003;17(7):1017-22. doi:10.1007/s00464-002-9208-9
45. Beyene RT, Kavalukas SL, Barbul A. Intra-abdominal adhesions: Anatomy, physiology, pathophysiology, and treatment. *Current Problems in Surgery*. 2015;52(7):271-319. doi:10.1067/j.cpsurg.2015.05.001
46. Mutsaers SE, Whitaker D, Papadimitriou JM. Stimulation of Mesothelial Cell Proliferation by Exudate Macrophages Enhances Serosal Wound Healing in a Murine Model. *Am J Pathol*. 2002;160(2):681-92. doi:10.1016/S0002-9440(10)64888-2
47. Cheong YC, Laird SM, Li TC, Shelton JB, Ledger WL, Cooke ID. Peritoneal healing and adhesion formation/reformation. *Human Reproduction Update*. 2001;7(6):556-66. doi:10.1093/humupd/7.6.556
48. Diamond MP, El-Hammady E, Wang R, Kruger M, Saed G. Regulation of expression of tissue plasminogen activator and plasminogen activator inhibitor-1 by dichloroacetic acid in human fibroblasts from normal peritoneum and adhesions. *American Journal of Obstetrics and Gynecology*. 2004;190(4):926-34. doi:10.1016/j.ajog.2004.02.009
49. Sulaiman H, Gabella G, Davis MC, et al. Presence and distribution of sensory nerve fibers in human peritoneal adhesions. *Annals of Surgery*. 2001;234(2):256-61. doi:10.1097/00000658-200108000-00016
50. Zindel J, Peiseler M, Hossain M, et al. Primordial GATA6 macrophages function as extravascular platelets in sterile injury. *Science*. 2021;371(6533):eabe0595. doi:10.1126/science.abe0595
51. Bernhardt T, Semmler ML, Schäfer M, Bekeschus S, Emmert S, Boeckmann L. Plasma Medicine: Applications of Cold Atmospheric Pressure Plasma in Dermatology. *Oxidative Medicine and Cellular Longevity*. 2019;2019:3873928. doi:10.1155/2019/3873928
52. Yan D, Sherman JH, Keidar M. Cold atmospheric plasma, a novel promising anti-cancer treatment modality. *Oncotarget*. 2017;8(9):15977-95. doi:10.18632/oncotarget.13304
53. Dubuc A, Monsarrat P, Virard F, et al. Use of cold-atmospheric plasma in oncology: a concise systematic review. *Ther Adv Med Oncol*. 2018;10doi:10.1177/1758835918786475

54. Panngom K, Baik KY, Nam MK, Han JH, Rhim H, Choi EH. Preferential killing of human lung cancer cell lines with mitochondrial dysfunction by nonthermal dielectric barrier discharge plasma. *Cell Death and Disease*. 2013;4(5):642. doi:10.1038/cddis.2013.168
55. Busco G, Robert E, Chettouh-Hammas N, Pouvesle J-M, Grillon C. The emerging potential of cold atmospheric plasma in skin biology. *Free Radical Biology and Medicine*. 2020;161:290-304. doi:10.1016/j.freeradbiomed.2020.10.004
56. Hoffmann C, Berganza C, Zhang J. Cold Atmospheric Plasma: methods of production and application in dentistry and oncology. *Med Gas Res*. 2013;3(1):21. doi:10.1186/2045-9912-3-21
57. Reuter S, von Woedtke T, Weltmann K-D. The kINPen—a review on physics and chemistry of the atmospheric pressure plasma jet and its applications. *Journal of Physics D: Applied Physics*. 2018;51(23):233001. doi:10.1088/1361-6463/aab3ad
58. Braný D, Dvorská D, Halašová E, Škovierová H. Cold Atmospheric Plasma: A Powerful Tool for Modern Medicine. *International Journal of Molecular Sciences*. 2020;21(8):2932. doi:10.3390/ijms21082932
59. Tanaka H, Bekeschus S, Yan D, Hori M, Keidar M, Laroussi M. Plasma-Treated Solutions (PTS) in Cancer Therapy. *Cancers*. 2021;13(7). doi:10.3390/cancers13071737
60. Yan D, Xu W, Yao X, Lin L, Sherman JH, Keidar M. The Cell Activation Phenomena in the Cold Atmospheric Plasma Cancer Treatment. *Scientific Reports*. 2018;8(1):15418. doi:10.1038/s41598-018-33914-w
61. Min T, Xie X, Ren K, et al. Therapeutic Effects of Cold Atmospheric Plasma on Solid Tumor. Review. *Frontiers in Medicine*. 2022;9:884887. doi:10.3389/fmed.2022.884887
62. Fan R, Zhao X, Qi M, et al. Properties and anticancer effects of plasma-activated medium stored at different temperatures. *AIP Advances*. 2022;12(9):095022. doi:10.1063/5.0120681
63. Holl M, Rasch ML, Becker L, et al. Cell Type-Specific Anti-Adhesion Properties of Peritoneal Cell Treatment with Plasma-Activated Media (PAM). *Biomedicines*. 2022;10(4):927. 927. doi:10.3390/biomedicines10040927
64. Tan F, Wang Y, Zhang S, Shui R, Chen J. Plasma Dermatology: Skin Therapy Using Cold Atmospheric Plasma. Review. *Front Oncol*. 2022;12:918484. doi:10.3389/fonc.2022.918484
65. Zhai S-Y, Kong MG, Xia Y-M. Cold Atmospheric Plasma Ameliorates Skin Diseases Involving Reactive Oxygen/Nitrogen Species-Mediated Functions. Review. *Frontiers in Immunology*. 2022;13:868386. doi:10.3389/fimmu.2022.868386
66. Koensgen D, Besic I, Gümbel D, et al. Cold Atmospheric Plasma (CAP) and CAP-Stimulated Cell Culture Media Suppress Ovarian Cancer Cell Growth – A Putative Treatment Option in Ovarian Cancer Therapy. *Anticancer Research*. 2017;37(12):6739-44. doi:10.21873/anticanres.12133
67. Lin AG, Xiang B, Merlino DJ, et al. Non-thermal plasma induces immunogenic cell death in vivo in murine CT26 colorectal tumors.

*OncoImmunology*. 2018;7(9):e1484978. doi:10.1080/2162402X.2018.1484978
68. Feil L, Koch A, Utz R, et al. Cancer-Selective Treatment of Cancerous and Non-Cancerous Human Cervical Cell Models by a Non-Thermally Operated Electrosurgical Argon Plasma Device. *Cancers*. 2020;12(4):1037. doi:10.3390/cancers12041037
69. Marzi J, Stope MB, Henes M, et al. Noninvasive Physical Plasma as Innovative and Tissue-Preserving Therapy for Women Positive for Cervical Intraepithelial Neoplasia. *Cancers*. 2022;14(8):1933. doi:10.3390/cancers14081933
70. Van der Paal J, Verheyen C, Neyts EC, Bogaerts A. Hampering Effect of Cholesterol on the Permeation of Reactive Oxygen Species through Phospholipids Bilayer: Possible Explanation for Plasma Cancer Selectivity. *Scientific Reports*. 2017;7(1):39526. doi:10.1038/srep39526
71. Yan D, Talbot A, Nourmohammadi N, Sherman J, Cheng X, Keidar M. Toward understanding the selective anti-cancer capacity of cold atmospheric plasma - a model based on aquaporins. *Biointerphases*. 2015;10(4):040801. doi:10.1116/1.4938020
72. Azzariti A, Iacobazzi RM, Di Fonte R, et al. Plasma-activated medium triggers cell death and the presentation of immune activating danger signals in melanoma and pancreatic cancer cells. *Scientific Reports*. 2019;9(1):4099. doi:10.1038/s41598-019-40637-z
73. Khalili M, Daniels L, Lin A, et al. Non-thermal plasma-induced immunogenic cell death in cancer. *Journal of Physics D: Applied Physics*. 2019;52(42):423001. doi:10.1088/1361-6463/ab31c1
74. Živanić M, Espona-Noguera A, Lin A, Canal C. Current State of Cold Atmospheric Plasma and Cancer-Immunity Cycle: Therapeutic Relevance and Overcoming Clinical Limitations Using Hydrogels. *Advanced Science*. 2023;10(8):2205803. doi:10.1002/advs.202205803
75. Khabipov A, Freund E, Liedtke KR, et al. Murine Macrophages Modulate Their Inflammatory Profile in Response to Gas Plasma-Inactivated Pancreatic Cancer Cells. *Cancers*. 2021;13(11). doi:10.3390/cancers13112525
76. Eggers B, Marciniak J, Memmert S, Kramer FJ, Deschner J, Nokhbehsaim M. The beneficial effect of cold atmospheric plasma on parameters of molecules and cell function involved in wound healing in human osteoblast-like cells in vitro. *Odontology*. 2020;108(4):607-16. doi:10.1007/s10266-020-00487-y
77. Zhang J-P, Guo L, Chen Q-L, et al. Effects and mechanisms of cold atmospheric plasma on skin wound healing of rats. 10.1002/ctpp.201800025. *Contributions to Plasma Physics*. 2019;59(1):92-101. doi:10.1002/ctpp.201800025
78. Kubinova S, Zaviskova K, Uherkova L, et al. Non-thermal air plasma promotes the healing of acute skin wounds in rats. *Scientific Reports*. 2017;7(1):45183. doi:10.1038/srep45183
79. Polaka S, Katare P, Pawar B, et al. Emerging ROS-Modulating Technologies for Augmentation of the Wound Healing Process. *ACS Omega*. 2022;7(35):30657-72. doi:10.1021/acsomega.2c02675

80. Brüggmann D, Tchartchian G, Wallwiener M, Münstedt K, Tinneberg HR, Hackethal A. Intra-abdominal adhesions: definition, origin, significance in surgical practice, and treatment options. *Dtsch Arztebl Int*. 2010;107(44):769-75. doi:10.3238/arztebl.2010.0769
81. De Wilde RL, Devassy R, ten Broek RPG, et al. The Future of Adhesion Prophylaxis Trials in Abdominal Surgery: An Expert Global Consensus. *Journal of Clinical Medicine*. 2022;11(6). doi:10.3390/jcm11061476
82. Holl M, Becker L, Keller A-L, et al. Laparoscopic Peritoneal Wash Cytology-Derived Primary Human Mesothelial Cells for In Vitro Cell Culture and Simulation of Human Peritoneum. *Biomedicines*. 2021;9(2). doi:10.3390/biomedicines9020176
83. Feuerer N, Morschl J, Daum R, et al. Macrophage retrieval from 3D biomaterials: A detailed comparison of common dissociation methods. *Journal of Immunology and Regenerative Medicine*. 2021;11:100035. doi:10.1016/j.regen.2020.100035
84. Ruiz-Alcaraz AJ, Martínez-Banaclocha H, Marín-Sánchez P, et al. Isolation of functional mature peritoneal macrophages from healthy humans. *Immunology & Cell Biology*. 2020;98(2):114-26. doi:10.1111/imcb.12305
85. Barth ND, Subiros-Funosas R, Mendive-Tapia L, et al. A fluorogenic cyclic peptide for imaging and quantification of drug-induced apoptosis. *Nature communications*. 2020;11(1):4027. doi:10.1038/s41467-020-17772-7
86. Telford W, Komoriya A, Packard B. Multiparametric Analysis of Apoptosis by Flow and Image Cytometry. *Methods in Molecular Biology*. 2004;263:141-60. doi:10.1385/1-59259-773-4:141
87. Schultze-Rhonhof L, Marzi J, Carvajal Berrio DA, et al. Human tissue-resident peritoneal macrophages reveal resistance towards oxidative cell stress induced by non-invasive physical plasma. *Frontiers in Immunology*. 2024;15:1357340. doi:10.3389/fimmu.2024.1357340
88. Huang X, Halicka HD, Darzynkiewicz Z. Detection of Histone H2AX Phosphorylation on Ser-139 as an Indicator of DNA Damage. *Current Protocols in Cytometry*. 2019;30(1):55. doi:10.1002/cpcy.55
89. Fink S, Ruoff F, Stahl A, et al. Multiplexed Serum Antibody Screening Platform Using Virus Extracts from Endemic Coronaviridae and SARS-CoV-2. *ACS Infectious Diseases*. 2021;7(6):1596-606. doi:10.1021/acsinfecdis.0c00725
90. Ruoff F, Henes M, Templin M, et al. Targeted Protein Profiling of In Vivo NIPP-Treated Tissues Using DigiWest Technology. *Applied Sciences*. 2021;11(23). doi:10.3390/app112311238
91. Schiferle EB, Cheon SY, Ham S, et al. Rejection of benign melanocytic nevi by nevus-resident CD4(+) T cells. *Sci Adv*. 2021;7(26):eabg4498. doi:10.1126/sciadv.abg4498
92. Wenzel T, Carvajal Berrio DA, Daum R, et al. Molecular Effects and Tissue Penetration Depth of Physical Plasma in Human Mucosa Analyzed by Contact- and Marker-Independent Raman Microspectroscopy. *ACS Applied Materials & Interfaces*. 2019;11(46):42885-95. doi:10.1021/acsami.9b13221

93. Zbinden A, Marzi J, Schlünder K, et al. Non-invasive marker-independent high content analysis of a microphysiological human pancreas-on-a-chip model. *Matrix Biology*. 2020;85-86:205-20. doi:10.1016/j.matbio.2019.06.008
94. Jolliffe IT, Cadima J. Principal component analysis: a review and recent developments. *Philos Trans A Math Phys Eng Sci*. 2016;374(2065):20150202. doi:10.1098/rsta.2015.0202
95. Feuerer N, Marzi J, Brauchle EM, et al. Lipidome profiling with Raman microspectroscopy identifies macrophage response to surface topographies of implant materials. *Proc Natl Acad Sci U S A*. 2021;118(52):e2113694118. doi:10.1073/pnas.2113694118
96. Chan JW, Taylor DS, Zwerdling T, Lane SM, Ihara K, Huser T. Micro-Raman spectroscopy detects individual neoplastic and normal hematopoietic cells. *Biophysical journal*. 2006;90(2):648-56. doi:10.1529/biophysj.105.066761
97. Notingher I, Green C, Dyer C, et al. Discrimination between ricin and sulphur mustard toxicity in vitro using Raman spectroscopy. *J R Soc Interface*. 2004;1(1):79-90. doi:10.1098/rsif.2004.0008
98. Mahadevan-Jansen A, Richards-Kortum RR. Raman spectroscopy for the detection of cancers and precancers. *J Biomed Opt*. 1996;1(1):31-70. doi:10.1117/12.227815
99. Huang Z, McWilliams A, Lui H, McLean DI, Lam S, Zeng H. Near-infrared Raman spectroscopy for optical diagnosis of lung cancer. *Int J Cancer*. 2003;107(6):1047-52. doi:10.1002/ijc.11500
100. Krafft C, Neudert L, Simat T, Salzer R. Near infrared Raman spectra of human brain lipids. *Spectrochim Acta A Mol Biomol Spectrosc*. 2005;61(7):1529-35. doi:10.1016/j.saa.2004.11.017
101. Cheng WT, Liu MT, Liu HN, Lin SY. Micro-Raman spectroscopy used to identify and grade human skin pilomatrixoma. *Microsc Res Tech*. 2005;68(2):75-9. doi:10.1002/jemt.20229
102. Lakshmi R, Kartha VB, Murali Krishna C, JG RS, Ullas G, Uma Devi P. Tissue Raman spectroscopy for the study of radiation damage: brain irradiation of mice. *Radiat Res*. 2002;157(2):175-82. doi:10.1667/0033-7587(2002)157[0175:trsfts]2.0.co;2
103. Schulz H, Baranska M. Identification and quantification of valuable plant substances by IR and Raman spectroscopy. *Vibrational Spectroscopy*. 2007;43(1):13-25. doi:10.1016/j.vibspec.2006.06.001
104. Czamara K, Majzner K, Pacia MZ, Kochan K, Kaczor A, Baranska M. Raman spectroscopy of lipids: a review. *Journal of Raman Spectroscopy*. 2015;46(1):4-20. doi:10.1002/jrs.4607
105. Naumann D. Infrared and NIR Raman spectroscopy in medical microbiology. Proc. SPIE; 1998:245-57.
106. Hanlon EB, Manoharan R, Koo TW, et al. Prospects for in vivo Raman spectroscopy. *Phys Med Biol*. 2000;45(2):1-59. doi:10.1088/0031-9155/45/2/201
107. Dukor RK. *Vibrational spectroscopy in the detection of cancer*. Handbook of vibrational spectroscopy. 2006.

108. Binoy J, Abraham JP, Joe IH, Jayakumar VS, Petit GR. NIR-FT Raman and FT-IR spectral studies and ab initio calculations of the anti-cancer drug combretastatin-A4. *Journal of Raman Spectroscopy*. 2004;35:939-46. doi:10.1002/jrs.1236
109. Seballos L, Zhang JZ, Sutphen R. Surface-enhanced Raman scattering detection of lysophosphatidic acid. *Anal Bioanal Chem*. 2005;383(5):763-67. doi:10.1007/s00216-005-0097-3
110. Ruiz-Chica AJ, Medina MA, Sánchez-Jiménez F, Ramírez FJ. Characterization by Raman spectroscopy of conformational changes on guanine–cytosine and adenine–thymine oligonucleotides induced by aminooxy analogues of spermidine. *Journal of Raman Spectroscopy*. 2004;35(2):93-100. doi:10.1002/jrs.1107
111. Stone N, Kendall C, Smith J, Crow P, Barr H. Raman spectroscopy for identification of epithelial cancers. *Faraday Discuss*. 2004;126:141-57. doi:10.1039/b304992b
112. Malini R, Venkatakrishna K, Kurien J, et al. Discrimination of normal, inflammatory, premalignant, and malignant oral tissue: a Raman spectroscopy study. *Biopolymers*. 2006;81(3):179-93. doi:10.1002/bip.20398
113. Shetty G, Kendall C, Shepherd N, Stone N, Barr H. Raman spectroscopy: elucidation of biochemical changes in carcinogenesis of oesophagus. *Br J Cancer*. 2006;94(10):1460-4. doi:10.1038/sj.bjc.6603102
114. Koljenović S, Schut TB, Vincent A, Kros JM, Puppels GJ. Detection of meningioma in dura mater by Raman spectroscopy. *Anal Chem*. 2005;77(24):7958-65. doi:10.1021/ac0512599
115. Stone N, Kendall C, Shepherd N, Crow P, Barr H. Near-infrared Raman spectroscopy for the classification of epithelial pre-cancers and cancers. *Journal of Raman Spectroscopy*. 2002;33(7):564-73. doi:10.1002/jrs.882
116. Sigurdsson S, Philipsen PA, Hansen LK, Larsen J, Gniadecka M, Wulf HC. Detection of skin cancer by classification of Raman spectra. *IEEE Trans Biomed Eng*. 2004;51(10):1784-93. doi:10.1109/tbme.2004.831538
117. Viehoever AR, Anderson D, Jansen D, Mahadevan-Jansen A. Organotypic raft cultures as an effective in vitro tool for understanding Raman spectral analysis of tissue. *Photochem Photobiol*. 2003;78(5):517-24. doi:10.1562/0031-8655(2003)078<0517:orcaae>2.0.co;2
118. Silveira Jr L, Sathaiah S, Zângaro RA, Pacheco MTT, Chavantes MC, Pasqualucci CAG. Correlation between near-infrared Raman spectroscopy and the histopathological analysis of atherosclerosis in human coronary arteries. *Lasers in Surgery and Medicine*. 2002;30(4):290-7. doi:10.1002/lsm.10053
119. Faoláin E, Hunter M, Byrne J, et al. A study examining the effects of tissue processing on human tissue sections using vibrational spectroscopy. *Vibrational Spectroscopy*. 2005;38:121-7. doi:10.1016/j.vibspec.2005.02.013

120. Lau DP, Huang Z, Lui H, et al. Raman spectroscopy for optical diagnosis in normal and cancerous tissue of the nasopharynx—preliminary findings. *Lasers in Surgery and Medicine*. 2003;32(3):210-4. doi:10.1002/lsm.10084
121. Katainen E, Elomaa M, Laakkonen U-M, et al. Quantification of the Amphetamine Content in Seized Street Samples by Raman Spectroscopy. *Journal of Forensic Sciences*. 2007;52(1):88-92. doi:10.1111/j.1556-4029.2006.00306.x
122. Pezzotti G, Boffelli M, Miyamori D, et al. Raman spectroscopy of human skin: looking for a quantitative algorithm to reliably estimate human age. *J Biomed Opt*. 2015;20(6):065008. doi:10.1117/1.jbo.20.6.065008
123. Ardavín C, Alvarez-Ladrón N, Ferriz M, Gutiérrez-González A, Vega-Pérez A. Mouse Tissue-Resident Peritoneal Macrophages in Homeostasis, Repair, Infection, and Tumor Metastasis. *Advanced Science*. 2023;10(11):2206617. doi:10.1002/advs.202206617
124. Kaushik NK, Kaushik N, Adhikari M, et al. Preventing the Solid Cancer Progression via Release of Anticancer-Cytokines in Co-Culture with Cold Plasma-Stimulated Macrophages. *Cancers*. 2019;11(6):842. doi:10.3390/cancers11060842
125. Nakamura K, Yoshikawa N, Mizuno Y, et al. Preclinical Verification of the Efficacy and Safety of Aqueous Plasma for Ovarian Cancer Therapy. *Cancers*. 2021;13(5):1141. doi:10.3390/cancers13051141
126. Jiang Y, Zhang Z, Yuan Q, et al. Predicting peritoneal recurrence and disease-free survival from CT images in gastric cancer with multitask deep learning: a retrospective study. *The Lancet Digital Health*. 2022;4(5):340-50. doi:10.1016/S2589-7500(22)00040-1
127. Liedtke KR, Bekeschus S, Kaeding A, et al. Non-thermal plasma-treated solution demonstrates antitumor activity against pancreatic cancer cells in vitro and in vivo. *Scientific Reports*. 2017;7(1):8319. 8319. doi:10.1038/s41598-017-08560-3
128. Galluzzi L, Buqué A, Kepp O, Zitvogel L, Kroemer G. Immunogenic cell death in cancer and infectious disease. *Nat Rev Immunol*. 2017;17(2):97-111. doi:10.1038/nri.2016.107
129. Van Loenhout J, Flieswasser T, Freire Boullosa L, et al. Cold Atmospheric Plasma-Treated PBS Eliminates Immunosuppressive Pancreatic Stellate Cells and Induces Immunogenic Cell Death of Pancreatic Cancer Cells. *Cancers (Basel)*. 2019;11(10):1597. doi:10.3390/cancers11101597
130. Bekeschus S, Müller A, Gaipl U, Weltmann K-D. Physical Plasma Elicits Immunogenic Cancer Cell Death and Mitochondrial Singlet Oxygen. *IEEE Transactions on Radiation and Plasma Medical Sciences*. 2017;2(2):138-46. doi:10.1109/TRPMS.2017.2766027
131. Jayasingam SD, Citartan M, Thang TH, Mat Zin AA, Ang KC, Ch'ng ES. Evaluating the Polarization of Tumor-Associated Macrophages Into M1 and M2 Phenotypes in Human Cancer Tissue: Technicalities and Challenges in Routine Clinical Practice. *Front Oncol*. 2019;9:1512. 1512. doi:10.3389/fonc.2019.01512

132. Davey AK, Maher PJ. Surgical adhesions: a timely update, a great challenge for the future. *J Minim Invasive Gynecol*. 2007;14(1):15-22. doi:10.1016/j.jmig.2006.07.013
133. Menzies D, Pascual MH, Walz MK, et al. Use of icodextrin 4% solution in the prevention of adhesion formation following general surgery: from the multicentre ARIEL Registry. *Ann R Coll Surg Engl*. 2006;88(4):375-82. doi:10.1308/003588406x114730
134. Ahmad G, Kim K, Thompson M, et al. Barrier agents for adhesion prevention after gynaecological surgery. *Cochrane Database Syst Rev*. 2020;3(3):CD000475. Cd000475. doi:10.1002/14651858.CD000475.pub4
135. Gökçelli U, Ercan UK, İlhan E, Argon A, Çukur E, Üreyen O. Prevention of Peritoneal Adhesions by Non-Thermal Dielectric Barrier Discharge Plasma Treatment on Mouse Model: A Proof of Concept Study. *J Invest Surg*. 2020;33(7):605-14. doi:10.1080/08941939.2018.1550542
136. Ar'Rajab A, Dawidson I, Sentementes J, Sikes P, Harris R, Mileski W. Enhancement of peritoneal macrophages reduces postoperative peritoneal adhesion formation. *Journal of Surgical Research*. Mar 1995;58(3):307-12. doi:10.1006/jsre.1995.1048
137. Honjo K, Munakata S, Tashiro Y, et al. Plasminogen activator inhibitor-1 regulates macrophage-dependent postoperative adhesion by enhancing EGF-HER1 signaling in mice. *The FASEB Journal*. 2017;31(6):2625-37. doi:10.1096/fj.201600871RR
138. Ito T, Shintani Y, Fields L, et al. Cell barrier function of resident peritoneal macrophages in post-operative adhesions. *Nature Communications*. 2021;12(1):2232. doi:10.1038/s41467-021-22536-y
139. Sahputra R, Dejyong K, Woolf AS, et al. Monocyte-derived peritoneal macrophages protect C57BL/6 mice against surgery-induced adhesions. Original Research. *Frontiers in Immunology*. 2022;13:1000491. doi:10.3389/fimmu.2022.1000491
140. Vega-Pérez A, Villarrubia LH, Godio C, et al. Resident macrophage-dependent immune cell scaffolds drive anti-bacterial defense in the peritoneal cavity. *Immunity*. 2021;54(11):2578-94. doi:10.1016/j.immuni.2021.10.007
141. Yan D, Talbot A, Nourmohammadi N, et al. Principles of using Cold Atmospheric Plasma Stimulated Media for Cancer Treatment. *Scientific Reports*. 2015;5:18339. doi:10.1038/srep18339
142. Tornin J, Mateu-Sanz M, Rodríguez A, Labay C, Rodríguez R, Canal C. Pyruvate Plays a Main Role in the Antitumoral Selectivity of Cold Atmospheric Plasma in Osteosarcoma. *Scientific Reports*. 2019;9:10681. doi:10.1038/s41598-019-47128-1
143. Edomskis PP, Dik WA, Sparreboom CL, et al. Monocyte response after colorectal surgery: A prospective cohort study. *Frontiers in Immunology*. 2022;13:1031216. doi:10.3389/fimmu.2022.1031216
144. Hirayama D, Iida T, Nakase H. The Phagocytic Function of Macrophage-Enforcing Innate Immunity and Tissue Homeostasis. *International Journal of Molecular Sciences*. 2017;19(1):92. doi:10.3390/ijms19010092

145. Park J-Y, Sung J-Y, Lee J, et al. Polarized CD163+ tumor-associated macrophages are associated with increased angiogenesis and CXCL12 expression in gastric cancer. *Clinics and Research in Hepatology and Gastroenterology*. 2016;40(3):357-65. doi:10.1016/j.clinre.2015.09.005
146. Bekeschus S, Seebauer C, Wende K, Schmidt A. Physical plasma and leukocytes – immune or reactive? 2019;400(1):63-75. Biological Chemistry. doi:10.1515/hsz-2018-0224
147. He Z, Liu K, Scally L, et al. Cold Atmospheric Plasma Stimulates Clathrin-Dependent Endocytosis to Repair Oxidised Membrane and Enhance Uptake of Nanomaterial in Glioblastoma Multiforme Cells. *Scientific Reports*. 2020;10(1):6985. doi:10.1038/s41598-020-63732-y
148. Vogel DYS, Heijnen PDAM, Breur M, et al. Macrophages migrate in an activation-dependent manner to chemokines involved in neuroinflammation. *Journal of Neuroinflammation*. 2014;11(1):23. doi:10.1186/1742-2094-11-23
149. Motaln H, Recek N, Rogelj B. Intracellular Responses Triggered by Cold Atmospheric Plasma and Plasma-Activated Media in Cancer Cells. *Molecules*. 2021;26(5):1336. doi:10.3390/molecules26051336
150. Crestale L, Laurita R, Liguori A, et al. Cold Atmospheric Pressure Plasma Treatment Modulates Human Monocytes/Macrophages Responsiveness. *Plasma*. 2018;1(2):261-76. doi:10.3390/plasma1020023
151. Thorpe GW, Reodica M, Davies MJ, et al. Superoxide radicals have a protective role during H2O2 stress. *Mol Biol Cell*. 2013;24(18):2876-84. doi:10.1091/mbc.E13-01-0052
152. Hwang J, Jin J, Jeon S, et al. SOD1 suppresses pro-inflammatory immune responses by protecting against oxidative stress in colitis. *Redox Biol*. 2020;37:101760. doi:10.1016/j.redox.2020.101760
153. Brentnall M, Rodriguez-Menocal L, De Guevara RL, Cepero E, Boise LH. Caspase-9, caspase-3 and caspase-7 have distinct roles during intrinsic apoptosis. *BMC Cell Biology*. 2013;14(1):32. doi:10.1186/1471-2121-14-32
154. Byeon SE, Yi Y-S, Oh J, Yoo BC, Hong S, Cho JY. The role of Src kinase in macrophage-mediated inflammatory responses. *Mediators Inflamm*. 2012;2012:512926. doi:10.1155/2012/512926
155. Sahin E, Haubenwallner S, Kuttke M, et al. Macrophage PTEN regulates expression and secretion of arginase I modulating innate and adaptive immune responses. *J Immunol*. 2014;193(4):1717-27. doi:10.4049/jimmunol.1302167
156. Brauchle E, Thude S, Brucker SY, Schenke-Layland K. Cell death stages in single apoptotic and necrotic cells monitored by Raman microspectroscopy. *Sci Rep*. 2014;4:4698. doi:10.1038/srep04698
157. Wenzel T, Carvajal Berrio DA, Reisenauer C, et al. Trans-Mucosal Efficacy of Non-Thermal Plasma Treatment on Cervical Cancer Tissue and Human Cervix Uteri by a Next Generation Electrosurgical Argon Plasma Device. *Cancers*. 2020;12(2). doi:10.3390/cancers12020267
158. Wang S, Doona CJ, Setlow P, Li Y-q. Use of Raman Spectroscopy and Phase-Contrast Microscopy To Characterize Cold Atmospheric Plasma

Inactivation of Individual Bacterial Spores. *Applied and Environmental Microbiology*. 2016;82(19):5775-84. doi:10.1128/AEM.01669-16
159. Feuerer N, Carvajal Berrio DA, Billing F, et al. Raman Microspectroscopy Identifies Biochemical Activation Fingerprints in THP-1- and PBMC-Derived Macrophages. *Biomedicines*. 2022;10(5):989. doi:10.3390/biomedicines10050989
160. Montenegro-Burke JR, Sutton JA, Rogers LM, Milne GL, McLean JA, Aronoff DM. Lipid profiling of polarized human monocyte-derived macrophages. *Prostaglandins & other lipid mediators*. 2016;127:1-8. doi:10.1016/j.prostaglandins.2016.11.002
161. Morgan PK, Huynh K, Pernes G, et al. Macrophage polarization state affects lipid composition and the channeling of exogenous fatty acids into endogenous lipid pools. *The Journal of Biological Chemistry*. 2021;297(6):101341. doi:10.1016/j.jbc.2021.101341
162. Castoldi A, Monteiro LB, van Teijlingen Bakker N, et al. Triacylglycerol synthesis enhances macrophage inflammatory function. *Nat Commun*. 2020;11(1):4107. doi:10.1038/s41467-020-17881-3
163. Batista-Gonzalez A, Vidal R, Criollo A, Carreño LJ. New Insights on the Role of Lipid Metabolism in the Metabolic Reprogramming of Macrophages. *Front Immunol*. 2019;10:2993. doi:10.3389/fimmu.2019.02993
164. Liu M, Guo S, Stiles JK. The emerging role of CXCL10 in cancer (Review). *Oncology letters*. 2011;2(4):583-9. doi:10.3892/ol.2011.300
165. Cheng F, Yan D, Chen J, Keidar M, Sotomayor E. Cold Plasma with Immunomodulatory Properties Has Significant Anti-Lymphoma Activities in Vitro and In Vivo. *Blood*. 2019;134:5307. doi:10.1182/blood-2019-131065
166. Arndt S, Unger P, Wacker E, et al. Cold atmospheric plasma (CAP) changes gene expression of key molecules of the wound healing machinery and improves wound healing in vitro and in vivo. *PLoS One*. 2013;8(11):79325. doi:10.1371/journal.pone.0079325
167. McFarland-Mancini MM, Funk HM, Paluch AM, et al. Differences in wound healing in mice with deficiency of IL-6 versus IL-6 receptor. *J Immunol*. 2010;184(12):7219-28. doi:10.4049/jimmunol.0901929
168. Tager AM, Kradin RL, LaCamera P, et al. Inhibition of Pulmonary Fibrosis by the Chemokine IP-10/CXCL10. *American Journal of Respiratory Cell and Molecular Biology*. 2004;31(4):395-404. doi:10.1165/rcmb.2004-0175OC

## 8 Declaration (Erklärung zum Eigenanteil)

Die Arbeit wurde am Department für Frauengesundheit der Universität Tübingen, am Institut für Biomedical Engineering in der Abteilung Medizintechnik und Regenerative Medizin, und am NMI Naturwissenschaftlichen Medizinischen Institut an der Universität Tübingen in Reutlingen unter der Betreuung von Herrn Prof. Dr. med. Martin Weiss (Doktorvater) durchgeführt.

Die Konzeption der Studie erfolgte in Zusammenarbeit mit Herrn Prof. Dr. med. Martin Weiss. Sämtliche Versuche wurden nach Einarbeitung durch folgende Labormitglieder (Dr. rer. nat. Nora Feuerer, Dr. rer. nat. Ricarda Breitmeyer, Dr. med. Myriam Holl, Dr. rer. nat. Johanna Heider, Dr. rer. nat. Anna-Lena Keller, Daniel Carvajal-Berrio und Prof. Dr. med. Martin Weiss) von mir eigenständig durchgeführt. Der DigiWest-Versuch wurde von der Arbeitsgruppe Assayentwicklung von Herrn Dr. rer. nat. Markus Templin (Gruppenleiter) am NMI durchgeführt.

Die statistische Auswertung erfolgte in Rücksprache mit Herrn Daniel Carvajal-Berrio (Raman Mikrospektroskopie), Dr. rer. nat. Julia Marzi (Raman Mikrospektroskopie) und Prof. Dr. med. Martin Weiss.

Ich versichere, das Manuskript selbständig verfasst zu haben und keine weiteren als die von mir angegebenen Quellen verwendet zu haben.

Tübingen, den

Laura Schultze-Rhonhof

## 9 List of publications

Holl M, Rasch ML, Becker L, Keller AL, **Schultze-Rhonhof L**, Ruoff F, Templin M, Keller S, Neis F, Keßler F, Andress J, Bachmann C, Krämer B, Schenke-Layland K, Brucker SY, Marzi J, Weiss M. Cell Type-Specific Anti-Adhesion Properties of Peritoneal Cell Treatment with Plasma-Activated Media (PAM). *Biomedicines*. 2022;10(4). doi:10.3390/biomedicines10040927.

**Schultze-Rhonhof L**, Marzi J, Carvajal Berrio DA, et al. Human tissue-resident peritoneal macrophages reveal resistance towards oxidative cell stress induced by non-invasive physical plasma. *Frontiers in Immunology*. 2024;15:1357340. doi:10.3389/fimmu.2024.1357340

## 10 Acknowledgements

Ein besonderer Dank gilt meinem Doktorvater Herrn Prof. Dr. med. Martin Weiss für die Aufnahme in seine Arbeitsgruppe und die fachliche Unterstützung bei der Planung, Durchführung und dem Schreiben der Dissertation.

Ganz besonders möchte ich mich bei Nora, Ricarda, Myriam, Johanna, Anna-Lena, Daniel und Julia bedanken für die Einarbeitung, die ständige Unterstützung und das schöne Arbeitsumfeld im Labor.

Schließlich gilt ein besonderer Dank meiner Familie, meinem Patenonkel und meinem Freund für ihre große Unterstützung diese letzten drei Jahre.